Minna Luoma

New β-decay Half-Lives of Heavy Neutron-Rich Nuclei and Performance Studies of the GEM-TPC Detector

UNIVERSITY OF JYVÄSKYLÄ

FACULTY OF MATHEMATICS
AND SCIENCE

Minna Luoma

New β-decay Half-Lives of Heavy Neutron-Rich Nuclei and Performance Studies of the GEM-TPC Detector

Esitetään Jyväskylän yliopiston matemaattis-luonnontieteellisen tiedekunnan suostumuksella
julkisesti tarkastettavaksi Ylistönrinteen auditoriossa FYS1
marraskuun 10. päivänä 2023 kello 12.

Academic dissertation to be publicly discussed, by permission of
the Faculty of Mathematics and Sciences of the University of Jyväskylä,
in Ylistönrinne, auditorium FYS1, on November 10, 2023, at 12 o'clock.

JYVÄSKYLÄN YLIOPISTO
UNIVERSITY OF JYVÄSKYLÄ

JYVÄSKYLÄ 2023

Editors
Ilari Maasilta
Department of Physics, University of Jyväskylä
Päivi Vuorio
Open Science Centre, University of Jyväskylä

ABSTRACT

Luoma, Minna
New β-decay half-lives of heavy neutron-rich nuclei and performance studies of
the GEM-TPC detector

This thesis presents results from the experiments aimed to measure new β-decay half-lives of neutron-rich nuclei near the $N = 126$ shell and investigate the performance of the GEM-TPC detector. Experimental requirements for the β-decay experiment included production, identification, and analysis of properties of heavy neutron-rich nuclei. In total, one experiment and two in-beam tests were conducted at the FAIR/GSI facility. Four new β-decay half-lives for isotopes $^{197-198}$Re, ^{195}W, and ^{191}Ta were measured. Additionally, the measured half-life values for $^{199-200}$Os and ^{196}Re were consistent with literature values.

Detailed analyses of the experiment and in-beam tests are presented, including a comparison with measured β-decay half-lives and predicted values from the FRDM + QRPA and CQRPA models. Consistently shorter half-life values than predictions were observed for nuclei near $N = 126$ shell.

The performance analysis of the GEM-TPC detector provided information on its properties, such as x position resolution, y position resolution, cluster strip multiplicity, control sum, detection and tracking efficiencies, strip signal summation, and data digitization impact. Moreover, a clusterization was utilized for the first time in the data analysis of the GEM-TPC detector.

The objectives of the studies were to increase our understanding about the properties of nuclei in the vicinity of the third r-process peak and to measure the capabilities of the GEM-TPC. The experimental results of the new β-decay half-lives can be used to validate existing models and improve our understanding of the properties of these nuclei. The performance study of GEM-TPC provides information on its measuring capabilities and suitability for future investigations and assists in planning the future experiments.

Keywords: beta-decay, neutron-rich nuclei, half-life, r-process, GEM-TPC, Super-FRS.

TIIVISTELMÄ (ABSTRACT IN FINNISH)

Tämä väitöskirja esittelee tuloksia kokeista, joiden tarkoituksena oli mitata uusia neutronirikkaiden ytimien β-hajoamisten puoliintumisaikoja $N = 126$ kuoren läheisyydessä ja tutkia GEM-TPC-ilmaisimen suorituskykyä. Kokeelliset vaatimukset β-hajoamisen tutkimukseen sisälsivät raskaiden neutronirikkaiden ytimien tuottamisen, tunnistamisen ja ytimien ominaisuuksien analysoinnin. Yhteensä kolme mittausta suoritettiin FAIR/GSI-kiihdytinlaboratoriossa. Neljä uutta beetahajoamisen puoliintumisaikaa mitattiin $^{197-198}$Re, ^{195}W ja ^{191}Ta isotoopeille. Lisäksi mitatut puoliintumisajat $^{199-200}$Os ja ^{196}Re isotoopeille olivat yhdenmukaisia kirjallisuusarvojen kanssa.

Analyysi kolmesta mittauksesta esitetään, sisältäen vertailun mitattujen beetahajoamisten puoliintumisaikojen ja FRDM + QRPA- ja CQRPA-malleista saatujen ennustettujen arvojen välillä. $N = 126$ kuoren läheisyydessä sijaitseville ytimille havaittiin johdonmukaisesti ennusteita lyhyempiä puoliintumisajan arvoja.

GEM-TPC-ilmaisimen suorituskykyanalyysi antoi tietoa ilmaisimen ominaisuuksista, kuten x- ja y-paikkaresoluutiosta, yhden klusterin sisältämien signaalien lukumäärästä, tarkistussummasta, havaitsemis- ja seurantatehokkuudesta, signaalinluentalinjojen signaalien summauksesta ja datan digitalisoinnin vaikutuksesta. Lisäksi klusterisaatiota käytettiin ensimmäistä kertaa tutkitun GEM-TPC-ilmaisimen data-analyysissä.

Tavoitteena oli lisätä ymmärrystämme ytimien ominaisuuksista r-prosessin kolmannen huipun läheisyydessä ja mitata GEM-TPC:n suorituskykyä. Uusia β-hajoamisen puoliintumisaika-arvoja voidaan käyttää olemassa olevien mallien validointiin ja parantaa ymmärrystämme näiden ytimien ominaisuuksista. GEM-TPC:n suorituskykytutkimus antaa tietoa ilmaisimen mittauskyvystä ja soveltuvuudesta tuleviin tutkimuksiin, sekä auttaa tulevien kokeiden suunnittelussa.

Author   Minna Luoma
                    Department of Physics
                    University of Jyväskylä
                    Jyväskylä, Finland

Supervisor   Assoc. Prof. Tuomas Grahn
                    Department of Physics
                    University of Jyväskylä
                    Jyväskylä, Finland

Reviewers   Dr. Alan John Mitchell
                    Department of Nuclear Physics and Accelerator Applications
                    The Australian National University
                    Canberra, Australia

                    Dr. Marco Cortesi
                    Facility for Rare Isotope Beams
                    Michigan State University
                    East Lansing, USA

Opponent   Dr. Karolina Kolos
                    Nuclear and Chemical Sciences Division
                    Lawrence Livermore National Laboratory
                    California, USA

AUTHOR CONTRIBUTIONS

The author of this work carried out the analyses, and interpreted related results presented in this thesis. Additionally, the author performed analysis, wrote the manuscript together with the co-authors, and contributed to interpreting the data for two peer-reviewed publications related to the GEM-TPC performance presented in this work [1, 2].

In addition, the author of this thesis has participated in the installation and maintenance of the JUROGAM 3 Ge-detector array at JYFL-ACCLAB, and participated in the re-commissioning experiment of the FRS, the *S468* and *S496* experiments at FAIR *Phase-0*. The author contributed to the experimental part of 14 peer-reviewed publications for measurements performed at JYFL-ACCLAB, Finland (13), and at GSI, Germany (1).

ACKNOWLEDGEMENTS

ACRONYMS

GEM	Gas Electron Multiplier
JYFL-ACCLAB	Accelerator laboratory of University of Jyväskylä
GSI	Helmholtzzentrum für Schwerionenforschung
FRS	FRagment Separator
FAIR	Facility for Antiproton and Ion Research
Super-FRS	Superconducting FRagment Separator
ToF	Time-of-Flight
TPC	Time Projection Chamber
GEM-TPC	Gas Electron Multiplier Time Projection Chamber
MUSIC	MUlti-Sampling Ionization Chamber
CS	Control Sum
PEXOR	PCI-Express Optical Receiver
TRIXOR	PC-based Trigger Module
DAQ	Data Acquisition
MBS	Multi Branch System
FEBEX3b	Front End Board with optical link EXtension
SAT	Signal Arrival Time
NUSTAR	NUclear STructure Astrophysics and Reactions

CONTENTS

INTRODUCTION

One of the big questions in nuclear physics is how elements heavier than iron are produced in the universe. It is known that the lightest nuclei i.e., hydrogen, helium, and a fraction of lithium, were produced by the Big Bang nucleosynthesis [3]. After that, the elements up to iron can be produced by fusion reactions, while the slow and rapid neutron-capture processes (s- and r-processes, respectively), photo-disintegration, and rapid proton capture (p-process) participate in the production of the heavier elements [4–8]. For example, in the atomic abundance curve, there are three pairs of the double peaks in heavier masses [4], which are filled by the r-process and are close to the known neutron (N) magic numbers 50, 82 and 126 [9].

In the r-process, a seed nucleus captures neutrons up to a point where the β-decay is more probable and faster than neutron capture. After this point, it decays by β decay towards the valley of stability, and then it continues capturing neutrons [4]. When the process approaches nucleus with neutron number close to the magic numbers, the β-decay half-life increases, accumulating material into the abundance peaks. The time scale for neutron capture in the r-process is faster than the typical β-decay half-lives [10]. Since the r-process produces half of the elements heavier than iron, it is a crucial part of nucleosynthesis in the universe. The r-process site was unclear for years, and neutron star merger and supernova explosions were preferred as origins [11]. Finally, the mergers of black holes and neutron stars were established as one of its sites [12].

In addition, the discovery of gravitational waves in 2015 from the merger of two stellar-mass black holes [13] and in 2017 from two neutron-star mergers [14] were breakthroughs in the understanding of the r-process. The detection of the gravitational wave GW170817 was followed by the independent measurement of a γ-ray burst (GRB 170817A) after 1.74 seconds [14]. The observation of a kilonova (AT 2017gfo) [15] was done after the merger of two neutron stars, fuelled by the radioactive decay of neutron-rich elements produced in the neutron-star merger. Consequently, for the r-process to take place, extreme conditions like high neutron flux and high temperature are needed.

Due to the fact that the r-process proceeds very far from stability, it has not been possible to measure the properties of neutron-rich nuclei close to the "waiting point" [4] around $N = 126$ in the past and produce experimental data for modelling and theoretical calculations. Consequently, the only information about these nuclei comes from theoretical models. However, nowadays, particle accelerators can accelerate heavy ions up to relativistic energies, enabling the production of these nuclei experimentally. Following the production, it becomes necessary to identify the produced nuclei and various particle detectors can be utilized to measure their properties.

A primary beam bombarded a light target causes so-called cold-fragmentation and fission reactions that are used to produce neutron-rich nuclei [16–18]. The most important observables for the r-process understanding to be studied of the nuclei are masses, β-decay half-lives, and neutron-capture cross-sections. The present work is focused on studying the β-decay half-life of nuclei close to the $N = 126$ line. Moreover, the present work is part of the analysis of the *S468 FAIR Phase 0* experiment "Search for new neutron-rich isotopes and exploratory studies in the element range from terbium to rhenium", which was performed to identify new neutron-rich isotopes, measure production cross-sections, masses, and β-decay half-lives. The motivation to study the β-decay half-lives is to increase the understanding of nucleosynthesis and produce experimental results which can be used in the theoretical calculations and models.

In addition to the particle accelerator, experimental devices are needed to identify the neutron-rich nuclei and measure β-decay half-lives. In the present work, the FRagment Separator (FRS) [19], located in Helmholtzzentrum für Schwerionen-forschung (GSI) in Darmstadt, Germany, was used to measure the atomic number Z and mass-over-charge ratio A/Q, i.e. to identify the nuclei on an event-by-event basis. The particle beam of ^{208}Pb at 1050 MeV/u, with intensity up to 10^9 ions/spill on a target stack of beryllium ($4 \frac{g}{cm^2}$) and niobium ($223 \frac{mg}{cm^2}$) were used to produce neutron-rich fragments.

The FRS is a powerful device, and more than 210 new isotopes have been discovered by using it [20, 21], and six new elements [22–27] were observed at the GSI using the velocity filter SHIP [28] and the UNIversal Linear ACcelerator (UNI-LAC). However, the production rate decreases as the study of even more exotic nuclei progresses. Therefore, some updates are needed either to the transmission of the FRS or the increased primary beam intensity. The latter is not possible with the current GSI facility, and therefore the construction of the Facility for Antiproton and Ion Research in Europe (FAIR) started in 2017. One of the central experimental devices of the FAIR facility will be the Superconducting FRagment Separator (Super-FRS) [20]. Compared with the existing FRS, the main improvements of the Super-FRS are the increased primary beam intensities, and its more than two times higher acceptance. However, the identification at the Super-FRS will also be made based on the atomic number Z and the mass-over-charge ratio A/Q.

In the future, the Super-FRS will complement the existing separator [20]. Improvements to be applied to that device are superconducting magnets providing maximum magnetic rigidity ($B\rho$) of 20 Tm and higher beam intensities. The higher acceptance of the fragments i.e. a wider range of particle trajectories and energies will be achieved by the superconducting magnets [29]. In addition, a higher resolving power improves the separation and identification of the fragment.

For the determination of the Z and A/Q ratio of the fragment, information on its magnetic rigidity ($B\rho$), time-of-flight (ToF), and energy loss (ΔE) are needed [19,30]. Therefore, along the FRS, different types of detectors are used to measure these

properties. Due to the increasing intensity at the Super-FRS, some upgrades are needed for particle detectors. One improvement is to replace existing Time Projection Chambers, which have a tracking efficiency at most 40 % with a beam intensity $\sim$ 1 MHz [31] with Time Projection Chamber with Gas Electron Multiplier (GEM-TPC) in twin-configuration [32]. The GEM-TPC detector in the twin-configuration can handle beam rates up to MHz, maintaining the tracking efficiency > 95 % on the event-by-event basis.

The present work includes a performance study of the prototype GEM-TPC detector, which was carried out in 2019 at the FRS with a primary ^{238}U beam at 850 MeV/u, with an intensity of up to 1000 ions/spill. Additionally, the performance of the prototype GEM-TPC was studied with the data measured at the FRS in 2016, with the primary beam of ^{12}C, and ^{124}Xe with the energies of 600 MeV/u.

This thesis makes a contribution to the present understanding of nuclear physics by presenting new data on the β-decay half-lives of the heavy neutron-rich nuclei close to the "waiting point" at $N = 126$. These nuclei decay via β decay. Acquiring experimental data is essential to validate existing models and improve our knowledge of the properties of these nuclei. Additionally, the performance of the prototype GEM-TPC detector is studied, providing valuable insights into its capabilities and suitability for future investigations. The findings from this performance study can assist in planning future experiments and support subsequent research.

For this Ph.D. work, one experiment and two in-beam tests were conducted at the FRS. Chapter 1 provides an overview of the physics background and motivation for the research. The second Chapter describes the experimental method and instrumentation used for studying the β-decay half-lives. The third and fourth chapters present the performance study of the prototype GEM-TPC detector. The fifth Chapter describes the analysis method utilized for determining the β-decay half-lives, presents the obtained results, and compares them with the predicted half-lives of the studied nuclei. Finally, the sixth Chapter summarizes the results presented and presents future necessary research activities.

1   PHYSICS BACKGROUND

This chapter provides an introduction to the essential physical processes relevant for the present research. It briefly introduces critical topics such as the r-process, β-decay process, two theoretical models to predict β-decay half-live, and the fragmentation reaction. For a more comprehensive review, see Ref. [5] and the references therein. In addition, the relevant theory of β decay has been briefly introduced.

1.1   r-process

The rapid neutron capture (r-process) [5] is responsible for producing neutron-rich nuclei heavier than iron [33], and all elements heavier than ^{209}Bi [34].

The r-process occurs far from the valley of stability in extreme conditions where there is a high neutron flux ($N_{neutron} > 10^{20}$ cm^{-3}) and high temperature ($T \sim 10^9$ K). Neutron capture takes place within a short time ~ 1 s producing heavier nuclei, up to the point where β decay is more probable and faster, where neutron capture is followed by the β decay or fission towards the valley of stability [35].

The r-process involves sequential neutron captures (n, γ) that deliver material away from the stability. Neutron capture continues until a point, known as the "waiting point", at which photodisintegration (γ,n) and (n,γ) become comparable. In this waiting point, the material accumulates until β decay moves material to the heavier element, i.e. to a higher Z number. In the solar system abundance curve, three peaks are filled by the r-process (see Fig. 1.1), of which the last two peaks are denoted as the 2nd and 3rd r-process peak, respectively. These peaks are located at mass A = 130, and 195 [5]. The origin of the peaks is the accumulated material resulting from the slower neutron-capture reaction rates and the longer β-decay

half-lives.
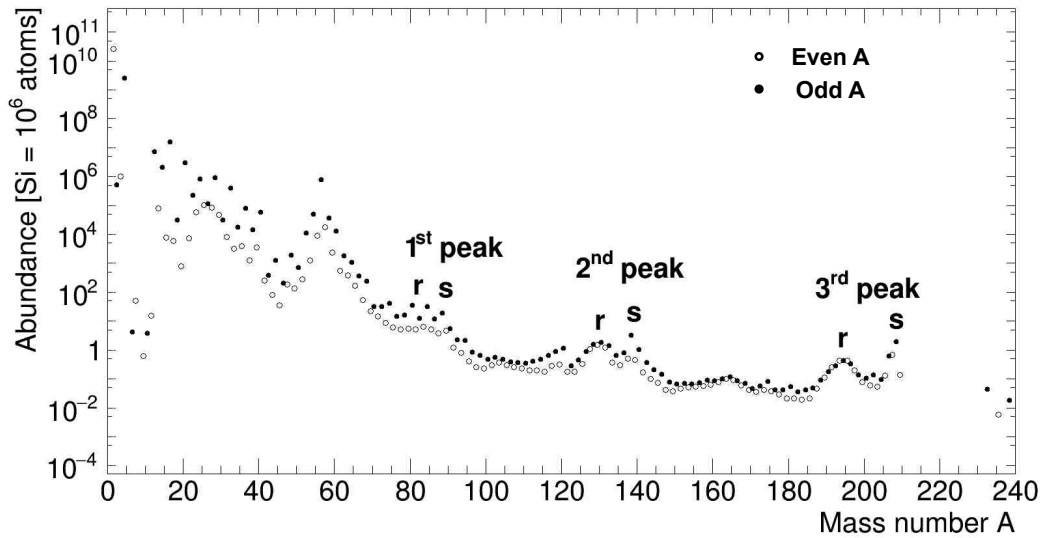
Figure 1.1: The solar system abundances normalized to 10^6 silicon atoms as a function of mass number A. Data taken from [36].

Detection of the gravitational wave GW170817, which resulted from the merger of two neutron stars, along with observation of the associated γ-ray burst GRB 170817A and subsequent identification of the AT 2017gfo kilonova, provided compelling evidence of the origin and site of the r-process. However, due to the challenging and extreme conditions required for the r-process, and because the heavy neutron-rich nuclei are complicated to produce in sufficient abundance to study their properties, experimental data on nuclear properties such as half-lives, masses, and β-delayed-neutron emission probabilities are lacking [33,37]. Consequently, the theoretical calculations rely on estimations for input parameters for the experimentally unknown nuclei [33].

1.2 β-decay process

Henri Becquerel, in 1900 [38] studied the β^- radiation of radium and discovered that it behaves like cathode radiation. Around thirty years later, in 1932, C. D. Anderson discovered the existence of the positron, a particle with a mass comparable to that of the electron and a positive charge [39]. The following year, in 1934, β^+-decay was observed from ^{30}P [40]. A few years later, in 1937, the third β-decay process, electron capture, was discovered by L. Alvarez [41]. The theory for electron capture was developed by G. C. Wick [42] and by H. Yukawa and S. Sakata [43].

β decay is a three-body, weak interaction process in which the nucleus transmutes

towards the valley of stability without changing the mass number. It can be categorized into three reactions, a negative beta (β^-) decay, a positive beta (β^+) decay, and an electron capture. In both β^- and β^+ decay, the electron neutrino and electron antineutrino are also produced. In β^--decay, a neutron inside the nucleus transforms into a proton, while in β^+-decay the reaction is reversed, the proton transforms into the neutron. The third type is electron capture, where the nucleus captures one electron from the inner electron shell, and one proton transforms into a neutron.

In β-decay processes, the measured energy distribution of ejected β particles (positrons or electrons) is continuous, ranging from zero to an endpoint energy. The explanation of the shape of the energy distribution is that there is a second particle called neutrino (the name given by E. Fermi [44]) ejected in these processes that carries the missing energy. The β-decay processes can be expressed as follows:

$$
\begin{aligned}
{}^A_Z X &\longrightarrow {}^A_{Z-1} X' + e^+ + \nu, & \beta^+ - \text{decay} \\
{}^A_Z X &\longrightarrow {}^A_{Z+1} X' + e^- + \bar{\nu}, & \beta^- - \text{decay} \\
{}^A_Z X + e^- &\longrightarrow {}^A_{Z-1} X' + \nu, & \text{electron capture}
\end{aligned}
\tag{1.1}
$$
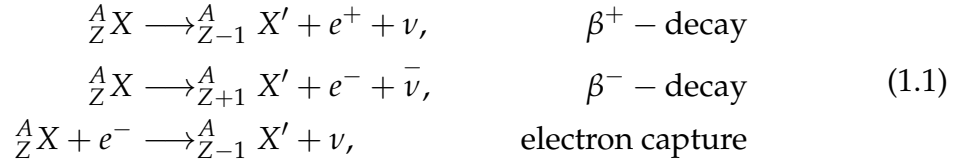
where X and X' represent the mother and daughter nuclei. The electron and positron are denoted as e^- and e^+, while ν and $\bar{\nu}$ represent the neutrino and antineutrino. In the present work, the isotopes under study decay by the β^--process, so from here on, the notation β decay refers to β^- decay.

The β decay can be represented as in Fig. 1.2 for the heavy neutron-rich nuclei. The energy available for the decay, referred to as Q_β, is determined by the mass difference between the mother and daughter nucleus. Q_β should be positive for the β-decay process to occur. During the β-decay process, the daughter nucleus can be left in an exited state, which subsequently de-excites through one or more γ-ray transitions. The daughter nucleus consists of many exited states, each with a different probability of being populated, denoted as I_β. Alternatively, if the populated level is above the neutron emission threshold S_n, a so-called β-delayed neutron can be emitted. This results in a nucleus with two fewer neutrons than the mother nucleus and one more proton.
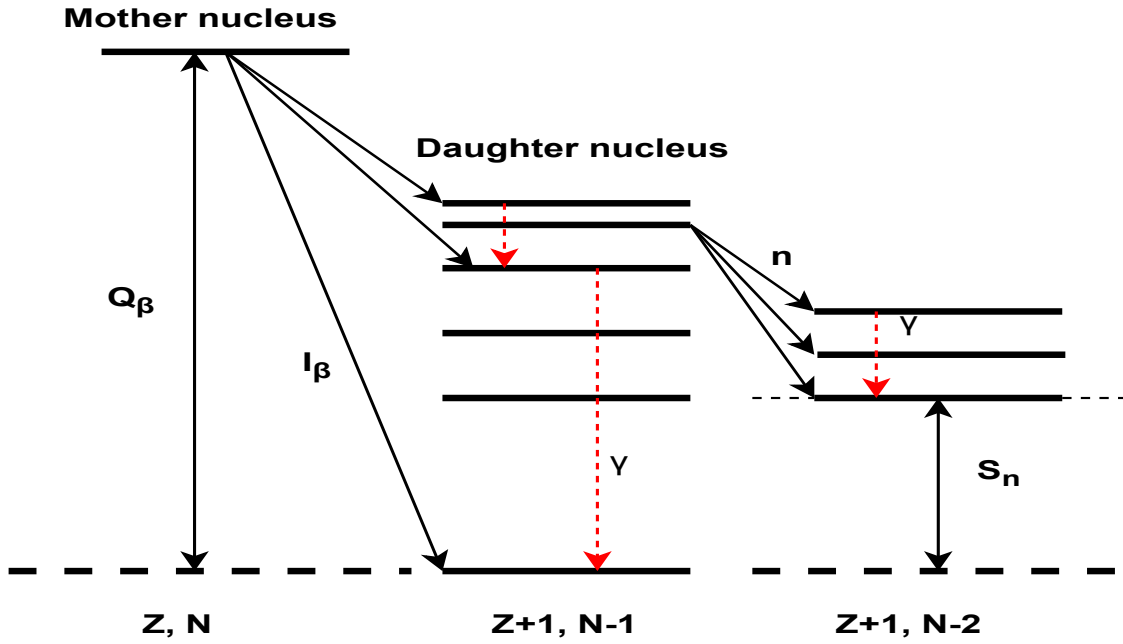
Figure 1.2: Illustration of β-decay in neutron-rich nucleus.

1.2.1 Q value in β-decay

As mentioned in the previous chapter, the Q_β value is defined as the mass difference between the mother and daughter nucleus. For β^- decay, the energy of the emitted β^- particle, denoted as Q_{β^-}, can be expressed as follows:

$$Q_{\beta^-} = [M_N(^A_Z X) - M_N(^A_{Z+1} X') - m_e] \cdot c^2. \tag{1.2}$$

In Equation 1.2, $M_N(^A_Z X)$ refers to the mass of the mother nucleus, $M_N(^A_{Z+1} X')$ corresponds to the mass of the daughter nucleus, and m_e represents the mass of the electron.

1.2.2 Selection rules of β-decay

In 1934, E. Fermi introduced the theory of β decay [44]. During the β decay process, two particles, a neutrino and a β particle, which do not exist in the nucleus before the decay, are created and emitted using the available decay energy [45]. Fermi's Golden Rule gives the transition rate λ of the decay between the initial and final states, and it is expressed as

$$\lambda = \frac{2\pi}{\hbar} |V_{fi}|^2 \rho(E_f), \tag{1.3}$$

where $\rho(E_f)$ is the density of final states and V_{fi} is a matrix element between the

initial and final states. The probability of the β decay depends on different factors, e.g. energy of the initial and final states, as well as the parity and spin of the states involved [45, 46]. Both the β particle and neutrino have a spin value of 1/2, and using the assumption that they are created in the centre of the nuclei they can not carry the orbital angular momentum.

If the spins of the β particle and neutrino are oriented antiparallel, the total spin value becomes 0. This particular decay process is known as allowed Fermi decay [45]. In Fermi decay, the change of the total angular momentum can be expressed as $\Delta \vec{J} = |\vec{J}_i - \vec{J}_f| = 0$ [45]. The Fermi β-decay theory assumes that there is no change in the spin-parity between the initial and final state. However, some experiments showed an infringement in this selection rule [47], and in 1936, Gamow and Teller [48] proposed to incorporate the nuclear spin into the β-decay process and allow the decay process where $\Delta \vec{J} = 1$.

The transitions where $\Delta \vec{J} = 1$ are called allowed Gamow-Teller decays. In the Gamow-Teller decay, the spins of the β particle and neutrino are oriented parallel, resulting in the total spin value of 1. In the so-called allowed approximation, the β particle and neutrino carry the total angular momentum of 1 (but have no orbital angular momentum), and therefore they must be coupled as $\vec{J}_i = \vec{J}_f + 1$. The latter is possible only if $\Delta \vec{J} = 0$ or 1, excluding the case where $\vec{J}_i = 0$ and $\vec{J}_f = 0$, where only the Fermi decay is possible.

When the β particle and neutrino do not carry orbital angular momentum, the parity of the initial and final states of the nuclei remains unchanged. Parity, denoted as π, is determined by the orbital angular momentum l, given by the equation $\pi = (-1)^l$. However, if the β particle and neutrino carry orbital angular momentum i.e., $l \neq 0$, these transitions are referred to as forbidden β-transitions. In such cases, a change in parity occurs between initial and final states as well. The summary of the selection rules for different β-decays are shown in Table 1.1.

Table 1.1: Selection rules for β decay.

Type of the transition	$\Delta \vec{J}$	l	$\Delta \pi$
Allowed	$0, \pm 1$	0	No
First-Forbidden	$0, \pm 1, \pm 2$	1	Yes

1.2.3 Mathematical method

The process of radioactive decay follows an exponential distribution when the number of emitted particles is plotted as a function of time. The half-life, denoted as $T_{1/2}$, represents the time when half of the radioactive nuclei in a given sample have decayed. It can be mathematically expressed as follows [49]:

$$T_{1/2} = \frac{\ln(2)}{\lambda} = \ln(2) \cdot \tau, \qquad\qquad (1.4)$$

where τ corresponds to the mean lifetime, and λ is known as the transition rate. In the present work, the value of τ is determined (see Chapter 5) and utilized to calculate the $T_{1/2}$ for the nuclei under study.

1.2.4 Theoretical models to predict β-decay half-lives

Various models have been developed to compute the half-lives of decaying nuclei far from the valley of stability [33]. Two main approaches have been taken, the macroscopic approximation used in the past and more recently, a microscopic approximation that includes microscopic calculations. One macroscopic approach, known as the Gross Theory (GT), was developed in 1969 [50–52]. In this theory, the discrete sum over states is replaced with integrals. Over time, this theory has been improved by applying a modified one-particle strength function and shell effects of the parent nucleus [53, 54].

The combination of the Quasi-particle Random-Phase Approximation (QRPA) and the Finite-Range Droplet Mass model (FRDM) [55] is one of the microscopic approaches to predicting β-decay half-lives. This model can be used to calculate the properties of almost all nuclei (9318 nuclei above ^{16}O) in the nuclear chart [56]. In this approach, the FRDM is used to predict the masses of the nuclei, whereas the QRPA is utilized to study Gamow-Teller (GT) transitions, taking into account the first-forbidden (FF) transitions from the Gross Theory. A recent addition to these calculations is considering the (n,γ) competition, i.e. the competition between neutron and γ emissions [57]. This factor has been found to result in either increased or decreased neutron emission probabilities. Additionally, it has been predicted that, on average, more neutrons have been emitted after the β decay close to the neutron drip line [57].

The second microscopic approach used for comparing measured β-decay half-lives in this work is known as the density functional+continuum QRPA (CQRPA) [58]. In the CQRPA model, self-consistent calculations for the ground state properties are done using the density functional combined with continuum QRPA. This model takes into account the ground state properties, the FF transitions, the GT transitions, and the excited states by the continuum QRPA calculations.

In the present work, the measured half-lives of β decay will be compared with calculations performed with the FRDM + QRPA, done by P. Möller *et al.* [56], and the CQRPA model computed by I.N. Borzov [58, 59]. The experimental half lives obtained in this work provide a testing ground for the predicted half lives from the models mentioned above. The results of this comparison will be discussed in Chapter 5.

1.3 Fragmentation reaction

In the present work, heavy neutron-rich nuclei were produced using the projectile-fragmentation reaction, which is an important production mechanism for secondary radioactive beams [16]. It can be described as an inelastic nuclear collision between a heavy projectile nucleus and a light target nucleus at relativistic energies. The discovery of the fragmentation reaction resulting in velocities for the fragments almost the same as that of the incident beam was done by H. Heckmann *et al.* in the early 1970s [60].

The fragmentation reaction can be separated into two steps which occur at different times [16,17]. The first step, the spontaneous interaction, the initial collision between projectile and target nucleus, occurs rapidly at the time 10^{-23} s, while the second step, where the system thermalizes and de-excites by different particle evaporation (for example, neutrons, protons, fission etc.) the time varies depending on the excitation energy, 10^{-21}s at 200 MeV, and 10^{-16} s at 10 MeV [16].

The fragmentation reaction between a heavy projectile and a light target nucleus can be represented with a geometrical abrasion model, containing both central and peripheral collisions [16]. A central collision leads to fusion and multifragmentation while the case of peripheral collisions produce fragments with masses close to the projectile nucleus. The schematic figure of the abrasion model with the peripheral collision is shown in Fig. 1.3. In the first step, in the abrasion, the projectile nucleons and the target nucleons create the "participator," i.e. overlapping region where they interact, and it is abraded from the projectile and target nucleons. The resulting part of the projectile nucleus is in a highly excited state, initiating a thermalization process, where the nucleons in the exited region interact with the rest of the nucleus, leading to subsequent de-excitation of the nucleus by different particle evaporation. The formed exited nucleus is called the pre-fragment. The second step of the process, where the pre-fragment de-excites by evaporating different particles and the final fragment is produced, is called ablation.
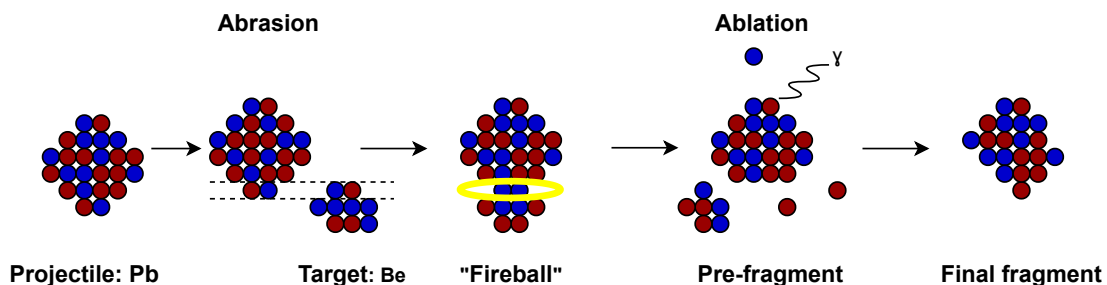

Figure 1.3: Schematic illustration of a peripheral collision in the abrasion-evaporation process between the projectile lead and target beryllium nucleus.

2 EXPERIMENTAL SETUP

In this work, the fragmentation reaction is used to produce exotic neutron-rich nuclei as described in Section 1.3. This nuclear reaction has been utilized at the FRagment Separator (FRS) in Darmstadt, Germany, to produce neutron-rich isotopes [61] studied in the present work. Production of the $^{208}\text{Pb}^{67+}$ ion beam started from an ion source, and it was followed by acceleration at the UNILAC accelerator, which injects the beam into the Schwer-Ionen-Synchrotron 18 (SIS18) [62]. After extraction from the SIS18 when entering the FRS, the beam energy was 1050 MeV/u, with an intensity of 10^9 ions/spill. The beam was not continuous in time. The particles arrived in pulses, denoted as spills in the present work.

This chapter presents the principles of identifying the fragment at the FRS and the instrumentation required for the identification process, including all necessary tracking detectors. The operation principles and calibration methods are also discussed. Special attention is given to the prototype GEM-TPC detector. The tracking detectors for the future Super-FRS will be based on this design since the tracking efficiency > 95 % at the counting rate of 1 MHz is required.

2.1 FRagment Separator

So far, 2740 nuclides have been identified, with 445 of them measured at GSI [63]. The FRS is a device that uses magnetic fields and energy loss in a degrader to separate secondary beams of radioactive isotopes produced by nuclear reactions, and select the nuclei of interest from an unwanted background [64]. The FRS can identify, deliver, and separate secondary beams in-flight through the 70-meter-long separator [19, 30]. Moreover, it can separate and identify all ions from protons up to uranium, with intensities up to 10^9 ions/spill, and at relativistic energies. The schematic figure of the FRS with detectors used in the identification and the

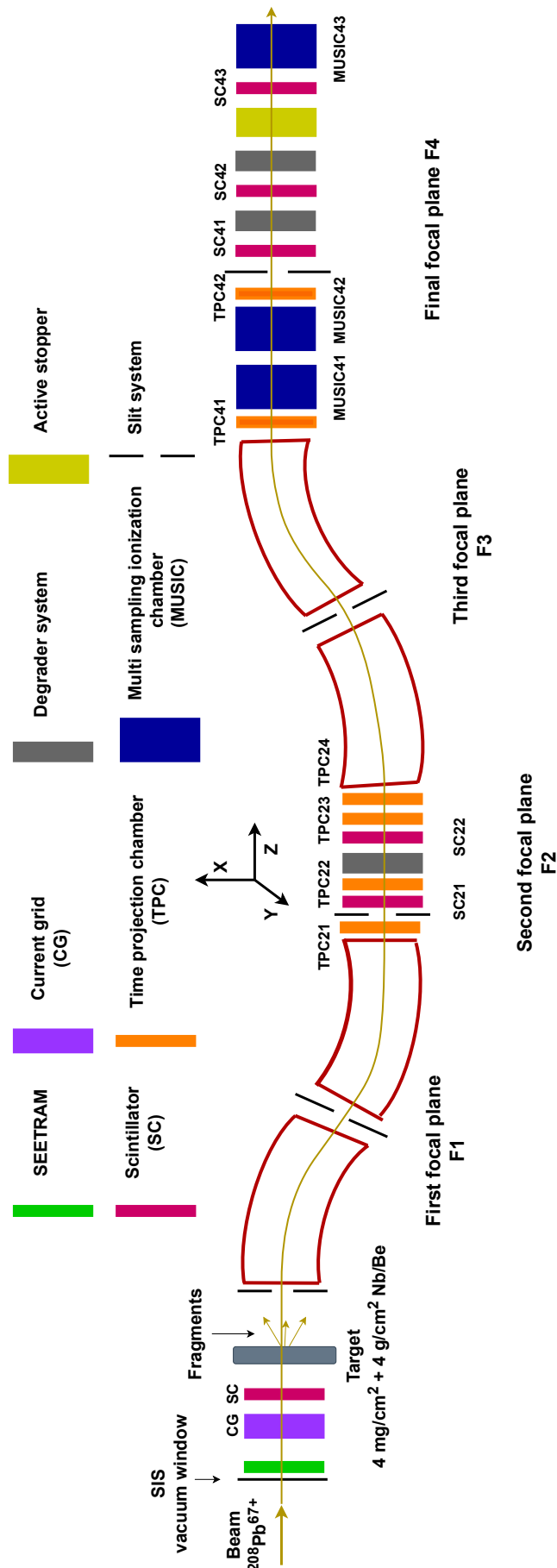coordinate system in the analysis of the current work is shown in Fig. 2.1.

Figure 2.1: The schematic illustration of the FRS setup. The coordinate system, four dipole magnets, and different detectors used in the identification are shown.
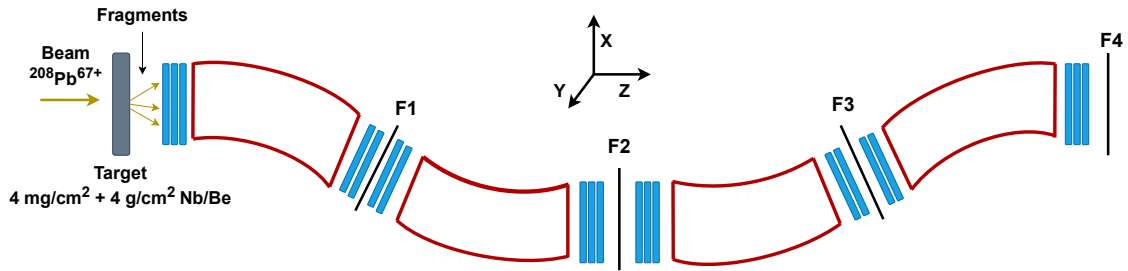
Figure 2.2: The layout of the FRS magnet setup, four dipole magnets are shown by **red** borders and quadrupole magnets by **blue** rectangles. The focal planes from 1 to 4 and the coordinate system are also shown.

The FRS consists of four dipole magnets with a curvature radius of 11.25 m and the highest operation field of 1.6 T, which results in a maximum magnetic rigidity of 18 Tm (curvature radius multiplied by the maximum magnetic field). Quadrupole magnets are placed in front of and behind the dipoles, to focus the trajectories of the fragments (see Fig. 2.2). Suppose two particles with the same magnetic rigidity but different incoming angles enter the dipole magnet. In that case, they experience a different deflection angle, and after the magnet, they end up in different positions. In addition to quadrupole magnets, sextupole magnets are also present in front of and behind the dipole magnets to correct aberrations. However, they are not shown in Fig. 2.2.

At the focal plane *F2*, certain detectors can handle intensities up to 10^6 ions/s. Therefore, after the first two dipole magnets, the primary beam is supposed to be removed, and the magnetic selection is obtained based on the magnetic rigidity [65]. In order to reduce the number of particles entering the *F2* area, slits after the dipoles can also be used. Furthermore, after the first two dipole magnets at the focal plane *F2*, there is a degrader system (see Fig. 2.3), which is a crucial part of the FRS to separate produced fragments [66]. The main purpose of the degrader system is to reduce the energy of the fragments, i.e. to change momentum, and work as an ion-optical component, allowing the modification of the positions of the fragments at the final focal plane *F4* [66].

The degrader system shown in Fig. 2.3 consists of three parts, a ladder degrader including plates of different thicknesses of $AlMg_4$ [67], and wedge-shaped discs and plates. This system has a critical role in the identification by allowing for the optimization of energy-loss. Depending on the goals of the experiment, the FRS can operate either in an achromatic or monoenergetic mode [30].

The monoenergetic degrader, compensates for the energy differences of the fragments by adjusting their path lengths [68]. In the monoenergetic mode, the fragments of the same isotope can reach the final focal plane *F4* in different positions, with their momentum at *F4* being independent of their position at *F2* [68].
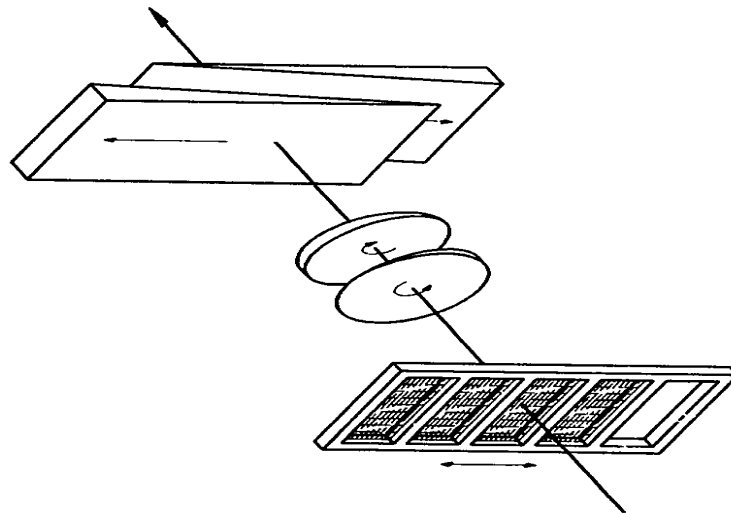
Figure 2.3: The mechanical layout of the degrader system at the focal plane of *F2*. It should be noted that in the current work, the ladder shown at the bottom was located in the middle, which differs from the configuration. Reprinted with permission from [30], Copyright © 1992 publisher Elsevier B.V.

In the achromatic mode, the main goal is to spatially separate different isotopes at the *F4*. Therefore, since the fragments have a different momentum after passing through the achromatic degrader, fragments with very similar A/Q values, transmitted by the first two dipoles, can be separated based on their momentum after the degrader. Thus, according to the new magnetic rigidity of the fragments, the second separation is done utilizing the last two dipoles. With the achromatic mode, the fragments of the same isotope can be spatially focused at *F4*, while additional degraders at *F4* can be utilized for energy bunching for further purposes. In the current work, the FRS was set in the achromatic mode.
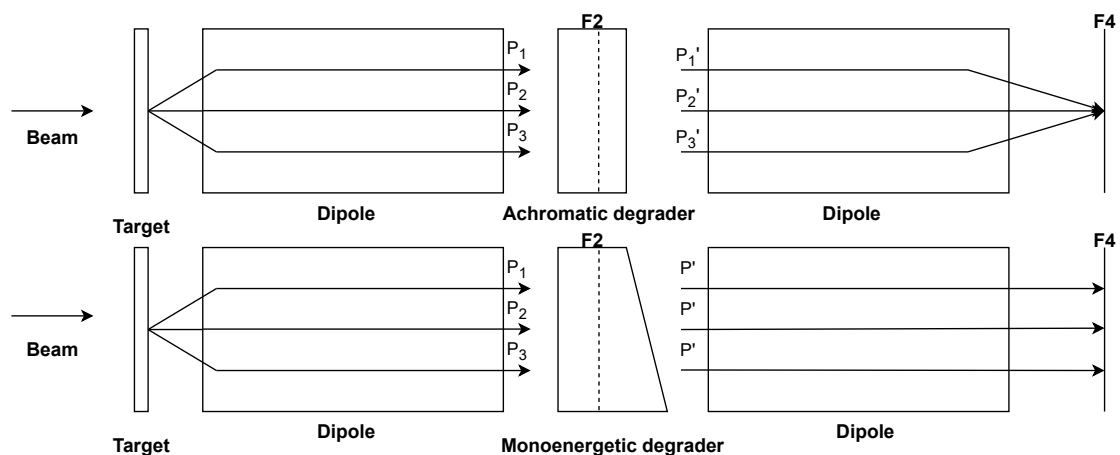
Figure 2.4: Schematic of the achromatic and monoenergetic modes of the FRS. In the achromatic mode, the fragments are horizontally focused at the final focal plane *F4*, while using the monoenergetic mode the fragments have the same momentum after the degrader and are spatially separated in the *F4*.

2.2 Identification

The identification is a crucial part of every experiment at the FRS. The fragments are identified by determining their mass-over-charge ratio (A/Q) and atomic number (Z). These can be determined with the magnetic rigidity ($B\rho$) analysis, time-of-flight (*ToF*) measurement, and energy-loss (ΔE) measurement, i.e. by using the *Bρ-ToF-ΔE* method [19,30,69].

2.2.1 *Bρ-ToF-ΔE* method

In the FRS, magnetic fields created by magnetic dipoles are homogeneous and orthogonal to the momenta of the particles. Heavy fragment with a mass m and charge q travelling with a velocity $\vec{v}$ inside the magnetic field $\vec{B}$ experiences Lorentz force $\vec{F}_L$

$$\vec{F}_L = q\,\vec{v} \times \vec{B}. \tag{2.1}$$

In addition, a centripetal force acts on the particle moving in a circular path. If no other forces are involved, the centripetal force is in balance with the Lorentz force. Forces in balance give the equation

$$qvB = \frac{mv^2}{r}, \tag{2.2}$$

by replacing the radius r with ρ, Equation 2.2 can be expressed

$$B\rho = v\frac{m}{q}. \tag{2.3}$$

Since the energies of the fragments are relativistic, and assuming that the fragments are fully stripped (mass $m = Au$) i.e. all electrons are removed, the momentum can be written

$$p = \beta\gamma Auc, \tag{2.4}$$

where $\beta = \frac{v}{c}$ is the relative velocity to the speed of flight, $\gamma = \sqrt{\frac{1}{1-\beta^2}}$ is the Lorentz factor, A is the atomic mass number, u is the atomic mass unit, and the c is the speed of light. Using the information that the fragments are fully stripped, i.e. the charge $q = Ze$, and by combining the Equations 2.3 and 2.4, the ratio of the mass number and atomic number can be written

$$\frac{A}{Z} = \frac{B\rho e}{\beta\gamma uc}.\tag{2.5}$$

In Equation 2.5, it can be seen that the fully stripped fragments defined with different A and Z values can be identified using the velocity β and the magnetic rigidity $B\rho$ when the value of Z is known. The following subsections introduce the determination of $B\rho$, *ToF*, and ΔE.

2.2.2 *Bρ* determination

After the fragmentation reaction inside the FRS target (see the location in Fig. 2.1), the resulting velocity is about the same for all fragments [30]. Therefore, the first two dipoles determine the curvature radii of the fragments based on the A/Q ratio of the reference fragment. The acceptance of the spectrometer and deviation of the magnetic rigidity impact the resolution of this selection.

A huge number of fragments with the A/Q ratio close to the reference fragment arrives at the *F2* after the first magnetic selection. To solve this problem, before the second selection, the fragments pass through the velocity degrader at the *F2* to reduce the velocity of the fragments, i.e. the momentum of the fragment differs before and after the degrader. Then the second magnetic selection can be made for the reduced fragment velocity.

For the $B\rho$ determination, the magnetic fields of the dipole magnets are set for the reference fragment. This means that such fragment passes through the magnets using a centred trajectory with the magnetic rigidity of $B\rho_0$, hereafter called the reference magnetic rigidity. Then for a non-centered fragment, the magnetic rigidity can be written

$$B\rho = B\rho_0 + \Delta B\rho,\tag{2.6}$$

where $\Delta B\rho$ is relative to the reference magnetic rigidity. Due to the deviation in the momentum of the non-centered fragment δ_{F2-F4} the following expression can be written

$$B\rho = B\rho_0(1 - \delta_{F2-F4}).\tag{2.7}$$

Moreover, the first order ion-optical matrix element of the magnetic separator can be expressed as following

$$x_4 = M_{F2-F4} \cdot x_2 + D_{F2-F4} \cdot \delta_{F2-F4},\tag{2.8}$$

where x_4 and x_2 are the fragment positions at the focal planes $F4$ and $F2$ respectively, M_{F2-F4} is the magnification between the focal planes, and D_{F2-F4} is the dispersion coefficient. By combining equations 2.7 and 2.8 the magnetic rigidity of the selected fragment can be expressed

$$B\rho = B\rho_0 \left(1 - \frac{x_4 - M_{F2-F4} \cdot x_2}{D_{F2-F4}}\right). \tag{2.9}$$

From Equation 2.9 it can be seen that the magnetic rigidity of the fragment under interest can be calculated by measuring its position at the focal planes $F2$ and $F4$.

2.2.3 *ToF* measurement

The scintillators placed at the final focal plane $F4$ and at the central focal plane $F2$ with a distance of about 37 m are used for the *ToF* measurement. The start time of *ToF* is given by the scintillators SC41 or SC42 at $F4$ and the stop time by the SC21 or SC22 at $F2$ (see the locations of the detectors in Fig. 2.1). In total eight-time measurements, SC41-SC21, SC42-SC21, SC41-SC22, and SC42-SC22, can be done each using the left or right sides of the scintillators [67].

For the inverse logic, there are two reasons: the first is to trigger only the events that survive up to the $F4$, and the second is to reduce the dead time. The measured *ToF** of each scintillator pair is then the average of the measured time differences in the left (ToF_R^*) and right sides (ToF_L*), as follows:

$$ToF^* = \frac{ToF_R^* + ToF_L^*}{2} = T_2 - T_4 + T_0,$$
$$ToF = T_4 - T_2 = T_0 - ToF^*, \tag{2.10}$$

where T_2 and T_4 are the times when the fragments pass the $F2$ and $F4$ respectively, T_0 is a time delay set for the T_2, and the *ToF* is the real time-of-flight, which can be expressed by

$$ToF = \frac{d}{v}, \tag{2.11}$$

where d is the flight length of about 37 m, and v is velocity. Connecting functions 2.10 and 2.11 the equation to calculate the velocity is

$$\frac{1}{v} = \frac{T_0}{d} - \frac{ToF^*}{d}. \tag{2.12}$$

2.2.4 ΔE measurement

The linear energy-loss of the charged particle in an absorber material $\frac{dE}{dx}$ is expressed with the Bethe-Bloch formula [49]:

$$-\frac{dE}{dx} = \frac{4\pi e^4 z^2 N Z}{m_0 v^2}\left[\ln\frac{2m_0 v^2}{I} - \ln\left(1 - \frac{v^2}{c^2}\right) - \frac{v^2}{c^2}\right], \quad (2.13)$$

where v and ze are the velocity and charge of the particle, m_0 is the electron rest mass, N and Z are the number density and the atomic number of the absorber material. The I is the average excitation and ionization potential of the absorber material.

From the Bethe-Bloch formula Equation 2.13, it can be seen that the energy loss of the particle is proportional to the square of its charge i.e.

$$\frac{dE}{dx} \propto Q^2. \quad (2.14)$$

The Z identification of different fragments based on their charge (Q) and velocity is done using MUSIC detectors (see details in Section 2.3.4). The charge Q equals the atomic number Z for fully stripped fragments. Therefore, the charge-dependent energy loss can be extracted following the equation 2.14. However, to achieve better separation in the energy loss measurement, the fragments pass through the so-called ladder degrader (see Fig. 2.3), where they lose energy according to their charge and Z value. This is done because all fragments have almost the same velocity after the fragmentation reaction in the target. The simple schematic view of how the ladder degrader affects the velocity of the fragment is shown in Fig. 2.5.
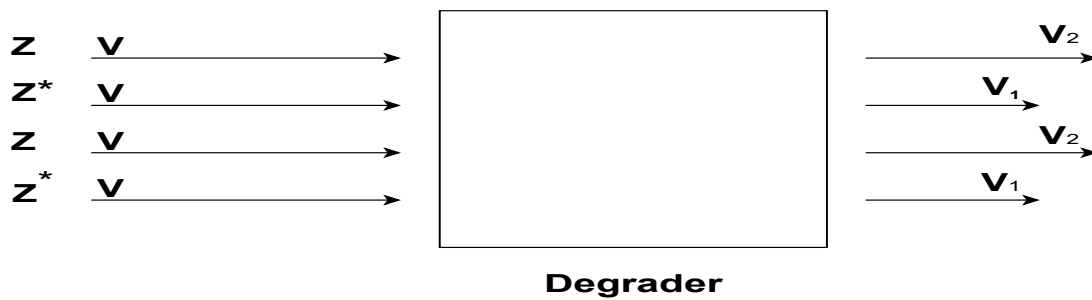

Figure 2.5: The simple schematic view of how the degrader affects the fragments with different atomic number (Z).

2.2.5 Determination of fully stripped fragments

Even when the FRS is set to deliver fully stripped fragments, a small fraction of H-like fragments, and He-like fragments are delivered [70]. Therefore, the degrader energy-loss measurement is needed. This measurement allows for distinguishing the different charge states. The energy loss in the matter of the fragment can be expressed by [65]

$$\Delta E = A \Delta \gamma, \tag{2.15}$$

where ΔE is the kinetic energy loss, the γ is the Lorentz factor, and A is the mass number of the fragment. As explained in Section 2.2.4, the energy-loss of the fragment is proportional to its charge and velocity. Therefore, by reformulating Equation 2.15, ΔE of the fragment over the FRS can be calculated

$$\frac{\Delta E}{Q} = (\gamma_1 - \gamma_2) \cdot \frac{A}{Q}, \tag{2.16}$$

where notations 1 and 2 are the measured Lorentz factors of the fragment in the first and second half of the FRS. Then by using Equations 2.3 and 2.4, γ_1 can be written as follows:

$$\gamma_1 = \frac{eB\rho_1}{cuA/Q \cdot \sqrt{1 - \frac{1}{\gamma_1^2}}}, \tag{2.17}$$

$$\gamma_1^2 = 1 + \left(\frac{e}{cu}\right)^2 \cdot \left(\frac{B\rho_1}{A/Q}\right)^2, \tag{2.18}$$

where e is the electron charge, u is the atomic mass unit, c is the speed of light, and β is the relative velocity. Additionally, γ_2 can be computed directly from the time of flight measurement and $\beta = v/c$ expression.

The energy loss of the fragments as a function of maximum energy loss Q_{max} (see Section 2.3.4 for details on Q_{max} determination), in the ^{193}Ta setting of the $S468$ experiment is shown in Fig. 2.6. In order to identify the fully stripped fragments, production rates of different charge states are calculated using the code GLOBAL [70] and LISE++ program [71, 72]. The line of spots in the middle of the figure represents the fully stripped fragments, denoted as 0e-0e. Additionally, some produced fragments carry one or two electrons over the entire FRS and populate the spots of the fully stripped fragments. However, the calculated ratio of ^{193}Ta isotopes with one electron to fully stripped ones is only about 3 %. The spots below the central line correspond to fragments which carry one electron

after the *F2* degrader, denoted as 0e-1e, and the calculated ratio for ^{199}Os is about 9 %. Additionally, a few entries above the main line correspond to fragments that carried one electron before the degrader (1e-0e). The calculated ratio for these fragments is about less than 1 %, which is why only a few entries are visible in this region.
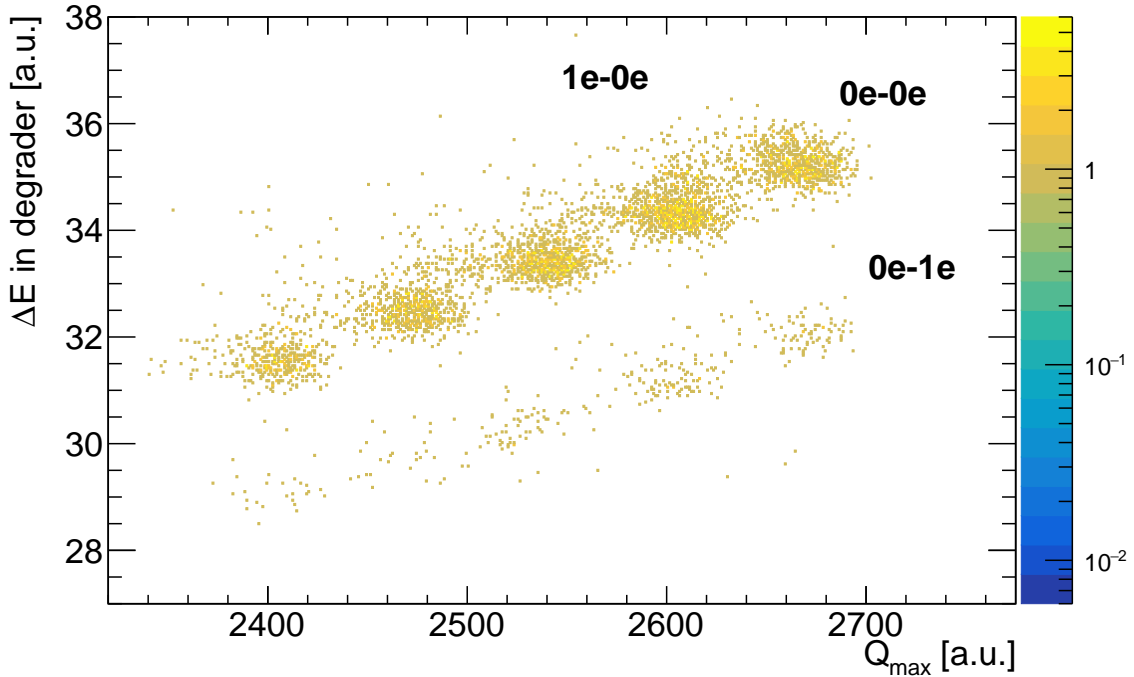
Figure 2.6: Energy loss (ΔE) of the fragments in ^{193}Ta setting in the degrader at *F2* as a function of the maximum energy loss Q_{max} in the MUSIC detectors at the *F4*.

2.3 Instrumentation

Different beam diagnostic systems are utilized for monitoring and tracking along the FRS beamline due to the varying conditions of different experimental areas. So far, Time Projection Chambers (TPCs) [73] have been used for the position measurements. However, in the future, the increasing beam intensities of the Super-FRS will require position measurements with a tracking efficiency >95 % with a counting rate of about 1 MHz, which cannot be achieved with the TPCs [31]. Therefore, Time Projection Chambers with Gas Electron Multipliers (GEM-TPC) detectors in twin field cage configuration [74] were developed to replace TPCs at the Super-FRS.

Nowadays, particle identification at the FRS and in the future at the Super-FRS will be made by the *Bρ-ToF-ΔE* method (see details in Section 2.2) [20, 30]. The ΔE measurement is provided by Multi-Sampling Ionization Chambers (MUSIC) [75],

while Time-of-Flight (*ToF*) is measured by the plastic scintillator detectors [76], and presently in the FRS, the position measurement is done by the TPCs and used to determine the $B\rho$.

In the following sub-chapters, trackers, working principles, and calibrations used in the identification at the FRS are presented.

2.3.1 Trackers at the FRS target area: SEETRAM

In the target area of the FRS, there are three different types of detectors, the SEcondary Electron TRAnsmission Monitor (SEETRAM) [77], a scintillator, and a current grid [78] (see Fig. 2.1). The purpose of these detectors is to measure the position and intensity of the beam, and additionally, they are used to calibrate each other.

The SEETRAM is the detector used to determine the beam intensity at the FRS. It operates in vacuum and consists of three parallel titanium foils, each with the thickness of 10 μm, mounted perpendicular to the beam direction. As the beam passes through these foils, it produces a current that can be collected with an electric field. The magnitude of the produced current is proportional to the intensity of the beam [77]. In the present work, the SEETRAM is utilized to measure beam intensity.

2.3.2 Time Projection Chamber

The TPCs are gas-filled detectors, where the incoming particle ionizes the gas volume, and the produced charge is collected and amplified in the anode wires. The active volume of the TPC at the FRS is 240 mm x 60 mm x 70 mm in the x, y, and z directions.

The TPC consists of four anode wires, two delay lines, and a field cage. The anode wires are used to determine four independent y position measurements and two delay lines to provide two x position measurements. The x coordinate is measured by the time difference at both ends of the delay line, while the y coordinate is computed by measuring the drift times at the anode wires. The field cage consists of thin Mylar strips (3 mm wide) metalized on both sides connected to a high-resistance divider. A voltage applied to the divider is used to create a uniform electric field inside the chamber [31]. The gas in use at the FRS is P10 (90% Ar, 10% CH_4) at atmospheric pressure and room temperature.

Position determination

The x position of the passing particle is determined from the time difference measured by both ends of the delay line. To convert the time into millimetres, the following equation is used [79]

$$x = A(t_l - t_r) + x_{off},$$ (2.19)

where A and x_{off} are calibration constants, and t_l and t_r are the measured times from the left and right sides of the delay line. Because the conventional TPC consists of two delay lines, two sets of calibration parameters are determined for the x coordinate. Since one TPC has four anode wires, four y coordinate calculations can be done with the equation

$$y = v \cdot t_d + y_{off},$$ (2.20)

where v is the drift velocity, t_d is the measured drift time and y_{off} is the determined offset. Since four y positions can be measured, four sets of calibration constants are needed to extract from the calibrations. In order to ensure accurate tracking with the TPC, the times related to the x and y coordinates of the event are correlated by the Control Sum (CS), which is utilized to eliminate noise (see details in Ref. [31]).

Calibrations

Calibrations of TPCs are needed to determine the drift velocity of electrons and signal propagation velocity in the delay lines. The calibrations at the FRS are done with the standard calibration method [31].

This method includes a defocused primary beam and a scintillator fiber grid, which consists of three scintillating fibers in the x and y directions. The diameter of the fibers is 1 mm, and the pitch of 12 mm on x side and 6 mm on y side. One calibration grid is placed in front of each TPC and aligned in the centre of the active area of the detector. With the defocused beam, the entire area covered by the grid is illuminated, and only the particles which interact with the fibers generate the trigger. As an outcome, three peaks are measured with a known distance in the x and y position distributions.

By triggering with the calibration grid, the shape of the calibration grid is visible in the two-dimensional position spectrum, as shown in Fig. 2.7. In that figure, the positions in the x- and y-axes are calibrated, and the distances between the fibers correspond to the known distances of 6 mm and 12 mm.
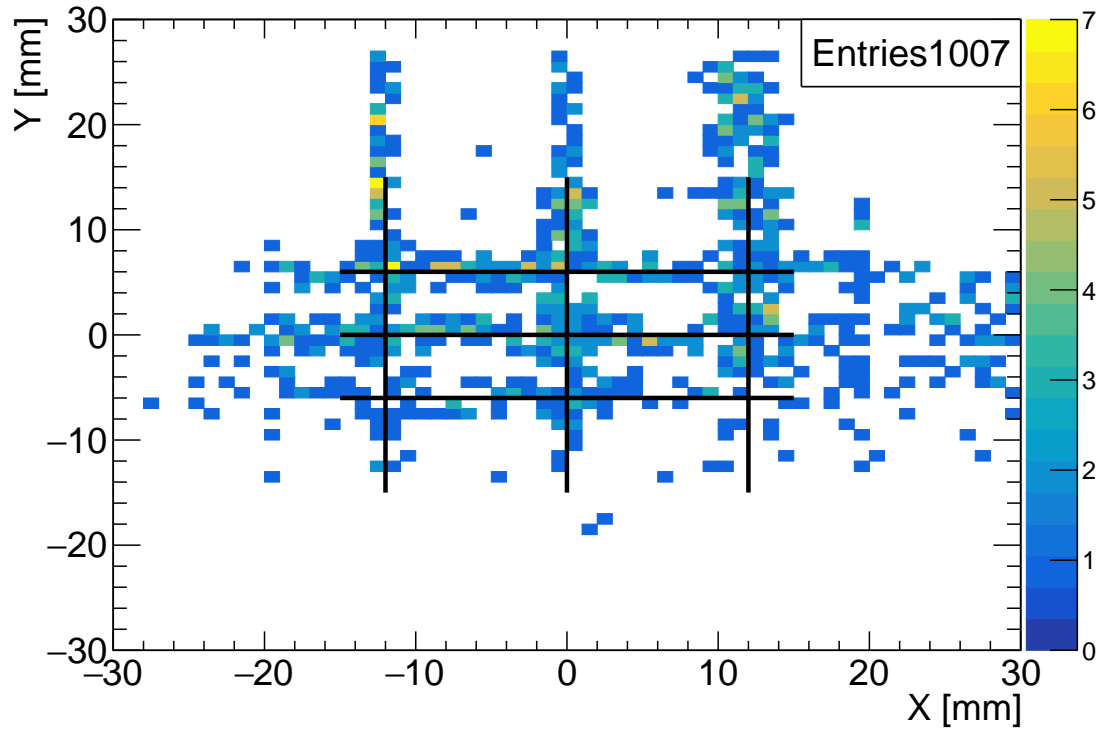
Figure 2.7: The calibrated positions of the TPC42. Three fibers of the calibration grid in the x and y directions are shown with the **black** lines. The figure is adapted from [1], under the license CC BY 4.0. The dashed lines of the original figure are changed to the continuous lines and the number of entries is added.

As an outcome of the calibrations, two sets of the calibrations factors for the x coordinate and four sets for the y coordinates are determined.

2.3.3 GEM-TPC

In the future at the Super-FRS, the GEM-TPC in the twin configuration provides the position information i.e. the x and y coordinates of the traversing particle. This information will be used in the magnetic rigidity ($B\rho$) analysis which is essential part of the particle identification.

The GEM-TPC in the twin configuration is a gaseous detector designed to operate at close to 100 % tracking efficiency at 1 MHz counting rate [32, 80, 81]. It consists of two GEM-TPCs inside the same vessel, sharing the same gas volume (see Fig. 2.8). The active volume of the GEM-TPC detector is 220 mm x 100 mm x 25 mm, in the x, y, and z directions, respectively. In the twin configuration, one GEM-TPC is flipped with respect to the middle plane so that the electric fields of the detectors are in opposite directions. This configuration provides two independent drift volumes and enables the measurement of the Control Sum (CS) [81], the sum of drift times from both detectors. Since the CS should remain constant, it can be used to associate the hits originating from a single event. Essentially, the CS can
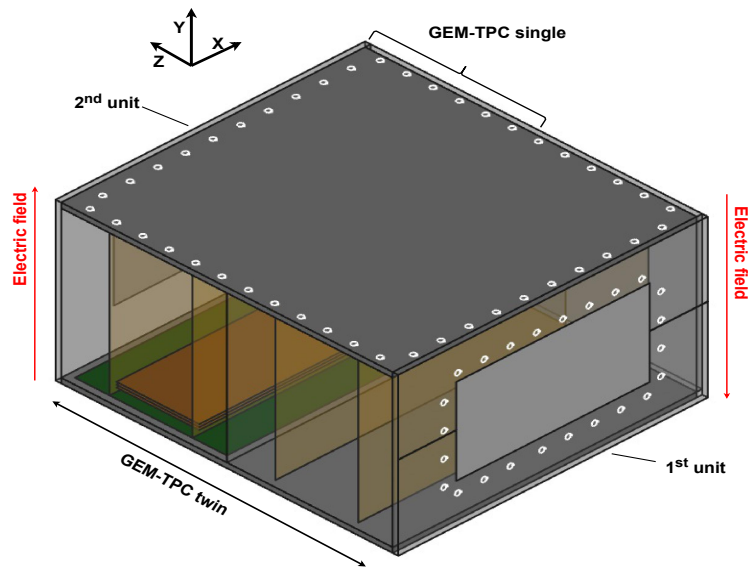
be used to reject the noise and pile-up.

Figure 2.8: An artistic view of the GEM-TPC twin detector configuration showing the direction of the electric field in the first and second unit.

The GEM-TPC consists of a field cage, similar to TPCs [31], a stack of three GEM foils [82] for the amplification, and a front-end electronics. The field cage includes 32 strips (a pitch of 3.12 mm) on both sides of 10 μm thick aluminized Mylar foil [83]. A resistor divider is used to connect the first strip on the cathode and the last strip on the top electrode of the first GEM foil. In that way, a uniform electric field can be applied to the field cage. In the direction of the incoming beam, 512 parallel strips (the pitch of 0.4 mm) are on the readout pad plane of the single GEM-TPC. For more technical details see Ref. [83].

Working principle

Inside the GEM-TPC, the incoming particle ionizes the gas volume, and produces positively charged gas ions and negatively charged electrons. Inside the field cage, the electrons and the ions drift in opposite directions in an electric field.

The x coordinate of the incoming particle is determined from signal reading strips, while the y coordinate can be calculated from the measured drift time of the electrons.

Clusterization process

The process denoted as clusterization means that electron cloud created by a single incoming particle is detected in multiple adjacent strips of the readout pad plane.

Thus, all the strip signals associated with a single event are grouped and fitted with a Gaussian function to obtain the amplitude profile of the cluster and its position. Most of the information about the incoming particle in the GEM-TPC can be determined from the clusters. The cluster provides information to determine the *x* position of the particle, the total collected charge, the cluster strip multiplicity, and the number of reconstructed clusters within the single trigger. In the present work, a new clusterization algorithm for the GEM-TPC detector was developed and tested for the first time [1].
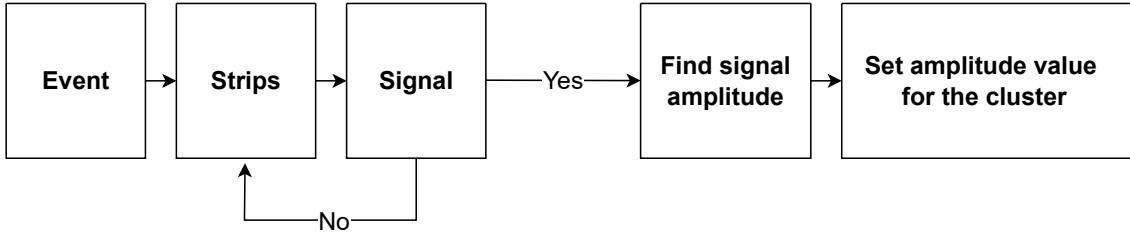

Figure 2.9: The block diagram showing the analysis steps in the clusterization process.

The block diagram of the analysis steps in the clusterization is shown in Fig. 2.9. For each event, the first step is to determine the measured charge, i.e. the signal amplitude of each strip. Afterwards, all the strips belonging to a single event are grouped. The next step is to fit a Gaussian function to determine the amplitude profile of the strips, and the mean value. The normalized Gaussian equation used to fit the cluster is following

$$f(x_{strip}) = \frac{A}{C \cdot \sqrt{2 \cdot \pi}} \cdot e^{-0.5 \cdot \frac{(x_{strip} - B)^2}{C^2}}, \qquad (2.21)$$

where A is the value of the amplitude, X_{strip} is the strip channel number, B is the mean channel, and C is the standard deviation of the fit, hereafter called sigma.

One example of the reconstructed cluster with a mean value of 97.53(8) strip and sigma of 2.41(6) strip is shown in Fig. 2.10. The maximum mean strip number for this cluster is 224 due to the experimental conditions that allowed readout only part of the strips.
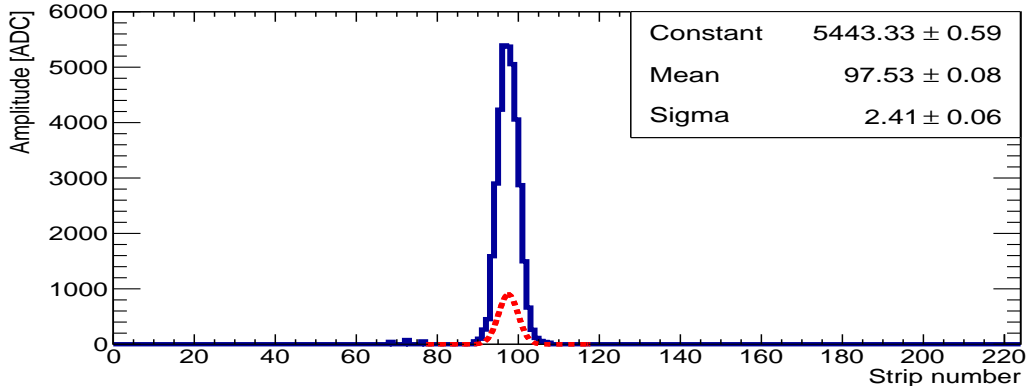
Figure 2.10: An example of the reconstructed cluster shown with a blue line, and a normalized Gaussian function fit drawn with a **red** dashed line. From this cluster, a mean value of 97.53(8), maximum amplitude of 5443.33(59), and sigma of 2.41(6) are extracted.

Position determination

The x coordinate for the event is calculated by multiplying the extracted mean value by the pitch of 0.4 mm (strip width is 0.25 mm) and then subtracting a fixed offset. Thus, the strip in the middle of the detector has a value of $x = 0$ mm. During the in-beam test in 2019, half of the strips of one GEM-TPC were read out, and the following equation was used to calculate the x coordinate

$$X_{GEM-TPC} = B \cdot P - C, \tag{2.22}$$

where $X_{GEM-TPC}$ is the measured x position, P is the pitch width, B is the extracted mean value of the Gaussian fit, and $C = 51.2$ mm is the distance from the edge of the active area to the centre.

The y coordinate of the event is extracted from the signal arrival time T_A of the cluster, where the closest strip to the maximum amplitude of the cluster is used to determine the T_A. Then the equation to calculate y coordinate is given by

$$f(T_A) = T_A \cdot v_{drift} - y_{off}, \tag{2.23}$$

where v_{drift} is the measured drift velocity, and y_{off} is the determined offset.

Calibration

In order to calculate the y coordinate, the calibration is needed to determine an essential parameter, the drift velocity. This calibration process utilizes the standard method employed for conventional TPCs [31] (see details in Section 2.3.2).

The events recorded by the closest TPC calibration grid are projected to the GEM-TPC. This projection provides three peaks from the grid, each at a known distance, as shown in the x direction in Fig. 2.11. In order to calculate the drift velocity for the y coordinate, the drift times of known drift distances are determined. This process includes fitting a Gaussian function to the peaks in the measured time distribution and then calculating the time difference of the mean values between the peaks with known distances.
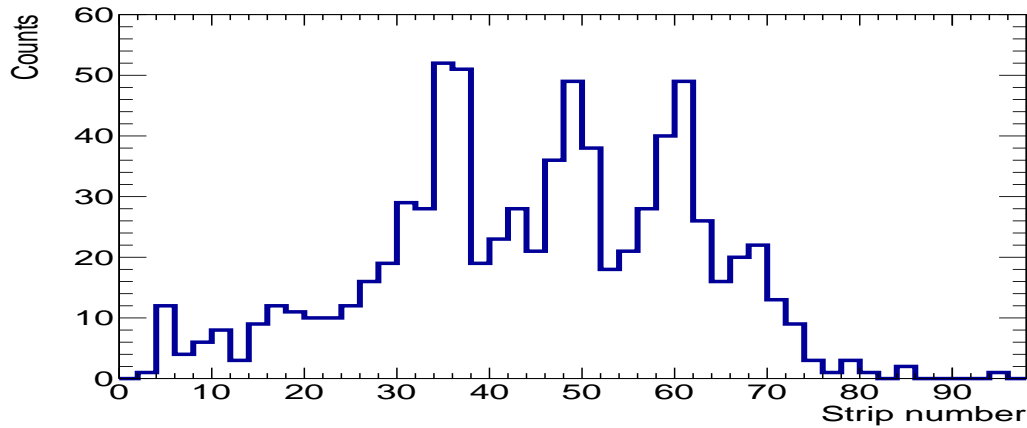

Figure 2.11: The measured x position spectrum (strip number) in the GEM-TPC when the trigger is taken from the calibration grid of the closest TPC.

2.3.4 MUlti-Sampling Ionisation Chamber

The MUlti-Sampling Ionisation Chamber (MUSIC) detector is a gas-filled detector designed to detect positive gas ions and electrons generated by incoming particles [75]. This detector consists of eight anode strips, a cathode, and an electric field created between them [84]. At the FRS, the MUSIC detectors are filled with a continuously flowing P10 gas (90% Argon, 10 % CH_4) and operated at atmospheric pressure and room temperature. The active volume of the detector is 200 mm x 80 mm x 400 mm, in the x, y, and z directions, respectively. The purpose of the MUSIC is to determine the atomic number of the particle, denoted as Z, by measuring the charge produced by the particle passing through the detector.

As shown in Fig. 2.1 at the focal plane $F4$, two MUSIC detectors are placed sequentially along the beam direction, which allows the identification of electron pick-up or loss reactions inside the detectors. Moreover, between the MUSICs at $F4$, a Nb foil was used to remove electrons gained by the particles inside the first MUSIC chamber. Fig. 2.12 shows a correlation plot of the measured energy-loss of the fragments in MUSIC detectors. It can be seen that the fragments without a change in their charge are located along the line, whereas the fragments with a change in the charge are situated either above or below the line, depending on the position of the charge change.

For the identification of the fragment, the value Q_{max} is defined as the highest energy loss measured in two MUSICs. However, the energy loss is proportional to the square of the charge, and therefore, it is very sensitive to the changes. Therefore, it is essential to note that fragments with the same number of electrons in both MUSIC detectors can not be distinguished.
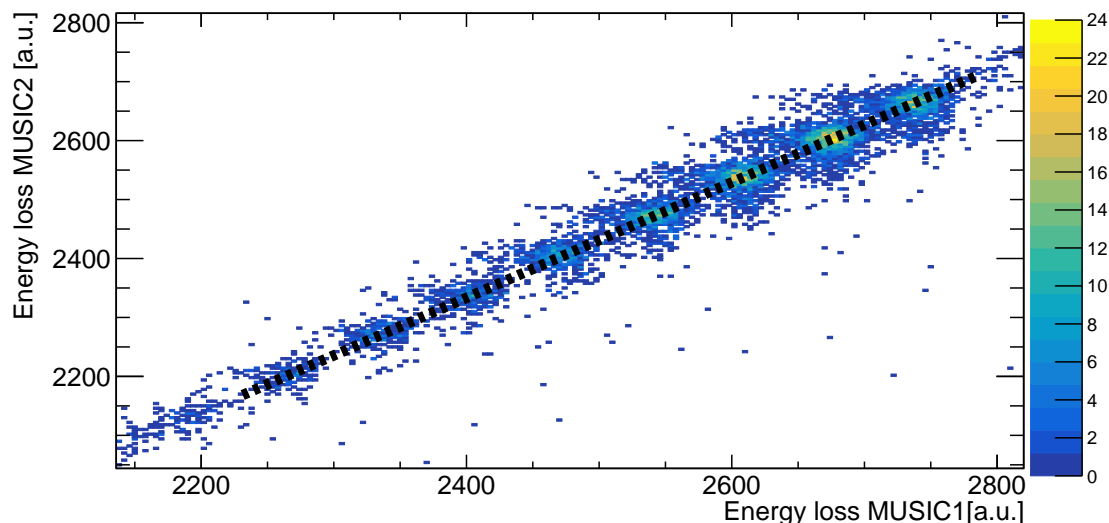

Figure 2.12: The correlation plot of measured energy loss in two MUSIC detectors with the ^{193}Ta setting. The **black** dashed line shows the fragments that lose about the same amount of energy inside both detectors, whereas the fragments with a change in charge are shown above and below the line.

Calibration

According to the Bethe-Bloch formula (Equation 2.13), the energy loss of the fragment is proportional to the square of its atomic number, and on the other hand, the energy loss is inversely proportional to the square of its velocity. Hence, the velocity i.e. β dependent on energy loss, needs to be calibrated. Furthermore, it is necessary to calibrate the position dependence of the energy-loss because the charge collection is reduced near the walls of the MUSIC detector.

For the calibrations of the MUSIC detector, two methods can be used. Either the FRS is set for the primary beam, following a scan of the beam over the MUSIC active area in the x direction, or the fragment which covers the full width of the horizontal area can be used. In this work, the latter method using the fragment covering the full width of the horizontal area was used. Afterwards, the resulting energy-loss can be plotted as a function of the position.

The equation for the position-dependent energy-loss calibration is as follows [85]

$$dE_c = dE \cdot \frac{a_0}{a_0 + a_1 \cdot x + a_2 \cdot x^2 + a_3 \cdot x^3 + a_4 \cdot x^4 + a_5 \cdot x^5 + a_6 \cdot x^6}, \tag{2.24}$$

where dE is the total energy-loss measured in all eight anodes, coefficients a_i are determined from the sixth-order polynomial fit to the spectra where the energy-loss is plotted as a function of the position, and x is the measured position by the TPCs. The data measured for the scintillator calibrations (see Section 2.3.5) can be used for the velocity-dependent calibration. For the velocity-dependent energy-loss calibration, the following expression is used

$$v_{cor} = b_0 + b_1 \cdot \beta + b_2 \cdot \beta^2 + b_3 \cdot \beta^3 + b_4 \cdot \beta^4, \tag{2.25}$$

where the coefficients b_i are determined from the fourth order polynomial applied into the spectrum of energy-loss as a function of β measured with a primary beam with different energies. The final determined Z is then calculated using Equation of 2.24 and 2.25 as follows

$$Z = Z_{primary} \cdot \sqrt{\frac{dE_c}{v_{cor}}} + Z_{off}, \tag{2.26}$$

where $Z_{primary} = 82$ is the charge of the primary beam, and Z_{off} is an offset to improve the charge spectrum fit. All calibration parameters used in the β-decay analysis can be found in Ref. [67].

2.3.5 Plastic scintillator

Plastic scintillator detectors made of Bicron (BC420) are used for the *ToF* measurement at the FRS. These detectors include two photomultiplier tubes, at the *F2* [86], and at the *F4* [87], equipped at the left and right side of the plastic scintillators. The dimensions of these detectors at the *F2* are 200 mm x 45 mm in the x and y directions, respectively, with the thickness of 5.09 mm [88]. Furthermore, the scintillators at the *F4* have dimensions of 200 mm x 100 mm with the thickness of 1 mm.

Calibrations

Once the calibrations of TPCs are done, it is possible to determine the position of the primary beam and fragments. Then, for the calibration of scintillator detectors, two procedures can be applied. The primary beam with at least three well-known energies or well-known targets can be used. In the current work, for the S468 experiment, five different beam energies were used to calibrate scintillators. At

first, the primary beam position was centred in the focal planes *F2* and *F4* with an angle of 0 mrad (with respect to the central axes). Thereafter, the SEETRAM, scintillators, *F2* degrader wedge, and TPCs at the *F2* and *F4* were set individually in the beam line, and corresponding changes from the centre position and respective $B\rho$ values were saved.

Finally, the time difference between scintillators at the *F2* and *F4* is measured, and the *ToF* is calculated and plotted as a relative velocity function ($\beta = v/c$). Then the linear calibration can be done as presented in Section 2.2.3.

3   PERFORMANCE MEASUREMENTS OF THE GEM-TPC DETECTOR 2016

In 2016, the GEM-TPC detector prototype (HGB4) in the twin configuration [32] was tested at GSI at the FRS using the ^{12}C and ^{124}Xe beams, with the energies of 600 MeV/u. The beam intensity varied from kHz/spill to a few MHz/spill. Throughout this chapter, the GEM-TPC refers to the prototype GEM-TPC in the twin configuration. The 1st GEM-TPC denotes the first unit of the GEM-TPC, while the 2nd GEM-TPC refers to the second unit of the GEM-TPC.

This in-beam test aimed to study the performance of the GEM-TPC and the response of the integrated electronics. As reference detectors, two conventional TPCs (TPC41 and TPC42) were used together with a plastic scintillator (SC41) which was used for the triggering (see the dimensions of the detectors in Fig. 3.1b).

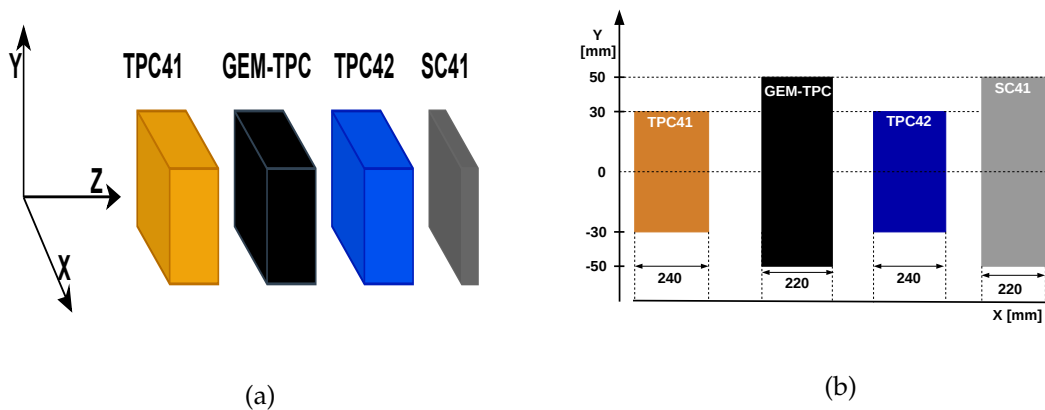(a)   (b)

Figure 3.1: (a) A schematic view of the experimental setup together with the coordinate system. The GEM-TPC was placed in between conventional TPCs (TPC41 and TPC42), and the plastic scintillator (SC41) placed downstream in the beamline at the final focal plane *F4* of FRS. (b) Dimensions of the detectors in the horizontal and vertical plane.

Figure 3.1a shows the experimental setup and coordinate system used in the analysis. The GEM-TPC was placed between the TPCs and the SC41 downstream from the GEM-TPC.

3.1 Readout electronics

The GEM-TPC has two options for reading out the measured signals in each unit. Firstly, the signal can be obtained from the bottom of the third GEM foil and, secondly, from the individual strips of the anode plane.

In this in-beam test, the readout electronics included GMX-NYXOR cards [32] for reading the analogue signals from the strips, and VV50-2 charge sensitive preamplifiers [89], referred to as preamplifiers hereafter, for reading the signals from the bottom of the third foil. Each GMX-NYXOR card has two n-Xyter chips [90], with 128 channels each. The n-Xyter chip measured the amplitude and timing information of strip signals exceeding a threshold. In total, four GMX-NYXOR cards and two preamplifiers were used to read signals of the GEM-TPC.

The collected data was then transmitted to the PCI-Express Optical Receiver (PEXOR) [91], which served as the connection between the front-end cards and the DAQ (Data Acquisition) computer.

To ensure data synchronization i.e. starting and stopping the data taking, the PC-based Trigger Module (TRIXOR) [92] was used and controlled by the PEXOR. The Multi Branch System (MBS) [93] was utilized to synchronize data from all detectors, ensuring that all events have the same timestamp value, and sending signals to the data storage.

3.2 Data flow

The signals obtained from the bottom of the third GEM foil provide information on the timing and the charge induced by the event. The timing can be utilized to calculate the y position and perform the performance analysis of the detector. On the other hand, the signals from the strips of the anode plane can be used to determine both the x and y positions of the event, the measured charge, and the cluster strip multiplicity, which is the number of fired strips within one trigger.

The signals measured from the bottom of the third foils were transported to the preamplifiers, while the signals from the strips were read out using the GMX-NYXOR cards, hereafter denoted as GEMEX. Subsequently, the clusterization was done for the strip signals (see details in Section 2.3.3). Two reconstructed clusters

are shown in Fig. 3.2. The difference of about three strips between their mean values is obtained for this event. Previous findings indicated the difference of 2 mm in the cluster positions between the GEM-TPCs along the x direction [32]. However, with the pitch of 0.4 mm, the observed difference of three strips now corresponds to 1.2 mm, which can be due to the misalignment of anode planes or an angle of the incoming event.
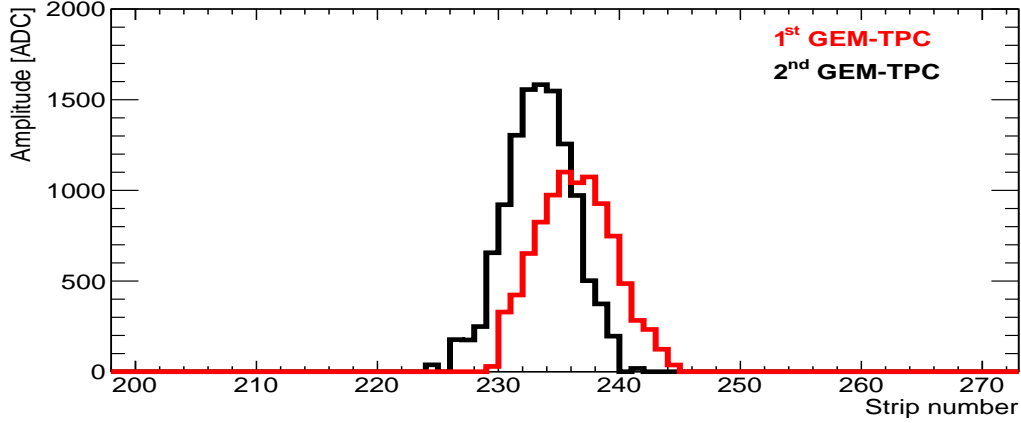

Figure 3.2: Reconstructed clusters for the carbon beam from the same event in both the 1st and 2nd GEM-TPC, shown in **red** and **black** lines, respectively.

3.3 Calibrations

3.3.1 TPC calibrations

To calibrate the TPC41, the standard calibration method [31] described in Section 2.3.2 was used. In the case of TPC42, due to the insufficient calibration data using the carbon beam for the TPC42, the calibration method explained in Ref. [1] and in Section 2.3.3 was used. The determined calibration parameters for the carbon beam for both coordinates are shown in Tables 3.1 and 3.2. It can be observed that the drift velocity remains almost the same for all anodes within the TPC41 and the TPC42.

Table 3.1: Determined calibration parameters for the carbon beam in the y direction for the TPCs.

Detector	Parameter	Anode			
		1	2	3	4
TPC41	$v\left[\frac{\mu m}{ns}\right]$	36.4(1)	36.8(1)	37.2(1)	36.7(1)
TPC41	$y_{off}[\mathrm{mm}]$	-71.5(2)	-72.5(2)	-74.0(2)	-73.1(2)
TPC42	$v\left[\frac{\mu m}{ns}\right]$	42.1(1)	42.4(1)	42.3(1)	42.1(1)
TPC42	$y_{off}[\mathrm{mm}]$	-71.5(1)	-69.7(1)	-71.0(1)	-70.5(1)

Table 3.2: Determined calibration parameters for the carbon beam in the x direction for the TPCs.

Detector	Delay line	$A\left[\frac{\mu m}{ns}\right]$	x_{off}[mm]
TPC41	1	80.8(2)	-1.8(1)
	2	82.0(2)	-3.2(1)
TPC42	1	74.3(2)	-1.8(1)
	2	75.8(3)	0.9(1)

Figure 3.3 shows the calibrated position spectrum of the calibration grid using the carbon beam in all anodes of the TPC41. The measured positions of the scintillator fibers of the grid are shown in Table 3.3. The spacing of 6.6(2) mm and 5.4(2) mm in the y direction, and spacing of 12(2) mm in the x direction between fibers are found with the TPC41.
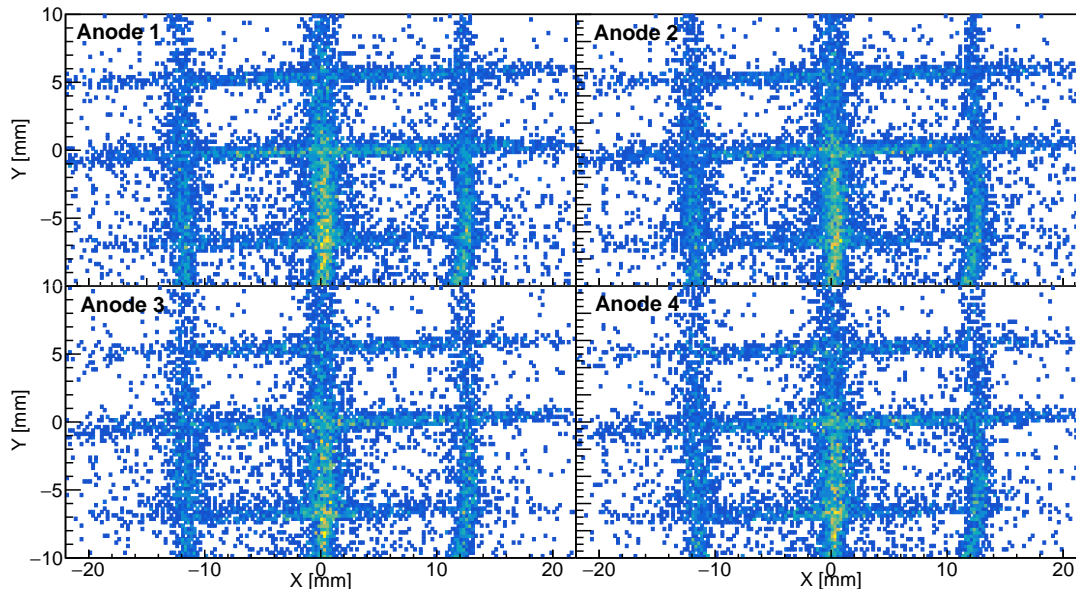

Figure 3.3: The calibration grid measured with the carbon beam in each anode of the TPC41.

Table 3.3: Measured positions of the calibration grid with the carbon beam (triggered by TPC41 calibration grid). The measured positions are relative to the zero position of TPC41 detector. Additionally, here note that the y position for the TPC42 is calculated using three anodes since the signals of one anode were not collected.

Detector	Coordinate	Peak position [mm]		
		Left	Middle	Right
TPC41	x	-11.8(1)	-0.2(1)	12.2(1)
	y	-6.6(1)	0.0(1)	5.4(1)
TPC42	x	-12.0(1)	0.1(1)	11.9(1)
	y	-7.5(10)	-2.6(5)	2.6(10)
1st GEM-TPC$_{GEMEX}$	x	-9.3(1)	2.9(1)	14.8(1)
	y	-6.3(1)	-0.2(1)	5.6(1)
2nd GEM-TPC$_{GEMEX}$	x	-10.0(1)	2.0(1)	13.5(1)
	y	-6.4(1)	-0.1(1)	5.5(1)
1st GEM-TPC$_{PreAmp}$	x	-9.2(1)	2.9(1)	14.7(1)
	y	-6.4(1)	-0.2(1)	5.5(1)
2nd GEM-TPC$_{PreAmp}$	x	-9.9(1)	1.9(1)	13.6(1)
	y	-6.3(1)	0.0(1)	5.7(1)

3.3.2 GEM-TPC calibrations

In order to measure the y coordinate in the GEM-TPC, the drift velocity calibration is required, as explained in Section 2.3.3. The calibration process utilizes events triggered by the scintillator grid of the TPC41 and projects them into the GEM-TPC. In the position spectrum measured by GEM-TPC, it becomes possible to identify three peaks separated by a known distance. For further information regarding the calibration method, see Ref. [1].

The determined calibration parameters for the carbon beam are presented in Table 3.4, with the field cage electric fields of 133.3 V/cm and 130.1 V/cm in the 1st and 2nd GEM-TPC, respectively. The measured drift velocities in the 1st and 2nd GEM-TPC, using either preamplifiers or GEMEXs, are in good agreement with a calculated drift velocity of 55.0(2) $\frac{\mu m}{ns}$ from a electric field of 130 V/cm. Moreover, the observed difference of about 15 mm in the offset parameter y_{off} comes from the delayed timing signals of the 2nd GEM-TPC. The reconstructed calibration grid using the times for the clusters taken from the preamplifiers and GEMEXs in the 1st and 2nd GEM-TPC are shown in Fig. 3.4.

The measured distances between the scintillator fibers of the calibration grid at the GEM-TPC are shown in Table 3.3. The obtained spacing between fibers is in very good agreement with the spacing measured at the TPC41. Moreover, a measured offset of 1.0(2) mm can be seen between the 1st and 2nd GEM-TPC at the fiber position of $x = 0$ mm. Earlier the offset of 2 mm with ^{124}Xe beam was reported without the clusterization or strip equalization [32].

Table 3.4: Determined calibration parameters for the carbon beam in the y direction for the GEM-TPC.

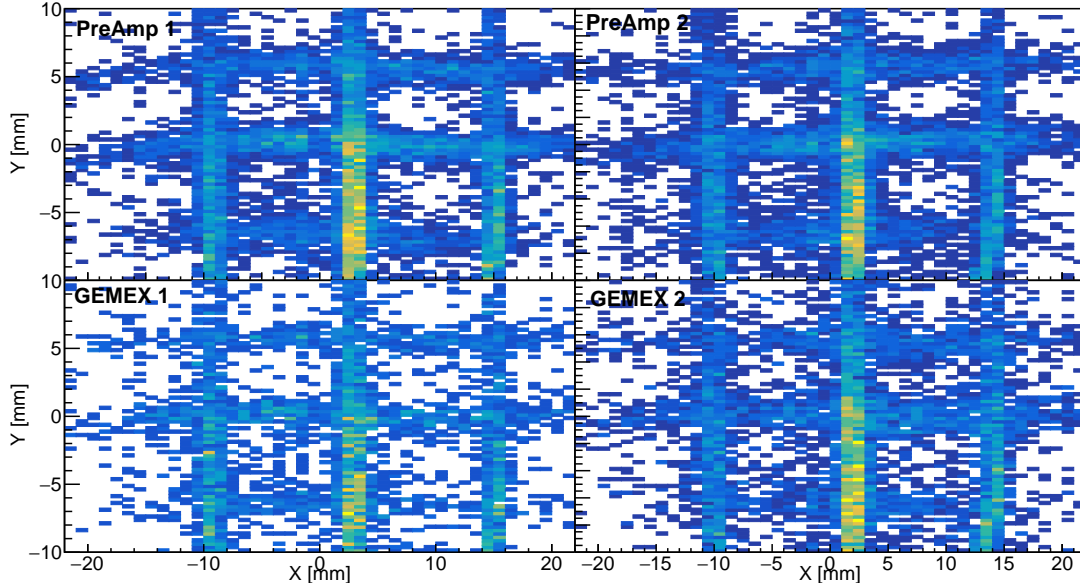| Detector	Data measured	$T_A[\frac{\mu m}{ns}]$	$y_{off}[mm]$
1st GEM-TPC	Preamplifier	53.6(3)	-75.9(4)
	GEMEX	54.8(6)	-61.4(6)
2nd GEM-TPC	Preamplifier	-54.2(4)	55.3(4)
	GEMEX	-55.7(5)	40.9(4)

Figure 3.4: The calibration grid measured with the carbon beam using the cluster times from the preamplifiers and GEMEXs in the 1st and 2nd GEM-TPC when the trigger is taken from the TPC41 calibration grid.

3.4 Alignments

Once the calibrations are completed, the alignment of the detectors is required in the beam coordinate system. In the present work, the alignments were performed offline due to the lack of a suitable data set taken with the primary beam and the beam line slits set in well-defined positions.

The offline alignment process used for the present analysis is the following:

1. Use the beam at position $x = 0$ mm and $y = 0$ mm
2. Determine the measured positions of the TPCs, 1st GEM-TPC, and 2nd GEM-TPC
3. Calculate the offsets for all the detectors to move them at the position $x = 0$ mm and $y = 0$ mm
4. In all beam positions in the x and y directions check aligned positions in all the detectors

The measured positions with the carbon beam with the electric fields of 241.3 V/cm and 234.2 V/cm in the 1st and 2nd GEM-TPC respectively, and TPCs before the offline alignment process are shown in Table 3.5.

Table 3.5: Measured positions with the carbon beam at the beam position x = 0 mm and y = 0 mm in the offline alignment process. Errors of the values in the table represent measured sigma values of the Gaussian fit, which was used to determine the position.

Detector	Position [mm]	
	x	y
TPC41	-2.7(16)	-1.2(12)
TPC42	-1.8(14)	0.7(18)
1st GEM-TPC$_{GEMEX}$	-0.4(15)	7.4(12)
2nd GEM-TPC$_{GEMEX}$	-1.1(15)	-2.1(12)
1st GEM-TPC$_{PreAmp}$	-0.4(15)	5.5(10)
2nd GEM-TPC$_{PreAmp}$	-1.1(15)	-0.2(9)

Figure 3.5 shows the aligned positions with the carbon beam obtained after the offline alignment process for all the beam positions in the x direction with the field cage electric fields of 241.3 V/cm and 234.2 V/cm in the 1st and 2nd GEM-TPC respectively. A good correlation between the measured positions and their corresponding beam positions can be observed across all the beam positions. Furthermore, Fig. 3.6 shows a strong correspondence in the correlation plots between the calculated positions of the events determined with the TPCs (denoted as the extrapolated position) at the locations of the GEM-TPCs and the measured positions at both the 1st and 2nd GEM-TPCs. The data points in the plot align closely along a 45-degree line, indicating consistency between the extrapolated and measured positions.
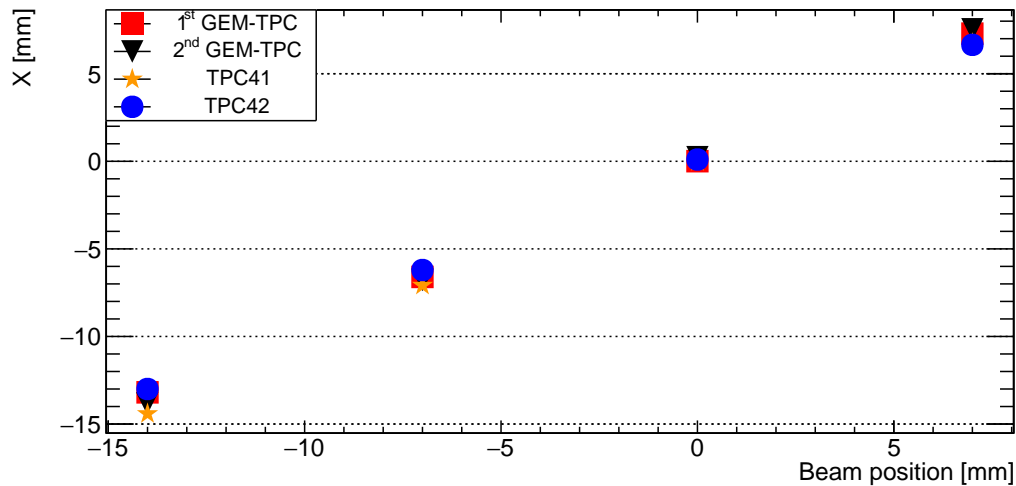

Figure 3.5: Aligned positions measured with the carbon beam in the x direction in each detector at different beam positions.
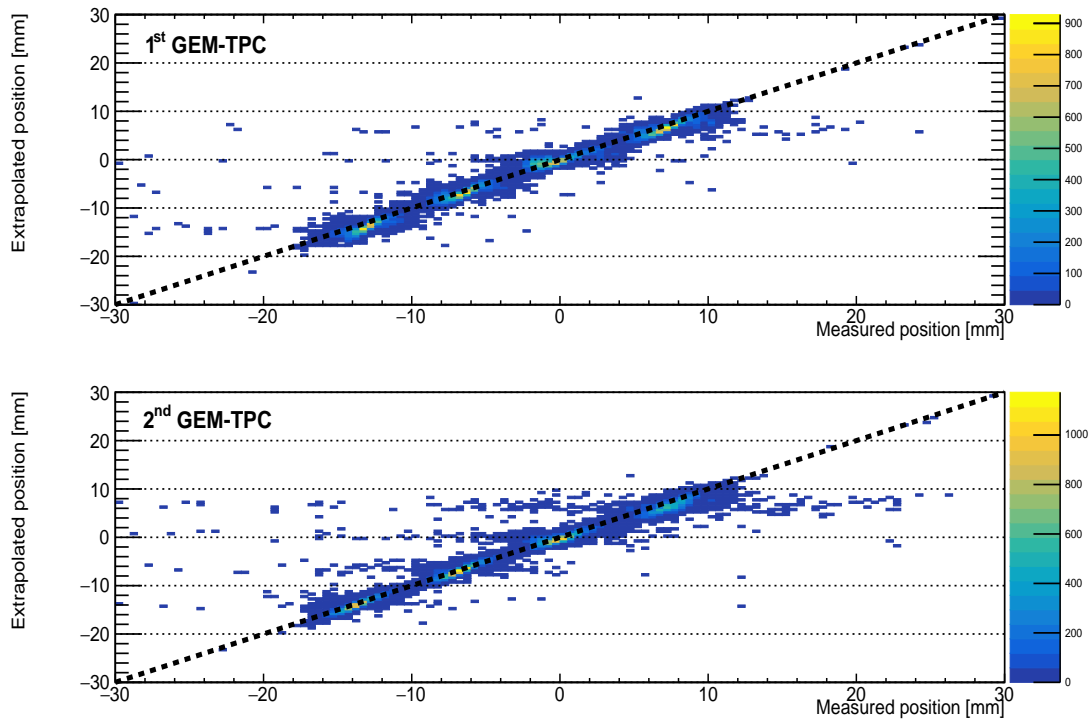
Figure 3.6: Position correlations between the extrapolated and measured positions at the GEM-TPC location, using the carbon beam in the x direction in the 1st and 2nd GEM-TPC detectors. The 45-degree lines are shown **black** dashed lines.

3.5 Results

The following subchapters show the results of analyses of the GEM-TPC performance. These analyses include the control sum analysis and the measured resolutions in the x and y directions, conducted for the events with a cluster multiplicity of one, i.e. the number of clusters within one scintillator trigger is one. The analyses were performed using the carbon and xenon beams. At the end of this chapter, Table 3.7 shows a summary of parameters and results obtained from the performance analysis. This table also shows the detection efficiencies measured during various analyses.

3.5.1 Control Sum

The twin design of the GEM-TPC was developed to achieve higher count rate capabilities [80], which is one of the requirements for the operation at the Super-FRS. Furthermore, the twin design enables the measurement of the Control Sum (CS), which can be used for several purposes, such as associating hits from the same event, reducing noise, and rejecting pile-ups. The CS can be calculated using the following expression:

$$CS = t_1 + t_2 - 2 \cdot t_{ref},\tag{3.1}$$

where t_1 and t_2 represent the measured drift times in the first and second unit of the GEM-TPC, respectively, and t_{ref} is the measured reference time from SC41.

If the focused primary beam is parallel to the z coordinate (see Fig. 3.1a), it is expected that the CS should remain constant. Therefore, it allows for its utilization in the performance analysis of the GEM-TPC. In order to study the CS in the current work, the electric field of the GEM-TPC field cages was changed from 150 V/cm to 300 V/cm.

At first, to confirm the parallel beam of carbon during the voltage scan of the electric field, the trajectories of the events were analysed in order to compute the angles of trajectories. The TPCs were utilized to measure the mean angles (with respect to the central axes), which remained close to 0 mrad throughout the scan. Additionally, approximately 68.3 % of the events fall within a range of about 4 mrad.
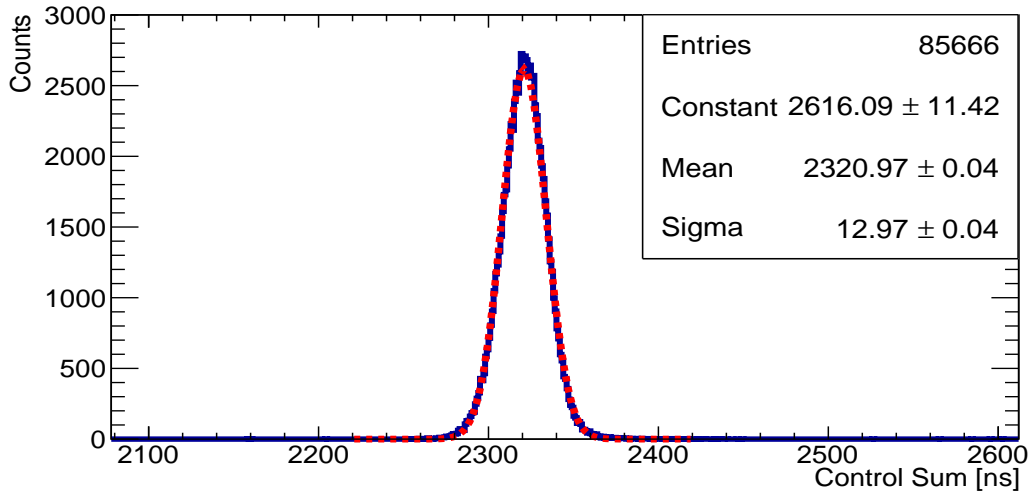

Figure 3.7: The CS values measured using the carbon beam. The CS values are shown by a blue line, while the **red** dashed line represents the Gaussian fit. These measurements were taken with the preamplifiers, with the electric field of 150 V/cm in the field cages of the GEM-TPC.

In Fig. 3.7, the CS distribution at the beam position $x = 0$ mm, measured by the preamplifiers, with the electric field of 150 V/cm is shown. Moreover, in Fig. 3.8, the measured mean CS values with different electric fields are shown, represented by black circles, and the corresponding sigma values with the red triangles. Additionally, the blue squares represent the sigma values obtained with an angle cut of 1 mrad, which means only the events with an angle within ± 0.5 mrad, were considered. In summary, no significant variations in the width of the measured CS distribution across the different electric fields were found. Moreover,

as expected, selecting events with a small incoming angle leads to a narrower CS distribution.
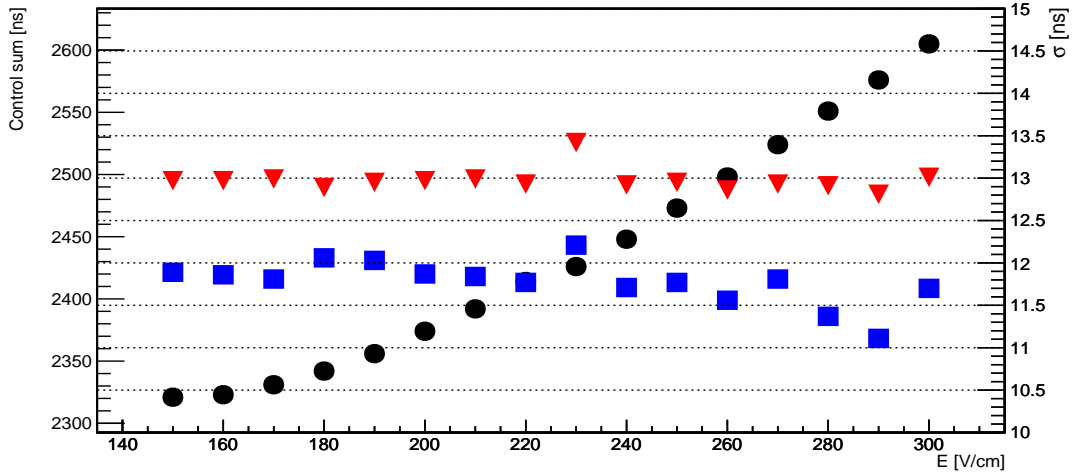

Figure 3.8: Obtained mean control sum values with the carbon beam and their corresponding sigma values, measured with different electric fields in the field cage. **Black** circles represent the measured control sum values, the corresponding sigma values by **red** triangles, and the sigma values with the 1 mrad angle cut for the events are represented by **blue** squares. The error bars are within the markers.

In order to investigate the CS at different locations within the GEM-TPC, the xenon beam was moved in the x and y directions while maintaining the constant electric field of 200 V/cm. The beam was moved from -3.8 mm to -75.9 mm in the x direction and from -10.5 mm to 13.2 mm in the y direction. The measured CS values (black circles) and their corresponding sigma values (red triangles) are shown in Fig. 3.9. It can be observed that the sigma values remain almost constant across all positions, and there are no big variations in the CS values. Additionally, the measured CS values (black circles) and corresponding sigma values (red triangles) obtained at various positions in the y direction are shown in Fig. 3.10. In this figure, the mean CS value varies depending on the incoming angle of the events, as expected. In contrast, no significant variations in the sigma values were found in the y direction.
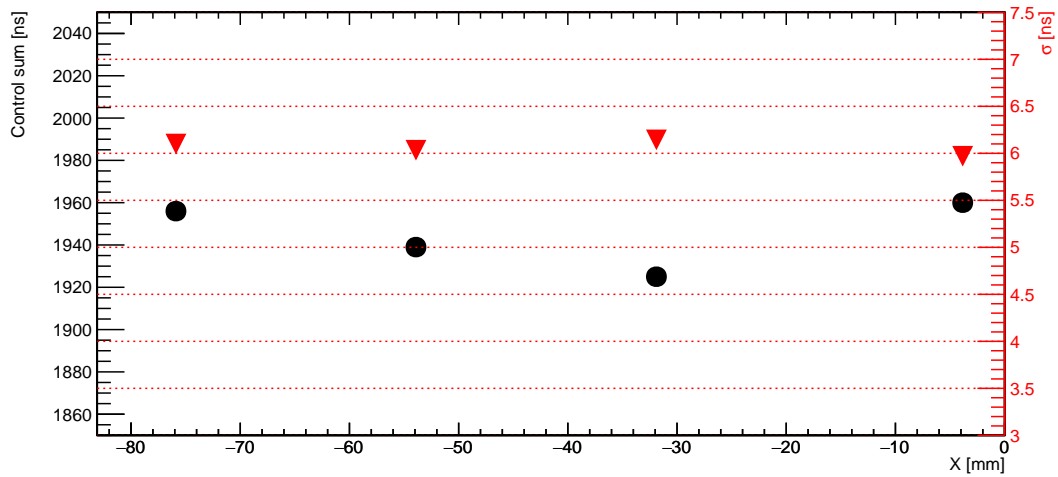
Figure 3.9: The mean CS values obtained with the xenon beam, and their corresponding sigma values, measured with different positions in the *x* direction. The measured CS values are denoted by **black** circles, while the corresponding sigma values are represented by **red** triangles. The error bars are within the markers.

Figure 3.10: The mean CS values obtained with the xenon beam, and their corresponding sigma values, measured with different positions in the *y* direction. The measured CS values are denoted by **black** circles, while the corresponding sigma values are represented by **red** triangles. The error bars are within the markers.
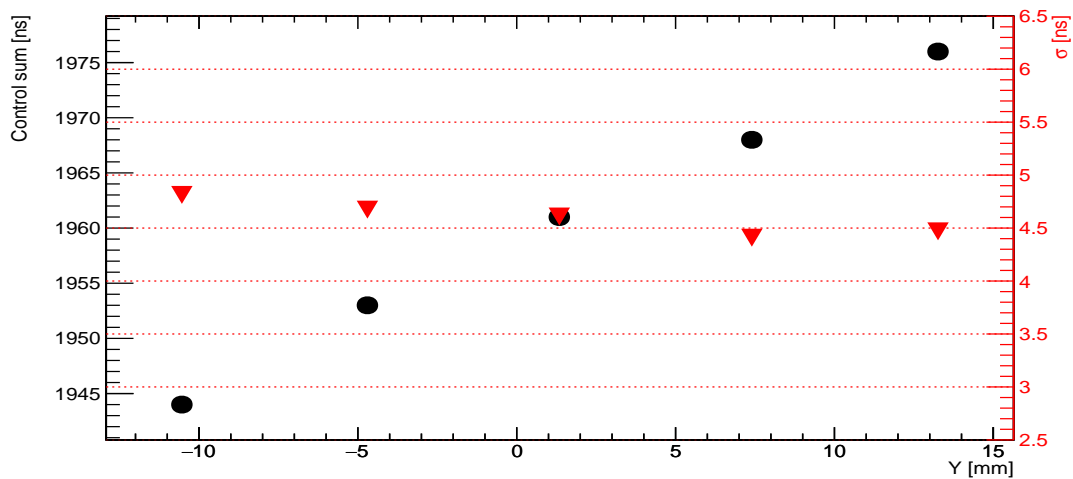
In the previous studies of the GEM-TPC, the CS was measured using calcium, bismuth, and uranium beams [32, 94]. When the uranium beam was used, the measured sigma of the CS was approximately 14 ns, and it slightly increased with the higher electric field. The difference with the present measurement, where the sigma of CS about 13 ns with the carbon beam and < 6.5 ns with the xenon beam were observed, is that the incoming angle of the events was not previously measured, which influences the broader distribution observed. Additionally, the performance analysis of the GEM-TPC is influenced by the beam optics of the separator, which affects the incoming angles of events, as can be seen in the CS

sigma values obtained with the carbon and xenon beams. In the case of the carbon beam, the position distribution of the beam was larger in all detectors, while the xenon beam showed a narrower beam width.

3.5.2 Beam profiles

After the calibrations, alignments, and CS analysis, the beam profile was determined with the carbon beam at the beam position $x = 7$ mm, and $y = 0$ mm, with the electric fields of 241.3 V/cm and 234.2 V/cm in the 1st and 2nd GEM-TPC respectively. The determination is accomplished by utilizing the measured times from both GEMEXs and preamplifiers, as shown in Fig. 3.11. The beam profile at the TPCs can be seen in Fig. 3.12. For the beam profile determination, the CS within 3σ, the angle cut of 1 mrad, and the trigger multiplicity equal to one are required.
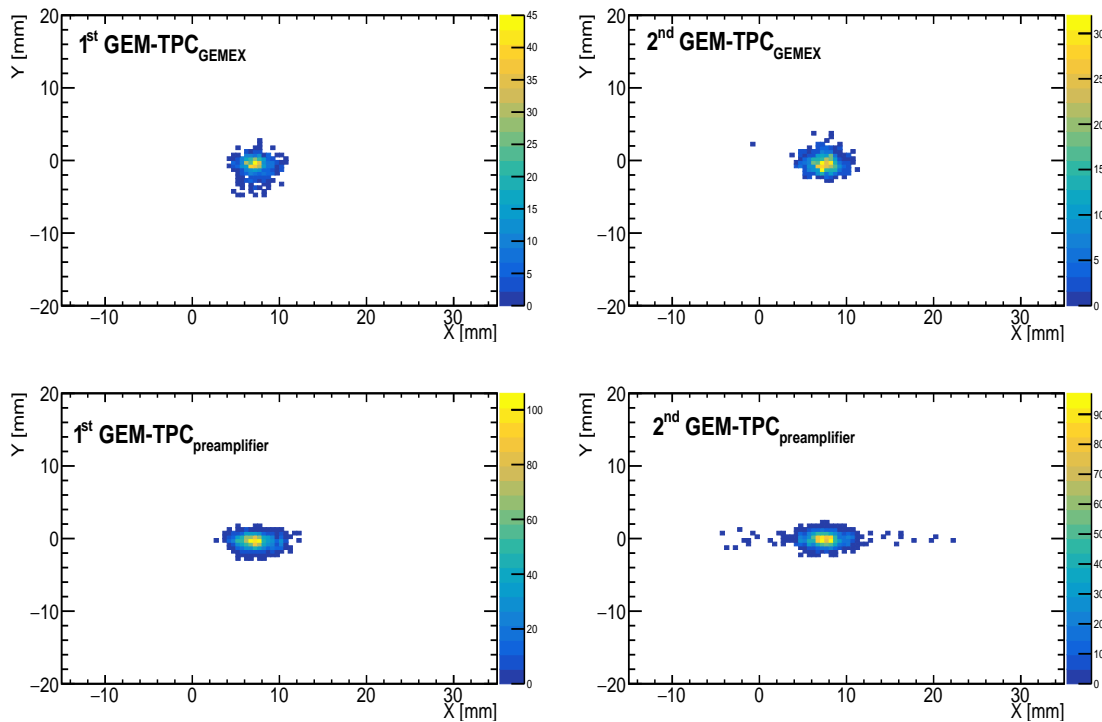

Figure 3.11: Beam profiles with the carbon beam at the beam position $x = 7$ mm in the 1st, and 2nd GEM-TPC determined using times measured by GEMEXs and preamplifiers.

The determined beam profiles are in very good agreement, regardless of whether the time of the cluster was determined using GEMEX or preamplifier. Furthermore, as expected, the beam profiles consistently remain at $x = 7$ mm, and $y = 0$ mm.
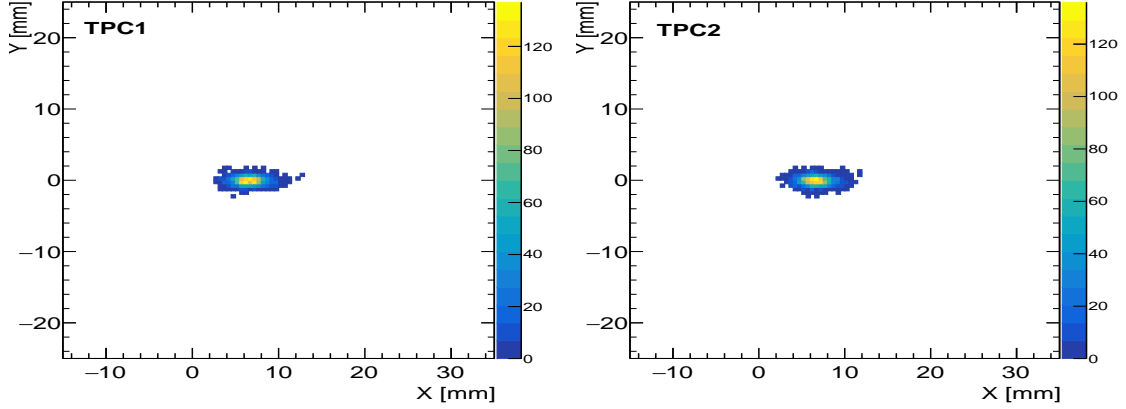
Figure 3.12: Beam profiles with the carbon beam at the beam position $x = 7$ mm in the TPCs.

3.5.3 Resolutions

The resolutions of the 1st and 2nd GEM-TPC were measured by using the residual distributions, similarly as described in Ref. [1]. The residual distributions were generated by the values of the difference between the measured position in the GEM-TPC and the extrapolated position at the corresponding location, calculated using the TPCs. In order to obtain the residual distribution, the extrapolated positions, denoted as Ext_{pos1} and Ext_{pos2} for the 1st and 2nd GEM-TPC, respectively, can be calculated using the following equation

$$Ext_{pos1/pos2} = \frac{tpc2_{pos} - tpc1_{pos}}{d_1} \cdot d_2 + tpc1_{pos}, \tag{3.2}$$

where the $tpc1_{pos}$, and $tpc2_{pos}$ represent the measured positions at the TPC41 and TPC42, respectively. The value of $d_1 = 1300$ mm corresponds to the distance between the TPCs. The distance between TPC41 and either the 1st or 2nd GEM-TPC, denoted as d_2, is 223.5 mm or 333.5 mm, respectively.

The sigma of the residual distribution contains the quadratic sum of the resolution of the GEM-TPC and tracking uncertainty (see Equation 4.3) [1]. In the analysis of the carbon and xenon beam, it was assumed that the tracking uncertainty consists of the internal resolutions of the TPCs, which are measured as 88 μm and 38 μm in the x and y directions [31], respectively. The examples of the measured residual distributions with the electric field of 200 V/cm at the beam position $y = -4.7$ mm are shown in Fig. 3.13a for the 1st GEM-TPC and in Fig. 3.13b for the 2nd GEM-TPC. The extracted resolutions in this beam position are 0.20(1) mm and 0.22(1) mm for the 1st and 2nd GEM-TPC, respectively.
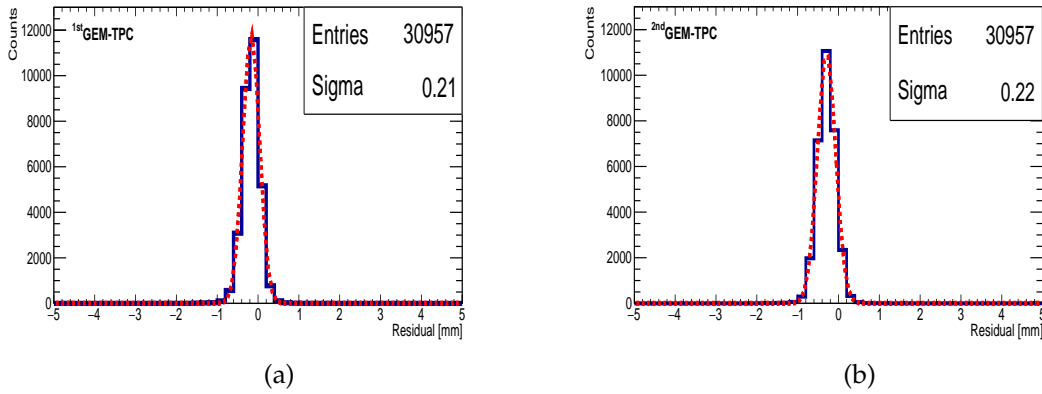
Figure 3.13: Measured residual distributions, at the beam position y = -4.7 mm with the preamplifiers in the 1st and 2nd GEM-TPC shown in Fig. (a) and (b), respectively. The Gaussian fits are shown in **red** dashed lines. The extracted resolution in this beam position is 0.20(1) mm for the 1st GEM-TPC and 0.22(1) mm for the 2nd GEM-TPC.

The measured y resolutions at different y positions in both GEM-TPCs are shown in Fig. 3.14 and 3.15 using GEMEXs and preamplifiers, respectively. These measurements were conducted using the xenon beam, with electric fields of 200 V/cm, beam intensity of 3k ions/spill, and spill length of 2 s with 1 s between the beam pulses, using both GEMEXs and preamplifiers. It can be observed that the resolutions remain about constant across different y positions in both the GEMEX and preamplifier measurements. Moreover, there is a slight difference of approximately 0.1 mm between the resolution values obtained with the GEMEX and preamplifiers. This difference can be attributed to the broader signal arrival time distribution measured in all beam positions with GEMEXs. Furthermore, there is a maximum variation of about 0.018 mm and 0.016 mm in the resolutions between the 1st and 2nd GEM-TPCs when measured with the preamplifiers and GEMEX, respectively. These differences come from the slightly narrower signal arrival time distribution. However, it is worth noting that the differences are not significantly large. Both GEM-TPCs show resolutions below the required value of 1 mm for trackers operating in the Super-FRS. The results demonstrate that both GEM-TPCs perform well and fulfil the necessary resolution criteria for their intended application.

Despite the good agreement in y resolution values between the two GEM-TPCs, the obtained results deviate from earlier measurements where the y resolution value of 125 μm was determined [32]. The difference between measurements can be attributed at least to two factors. Firstly, in the earlier measurement, clusterization was not utilized. This difference could contribute depending on how the signal arrival times were determined. Without clusterization, one method to determine the y coordinate of the event is to use signal taken from the bottom of the third GEM foil. This method aligns with the method utilized with the preamplifiers in the current work, resulting in resolution values close to previously measured ones. Secondly, in the present analysis, the tracking uncertainty was attributed only
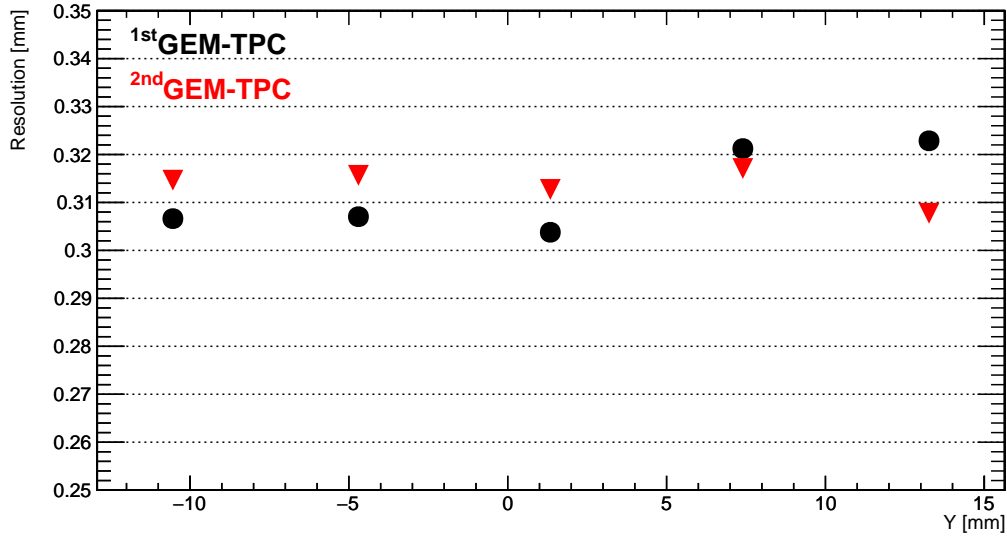
Figure 3.14: Measured y resolution of the 1st and 2nd GEM-TPC obtained using the xenon beam and GEMEXs. The 1st GEM-TPC is denoted by **black** circles, while the 2nd GEM-TPC is represented by **red** triangles.
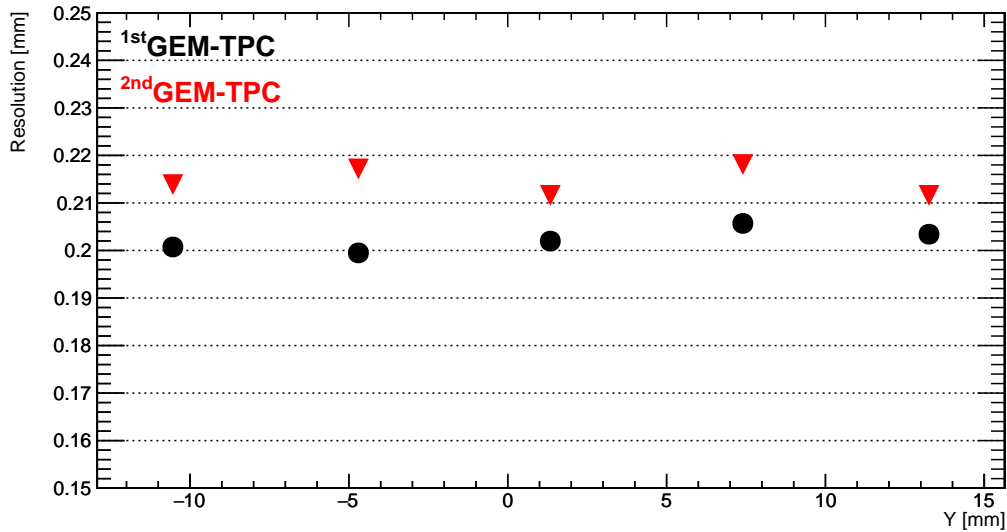

Figure 3.15: Measured y resolution of the 1st and 2nd GEM-TPC obtained using the xenon beam and the preamplifiers. The 1st GEM-TPC is denoted by **black** circles, while the 2nd GEM-TPC is represented by **red** triangles.

to the internal resolutions of the TPCs, which were assumed to be 88 μm and 38 μm, in the x and y directions [31], respectively. However, the earlier measurement might have considered additional factors in the tracking uncertainty, such as more accurate calibration and alignments, which were not possible to include in the present analysis.

Moreover, in the previous experiment, the given y resolution value is given to the whole GEM-TPC in the twin configuration, i.e. it includes both GEM-TPCs. As

a summary, the differences in data processing and consideration of the tracking uncertainty might explain the deviations observed in the y resolution values between the present and earlier measurements. Therefore, it highlighted the importance of considering the analysis technique and the tracking uncertainty when comparing results from different experiments.

The measured x-resolution values of both GEM-TPCs in different beam positions along the x direction with the xenon beam are shown in Fig. 3.16. The measurements were done with the electric field of 200 V/cm, a beam intensity of 40k ions/spill, and spill length of 2 s with 1 s between beam pulses. An angle cut of ± 3 mrad was applied to select events within the specified range, however, resulting in wide-angle distribution. This figure shows that the x resolution remains below 1 mm in all beam positions, fulfilling the requirement set for the resolution. Additionally, there is a variation in the measured resolution ranging from 0.03 mm to 0.18 mm between the GEM-TPCs, with a maximum variation of about 0.1 mms observed in the 2nd GEM-TPC across different beam positions. These variations may be attributed to the wide distribution of accepted angles in the analysed events. However, further investigations are required to confirm any differences in the position resolution across different locations of the GEM-TPCs.
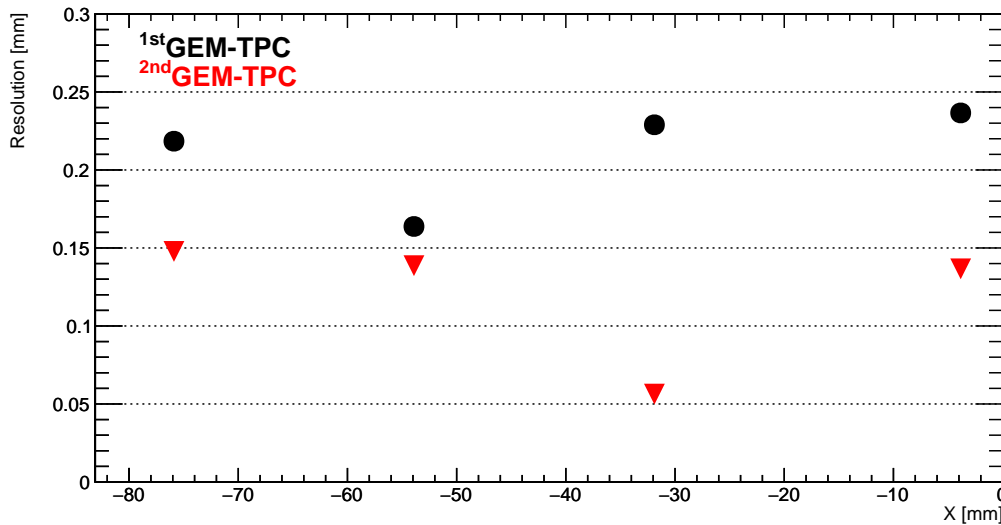

Figure 3.16: Measured x resolution of the 1st and 2nd GEM-TPC obtained using the xenon beam. The data points of the 1st GEM-TPC are drawn by **black** circles, while the 2nd GEM-TPC is represented by **red** triangles.

The obtained x-resolution values for the GEM-TPCs in the present analysis are consistent with the values reported from previous measurements, where x resolutions between 120 μm and 300 μm were reported for the GEM-TPC detector in the twin configuration. However, there are some differences between the measurements which come from several factors. Firstly, the present analysis applied clusterization, whereas the previous measurements utilized a different method for

x-position determination. Additionally, differences in consideration of tracking uncertainty could also contribute to the observed resolutions.

The summary of parameters and results obtained from the prototype GEM-TPC performance analysis are shown in Table 3.7. Whereas performance values for the TPC (parameter definitions can be found in Ref. [31]), are presented in Table 3.6. The detection efficiency of the GEM-TPC is determined by comparing the number of events at the GEM-TPC to the events triggered by the scintillator. Meanwhile, the detection efficiency for the TPC is determined by comparing events where at least one of the four control sums falls within 3σ to the events triggered by the scintillator. The detection efficiencies measured in this in-beam test indicate that the GEM-TPC maintains the detection efficiency > 95 %, while the efficiency of the TPC decreased below this with the intensity of 27 k ions/spill.

Table 3.6: Summary of parameters and performance values measured with ^{40}Ar, ^{80}Kr, and ^{238}U data for the TPC from Ref. [31].

Observable	Beam	Rate [ions/s]	Value
Tracking efficiency	^{40}Ar, ^{80}Kr	40 k	> 99 %
	^{40}Ar, ^{80}Kr	400 k	> 80 %
External resolution: x	^{238}U	-	160 μm
External resolution: y	^{238}U	-	200 μm
Internal resolution: x	^{238}U	-	88 μm
Internal resolution: y	^{238}U	-	38 μm

Table 3.7: Summary of parameters and results from GEM-TPC performance analysis. Please note that the resolution and detection efficiency values with ^{124}Xe beam for the GEM-TPCs are provided as average values measured at all beam positions. For the ^{12}C and ^{124}Xe beams, the spill length was 2 s with 1 s between the beam pulses.

Detector	Observable	Beam	Rate [ions/spill]	Value
TPC	Detection efficiency	^{124}Xe	3 k	95 %
		^{124}Xe	40 k	78 %
		^{12}C	27 k	93 %
		^{12}C	50 k	89 %
1stGEM-TPC	Detection efficiency	^{124}Xe	3 k	96 %
		^{124}Xe	40 k	99 %
		^{12}C	27 k	97 %
		^{12}C	50 k	98 %
	Resolution: x	^{124}Xe	40 k	212 μm
2ndGEM-TPC	Detection efficiency	^{124}Xe	3 k	97 %
		^{124}Xe	3 k	99 %
		^{12}C	27 k	99 %
		^{12}C	50 k	99 %
	Resolution: x	^{124}Xe	40 k	120 μm
1st GEM-TPC$_{GEMEX}$	Resolution: y	^{124}Xe	3 k	312 μm
2ndGEM-TPC$_{GEMEX}$	Resolution: y	^{124}Xe	3 k	314 μm
1st GEM-TPC$_{PreAmp}$	Resolution: y	^{124}Xe	3 k	202 μm
2nd GEM-TPC$_{PreAmp}$	Resolution: y	^{124}Xe	3 k	214 μm

4 PERFORMANCE MEASUREMENTS OF THE GEM-TPC DETECTOR 2019

The GEM-TPC detector prototype (HGB4) [32] in a single field cage configuration was tested at GSI at the FRS [30] in 2019 using a ^{238}U beam at 850 MeV/u. Since this prototype GEM-TPC was tested earlier with a uranium beam [32], the main goal of this in-beam test was to investigate its performance and response with newly integrated Low Noise Amplifier With Adaptive Gain Settings - (AWAGS) ASIC [95, 96] readout electronics using two conventional TPCs [31] as reference trackers.

Figure 4.1a shows a schematic view of the experimental setup while the dimensions of the detectors in the horizontal and vertical planes can be seen in Figure 4.1b.
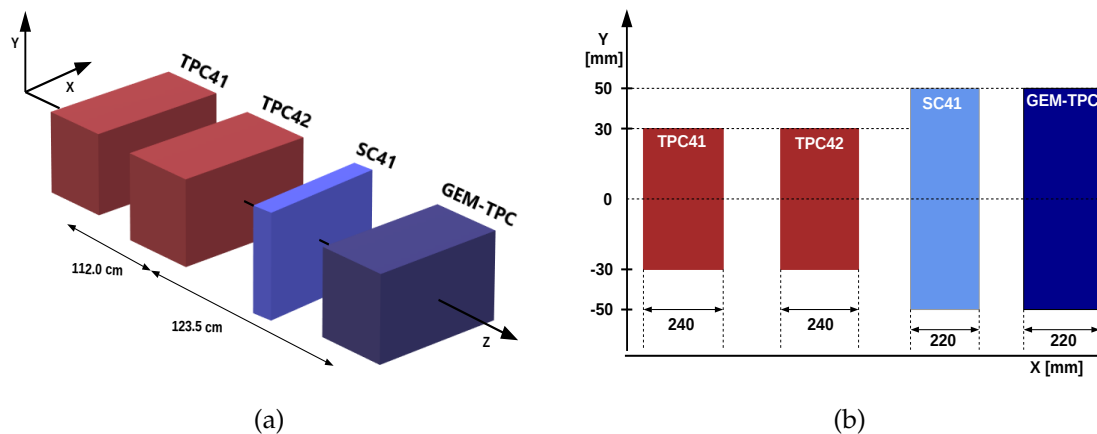

(a)   (b)

Figure 4.1: (a) A view of the experimental setup together with the coordinate system used. Two conventional TPCs (TPC41 and TPC42) and a plastic scintillator (SC41) are placed upstream in the beamline at the final focal plane *F4* of FRS. (b) The dimensions of the detectors in the *x* and *y* directions.

The experimental setup at the FRS consisted of two conventional TPCs (TPC41 and TPC42), one plastic scintillator (SC41) used for triggering, and the GEM-TPC prototype in the single field cage configuration. In this chapter, the term "GEM-TPC" refers to the GEM-TPC prototype in the single field cage configuration.

The analysis used a coordinate system as shown in Figure 4.1a, with the z-axis orthogonal to the GEM-TPC plane and parallel to the beam direction, the x-axis in the horizontal direction, and the y-axis in the vertical direction.

In the GEM-TPC, P10 (90% Ar, 10% CH_4) gas was used at atmospheric pressure and room temperature. The electric fields applied in the field cage varied from 90 V/cm to 320 V/cm. The beam delivered by the FRS was $^{238}U^{+92}$ at 850 MeV/u with a spill length ranging from 2 s to 8 s, and the intensity varied from 100 to 1k ions/spill.

4.1 Readout electronics

In Section 2.3.3, it is mentioned that the GEM-TPC in the single field cage configuration consists of 512 strips in its readout pad plane. However, in the current in-beam test, only half of the strips were read out due to the limited availability of the tested electronics. The induced signals on each strip of the GEM-TPC were collected and used to determine the coordinates of the event. Additional checks for the drift time and induced charge were performed from the bottom of the third GEM foil. Figure 4.2 shows the locations of picking up signals of the GEM-TPC.
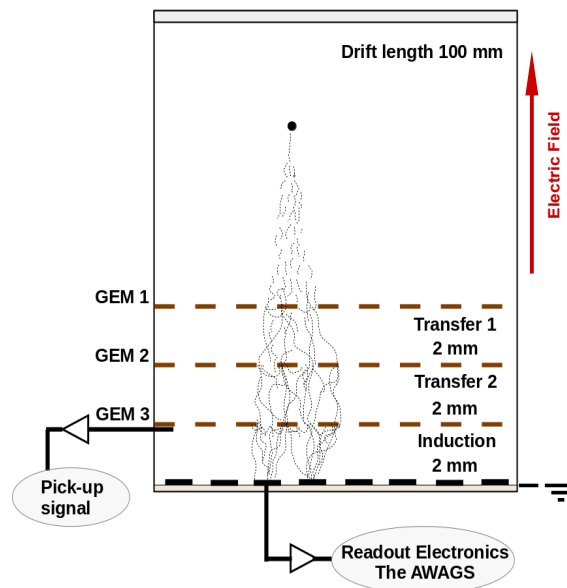

Figure 4.2: Layout view of the GEM-TPC. The triple GEM stack, field cage and positions for picking up signals are shown. The figure is adapted from [1], under the license CC BY 4.0.

The Low Noise Amplifier With Adaptive Gain Settings - (AWAGS) ASIC [95, 96] with a differential output, electronics was used. This was the first in-beam test where this electronics was tested together with the GEM-TPC with a particle beam. The strength of the AWAGS lies in its large dynamic range which is created using five separated capacitors.

The analogue signals from the AWAGS were transported to the FEBEX3b digitizer (Front End Board with optical link EXtension) [97] (see Fig. 4.3). One FEBEX3b board can produce ADC samples of 16 channels, providing 20 ns per sample with 50 MHz sampling rate. This board has 14-bit ADC for both polarities, thus providing 16 384 ADC counts for each digitized waveform. The signals generated by the GEM-TPC have negative polarities, and the effective dynamic range is therefore half of the ADC counts provided by FEBEX3b, thus 8192 ADC counts.
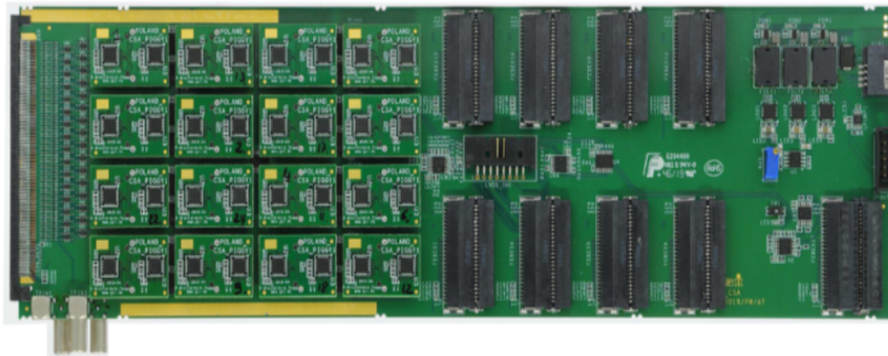

Figure 4.3: The FEBEX3b board with the AWAGS electronics. The figure is adapted from [1], under the license CC BY 4.0.

The Multi Branch System (MBS) [93] was used to collect and synchronize the data on an event-by-event basis. As a consequence, all the detectors are synchronized by the same timestamp value. From the digitizers, the data is moved to the PCI-Express Optical Receiver (PEXOR) [91], which was used to connect front-end cards to the DAQ computer. For the data synchronization, starting and stopping the data taking, the PC-based Trigger Module (TRIXOR) [92] is used, which is controlled by the PEXOR.

4.2   Data flow and Analysis method

The process for determining the signal of the strip is shown in a block diagram in Fig. 4.4. The baseline and signal sample distributions are determined as a starting point of the analysis. The mean values, i.e. the mean baseline and mean signal, are obtained using the Gaussian function. The difference between mean values is calculated for the next step, representing the measured signal in that strip. Additionally, the sigma value of the baseline distribution is collected for later use in strip equalization.
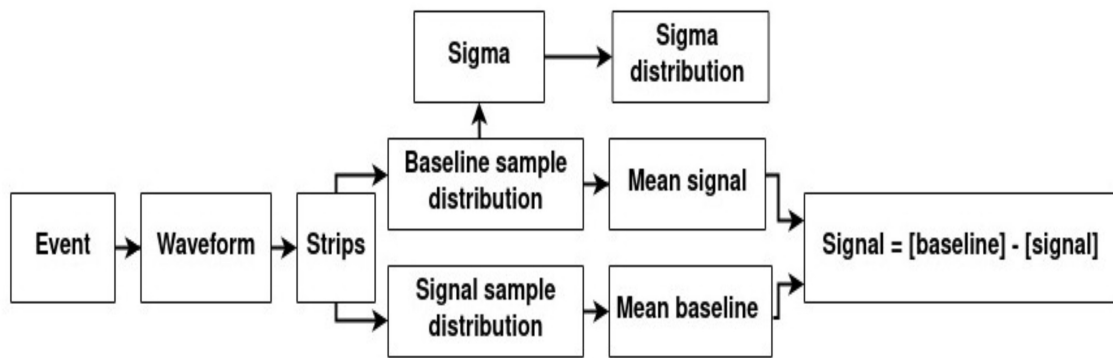
Figure 4.4: Schematics showing the process for determining the signal of the strip shown in a block diagram.

Figure 4.5a shows an example of a measured waveform from a single event in one strip. Each waveform includes 1000 samples, but the region of interest only covers the baseline and signal samples ($\sim$ 784 samples).
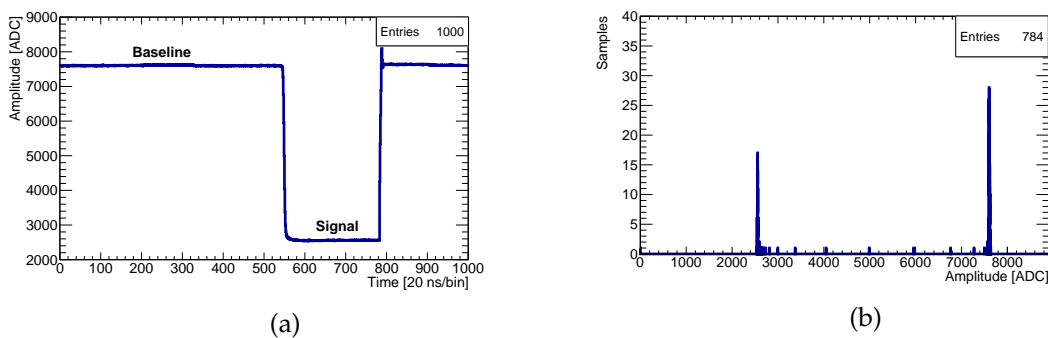

(a)

(b)

Figure 4.5: (a) A waveform measured from a single event in one strip. (b) The corresponding ADC distribution of the baseline and signal samples.

Firstly, the ADC distribution of the baseline and signal samples of an event in a single strip is determined, as shown in Figure 4.5b. Next, the pedestal is determined, which is the mean value of the Gaussian fit to the baseline samples (see Figure 4.6a). For the determination of the amplitude value of the measured signal, the signal sample distribution is fitted by the Gaussian, as shown in Fig. 4.6b. Finally, the difference between the mean values is calculated to obtain the signal value for that strip.
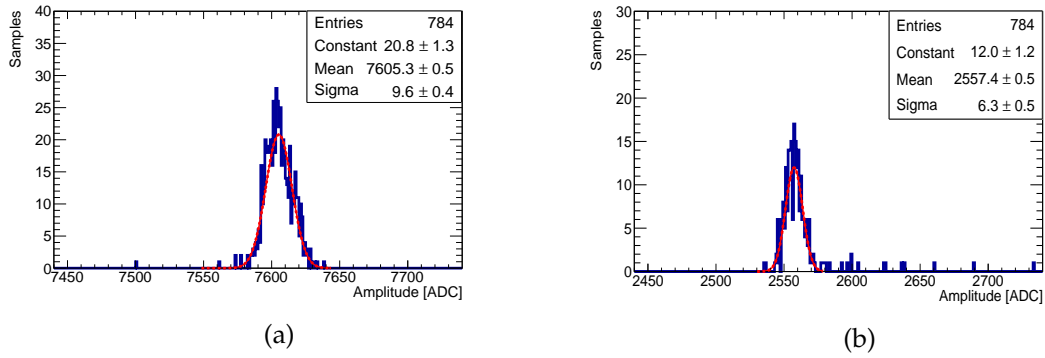
(a)

(b)

Figure 4.6: (a) An example of the baseline sample distribution with a Gaussian fit shown with a **red** dashed line. (b) Signal sample distribution with a Gaussian fit drawn with a **red** dashed line.

The clusterization process, shown in the block diagram in Fig. 4.7, is the next step in the analysis procedure. As a preliminary step for this process, the amplitude of each strip is first equalized using the sigma cut method. This method involves extracting the mean value of the saved sigma distribution (determined from the pedestal distributions), using the Gaussian fit, and multiplying the obtained mean value by a sigma cut value of 150 (see details about the sigma cut value selection in Section 4.2.4). The outcome value is subtracted from the signal amplitude of the strip, resulting in the amplitude value for that strip in the cluster. As a final step of the analysis, the reconstructed cluster is then fitted by the Gaussian fit to determine the mean channel value of the cluster, which will be used to determine the *x* position and timing of the event.
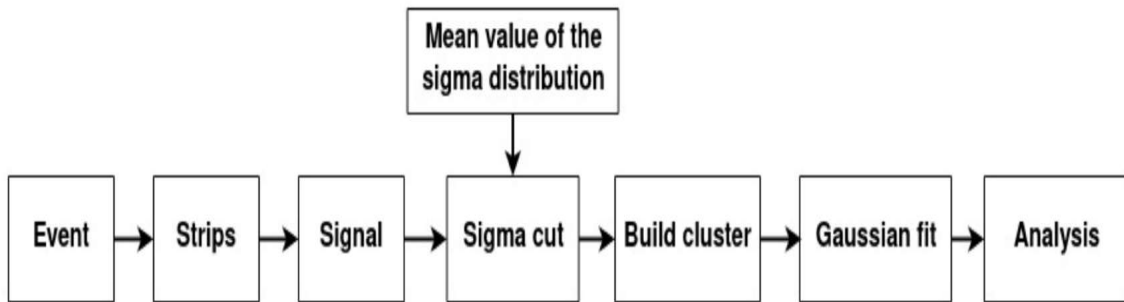

Figure 4.7: A block diagram of the clusterization process.

For a consistency check of the described analysis method, the waveforms were fitted with sigmoid fits to reconstruct the cluster. The function *f(t)* of the sigmoid fit is following

$$f(t) = P_0 + \frac{P_1}{(1 + exp(-\frac{t-P_2}{P_3}))}, \tag{4.1}$$

where the minimum level of the waveform is P_0 , P_1 is the signal amplitude, P_2 is the time bin when maximum slope occurs, and the last parameter P_3 is the maximum slope parameter. An example of the waveform with the sigmoid fit is shown in Fig. 4.8. The measured amplitudes of 5047.9(8) and 5039(15) ADC counts for the strip signal using the first described method and the sigmoid fit are in good agreement.
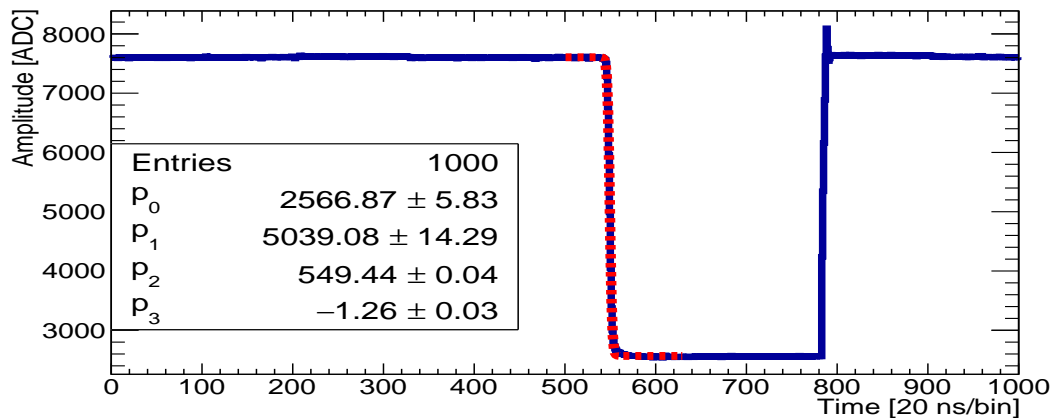

Figure 4.8: The waveform with a sigmoid fit in **red** dashed line.

4.2.1 Timing of the event

A signal arrival time of the cluster needs to be determined after the cluster reconstruction for the y coordinate calculation (explained in Section 2.3.3). Since the granularity of the digitizers is 20 ns, two methods in order to determine the time of the cluster are used.

The strip closest to the mean value of the cluster is chosen for the time determination. Then, a threshold of 100 ADC counts is applied to the leading edge of the waveform, and the signal arrival times are extracted from the crossing points at the threshold from the waveform and sigmoid fit. In Fig. 4.9, the waveform and sigmoid time projections at the threshold are shown. A good comparison is obtained between the determined times of 1289(15) ns and 1298(20) ns.

To ensure that the determined time of the cluster is not affected by the method, the possible time-walk correction is studied at three beam positions at x = -20 mm, x = 0 mm, and x = +20 mm. Fig. 4.10 shows the signal arrival time plotted as a function of the cluster amplitude, and it is evident that there is not observable slew, indicating that there is no need for the time-walk correction.
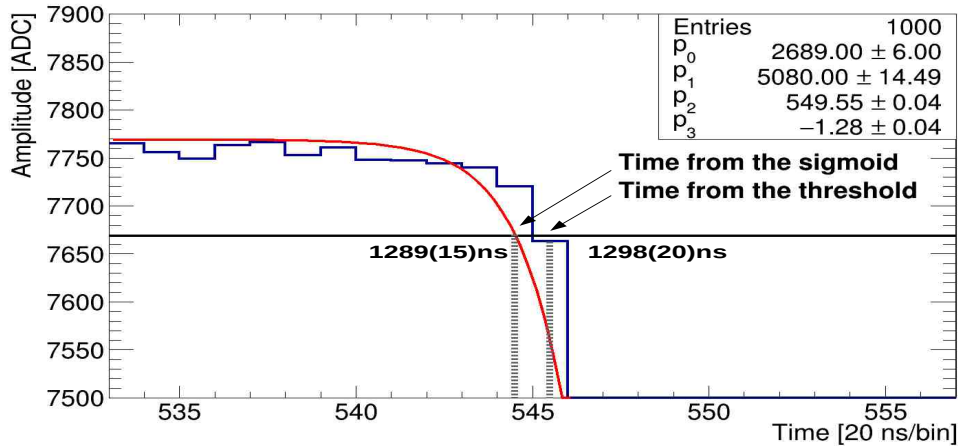
Figure 4.9: Signal arrival time determination with a threshold of 100 ADC counts. The measured times of 1289(15) ns and 1298(20) ns from the sigmoid fit in **red** and threshold are in good agreement. The figure is adapted from [1], under the license CC BY 4.0. The values of signal arrival times are added to the original figure.
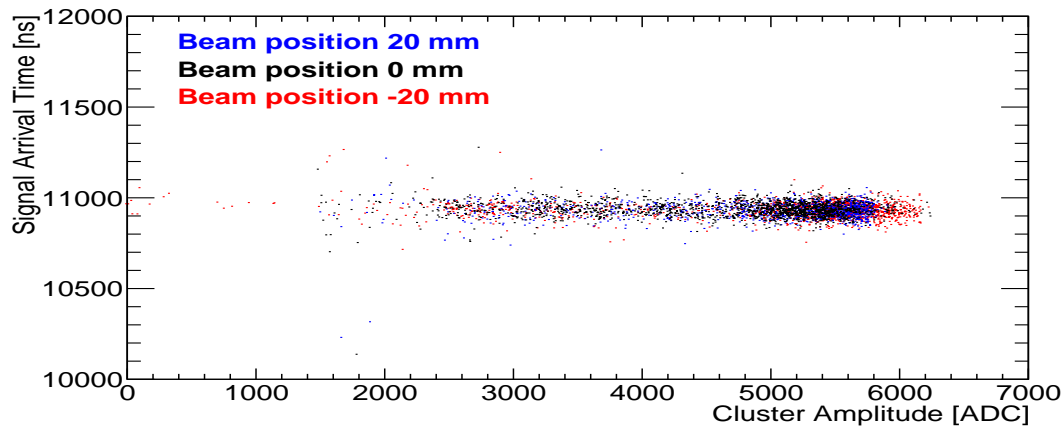
Figure 4.10: Signal arrival time of the cluster as a function of the cluster amplitude.

4.2.2 Consistency checks of the used analysis method

In Section 4.2, the process of using Gaussian fits to obtain pedestal values is explained. As an example, the determined pedestal values in each strip in the beam position $x = 0$ mm are shown in Fig. 4.11. It is evident that the pedestal values fluctuate between strips and events, which is why the sigma cut is utilized to equalize the strips.

The reduced chi-squared χ_ν^2 test [98] can be used to measure the goodness of the utilized Gaussian fit. The χ_ν^2 value close to one indicates a good agreement between the data and fit, while the values significantly larger or smaller than one indicate a poor fit.

Figure 4.11: Obtained pedestal values of each strip in the beam position $x = 0$ mm.
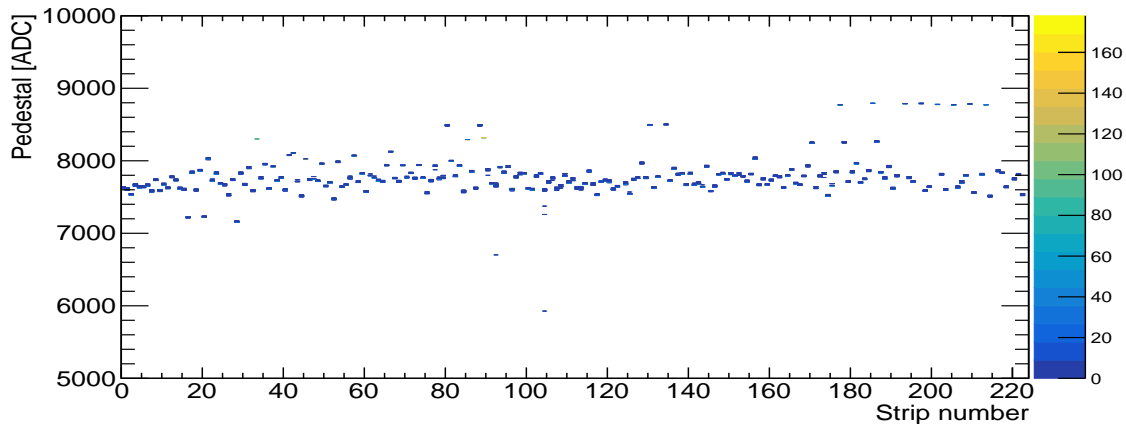
To test the goodness of the applied Gaussian fits to the baseline and signal sample distributions, χ^2_ν distributions are extracted as shown in Fig. 4.12a and 4.12b. From the signal part, the mean value of 1.256(2) is obtained. Since this value is close to one, it indicates that the chosen Gaussian fit is an appropriate selection. On the other hand, from the baseline part, the mean value of 6.44(2) is obtained, using the peak with a higher χ^2_ν value. Two peaks in this distribution and a bigger χ^2_ν value indicates that the baseline distribution is not fully Gaussian shaped. However, in the present work it can be used to estimate the value of the pedestal, since after the pedestal determination the strip signals are equalized with the sigma cut.
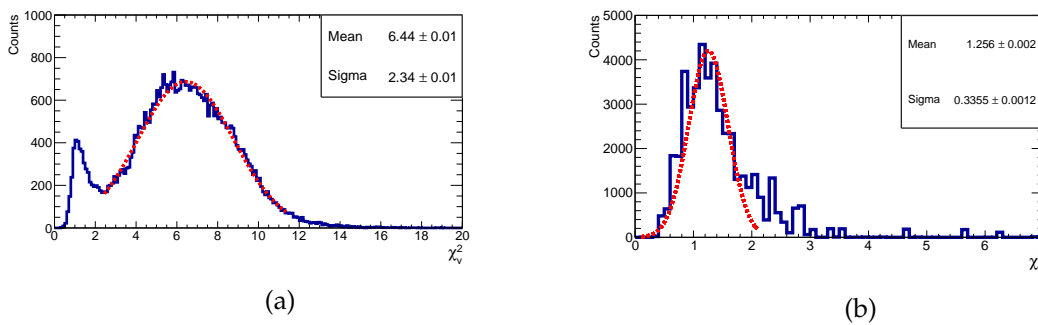
Figure 4.12: (a) χ^2_ν value distribution of all the pedestal determinations of one strip. (b) χ^2_ν value distribution extracted from all the signal distributions of one strip. In both figures, the Gaussian fit is shown with a **red** dashed line.

To summarize the consistency checks using the χ^2_ν test, the Gaussian fit used for the signal part of the ADC distribution is appropriate because the mean value of 1.256(2) was found. Additionally, the χ^2_ν distribution extracted from the baseline distributions revealed fluctuations in the baseline and indicated that it is not entirely Gaussian.

4.2.3 Sigma cut for the equalization of the strips

For the equalization of the strips, the sigma cut method is used since the baseline of the waveforms varied between events in the same strip. The sigma values obtained from the Gaussian fit in the baseline distribution were saved independently for each strip. Next, the Gaussian fit determines the mean value from the sigma distribution. This value was then multiplied by a constant, resulting in an independent factor for each strip subtracted from the measured amplitude.

Fig. 4.13 shows an example of the determined sigma distribution in one strip at the beam position $x = 0$ mm. In the next step of the sigma cut process, the mean value of 7.756 ADC counts was multiplied by the sigma cut value. The size of the sigma cut value is selected according to the study that will be discussed in Section 4.2.4.
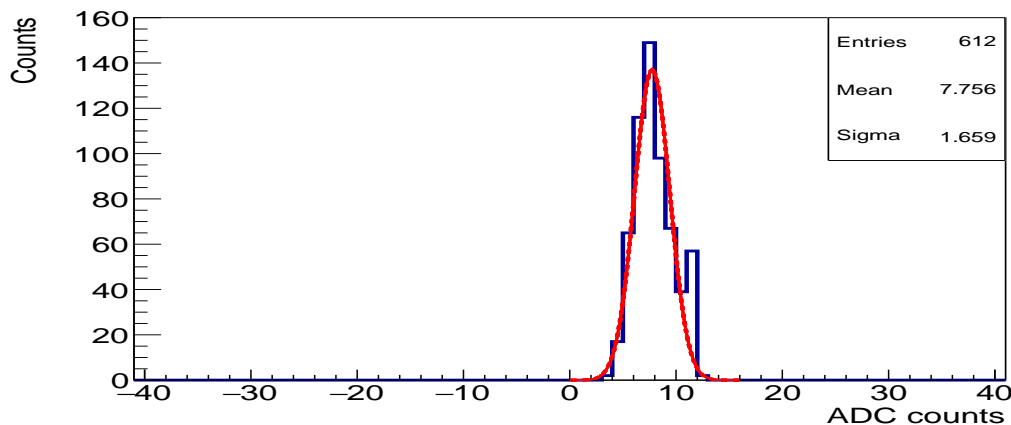
Figure 4.13: The sigma distribution determined from the Gaussian fit in **red** to the baseline part in one strip.

4.2.4 Influence of the sigma cut

Before using the sigma cut in the performance analysis of the GEM-TPC its influence on the measured positions, charge, and cluster strip multiplicity was investigated. Figures 4.14a and 4.14b show measured positions with the increasing values of the sigma cut. It can be seen that there are no major differences in the measured positions. In these plots, the error bars represent the width of the position distributions.

Next, the influence of the sigma cut on the measured charge is shown in Fig. 4.15a. Similarly, in this figure, the error bars represent the width, i.e. the sigma of the distribution. As expected, the measured charge decreased as the amplitude of the strips is cut.
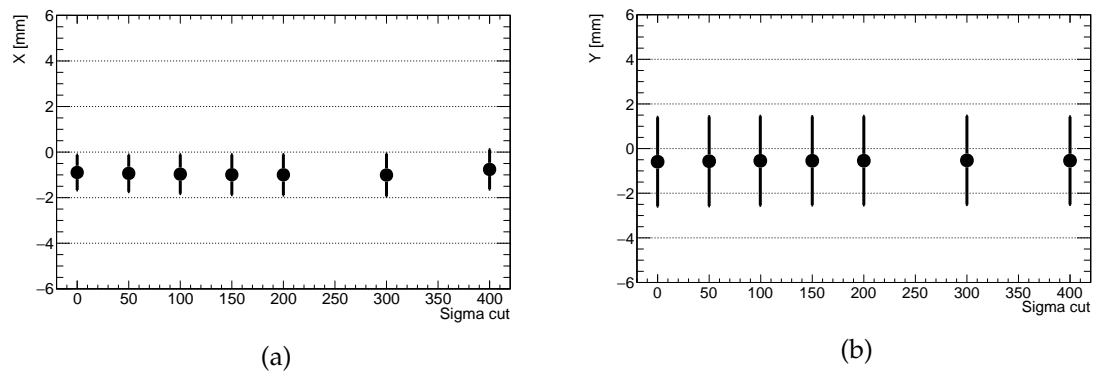
Figure 4.14: (a) Measured x position at the GEM-TPC with different sigma cuts. (b) Measured y position at the GEM-TPC with different sigma cuts.

The effect of the sigma cut on the cluster strip multiplicity is shown in Fig. 4.15b. As the cut value increased, the cluster strip multiplicity decreased. Additionally, an important observation from this plot is that the width of the distribution decreased up to a sigma cut ~ 100, indicating that the noise is eliminated at that point. Moreover, the cluster strip multiplicity value of the GEM-TPC, which is simulated earlier, is reached [99].

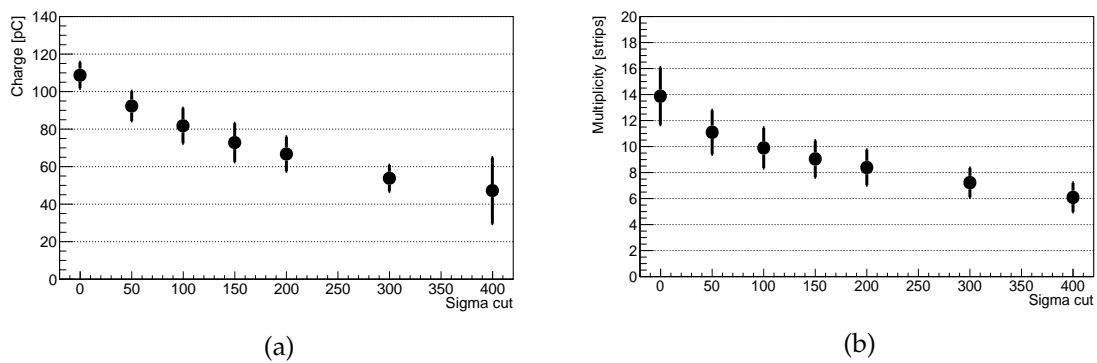**Figure 4.15:** (a) Measured charge at the GEM-TPC with different sigma cuts. (b) Cluster strip multiplicity at the GEM-TPC with different sigma cuts.

In summary, after studying the influence of the sigma cut, the value of 150 was chosen. This choice was made since it does not affect the measured positions at the GEM-TPC, the cluster strip multiplicity matches the simulated one, and the measured charge is not remarkably cut.

4.3 Calibrations

To calibrate the y coordinate of the GEM-TPC, the method described in Section 2.3.3 is used. The constants of 5.2(5) $\frac{cm}{\mu s}$ for the drift velocity v, and $y_{offset} = 5.01(4)$ cm are determined. The measured drift velocity corresponds well with the calculated value of 5.4(10) $\frac{cm}{\mu s}$, which was calculated based on a drift field of 122.5 V/cm.

For the TPCs, the standard calibration method is applied to the TPC42. However, due to the corrupted calibration files of the TPC41, an alternative approach similar to the calibration method used for the GEM-TPC is employed. In this process, the hits triggered by the TPC42 calibration grid are projected onto TPC41, resulting in three distinct peaks in the position spectrum of TPC41 in the x and y directions with a spacing of 6 mm and 12 mm, respectively.

4.4 Alignments

After the detectors have been mounted at the FRS, the pre-alignment is done with a laser beam. In addition, an offline alignment in the beam coordinate system is needed.

Using the beam position $x = 0$ mm, the TPCs are aligned to the beam coordinate system utilizing the following procedure [100]. The angle of the event trajectory with respect to the beam axis is extracted first, which is possible from the measured positions at the TPCs. Next, the residual distribution, which is the difference between the extrapolated and measured event position at the GEM-TPC is determined. If the mean of the residual distribution differs from zero, then an offset is added to the measured position of the TPC. This iterative method is continued until the residual distribution remains at zero and the extracted angle is close to zero.

Fig. 4.16 shows the examples of the determined residual distribution during the alignment procedure. The best match with the offset of 2.5 mm for the TPC41 is found. It can also be seen that during the iterative process, the mean of the residual distribution varies close to 0 mm, but the sigma value remains almost the same. In addition, the measured angle in the xz plane along the alignment process varied from 4.8 mrad to 1.9 mrad.

After aligning the TPCs, Fig. 4.17 shows the measured positions at the TPCs, triggered from the calibration grid of TPC42, and in Fig. 4.18 in all beam positions in the x direction. The difference in measured beam positions between the TPCs varied from 2.2 mm to 4.5 mm, using the 2.5 mm offset for the TPC41 as the best outcome of the iterative process. This can be seen in Fig. 4.19, where the
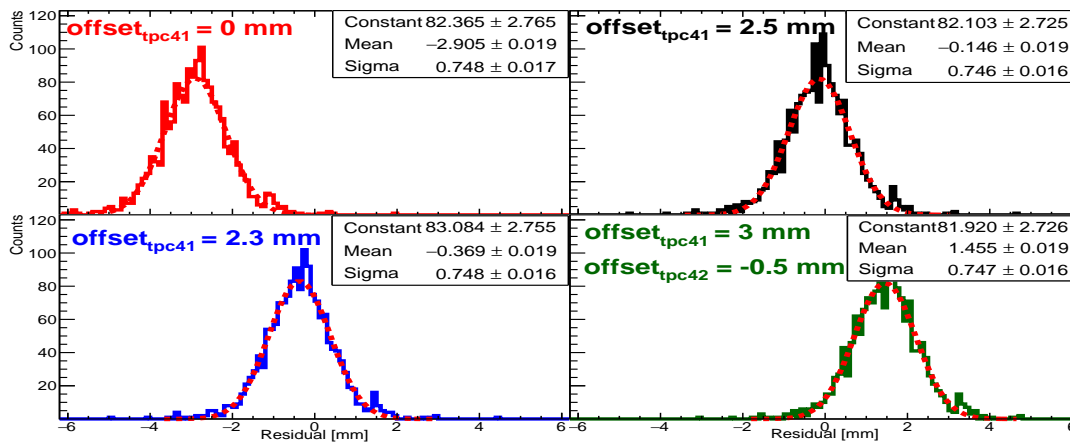
Figure 4.16: Measured residual distributions at the beam position $x = 0$ mm with different offset values in TPCs. The Gaussian fits are shown with **red** dashed lines. The figure is adapted from [1], under the license CC BY 4.0.
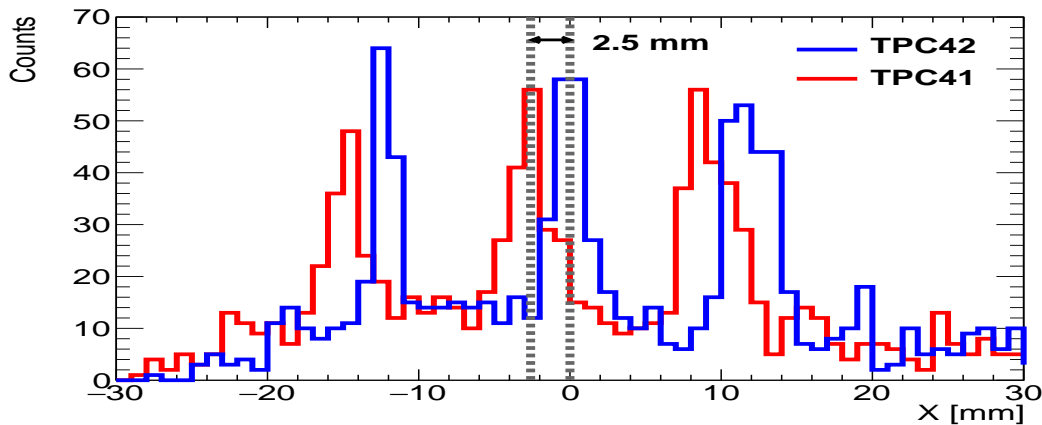
Figure 4.17: Measured positions at the TPCs after the alignments with the data measured with the trigger from the TPC42 calibration grid. The figure is adapted from [1], under the license CC BY 4.0. The colours of the original figure are changed.

correlation between the extrapolated and measured beam positions at the location of the GEM-TPC is shown. In this figure, the beam is on the 45° degree line and crosses the origin point at $x = 0$ mm, demonstrating the success of the alignment.
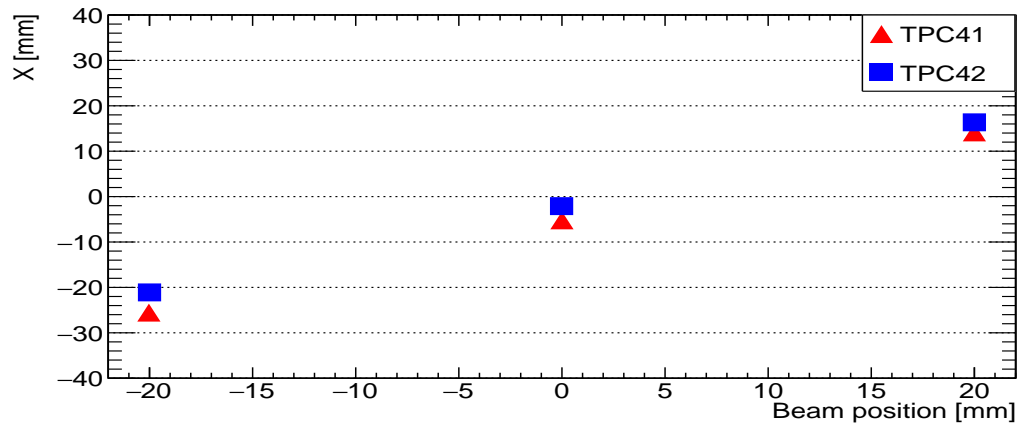
Figure 4.18: Measured positions at the TPCs after the alignment in different beam positions. The figure is adapted from [1], under the license CC BY 4.0. The colours of the original figure are changed.
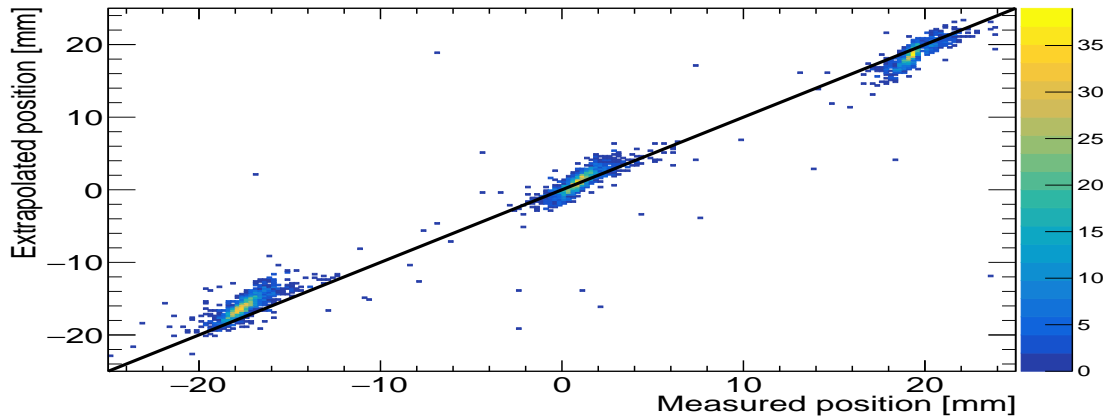
Figure 4.19: Extrapolated position of the GEM-TPC as a function of the measured x position in the GEM-TPC. The 45-degree line is shown in **black**. The figure is adapted from [1], under the license CC BY 4.0. The ranges of axes of the original figure are changed.

Although there is a generally good agreement between extrapolated and measured beam positions, slight differences are noticeable at the beam locations of -20 mm and +20 mm. This discrepancy is due to propagation errors from various sources, including the position calibration precision and the error associated with the extrapolated and measured positions. However, the cumulative error contribution remains relatively small. In summary, the overall impact of these discrepancies is minor.

4.5 Results

After the calibrations and alignments, the beam profiles are extracted at the beam position $x = 0$ mm, shown in Fig. 4.20. Since the focal point at the FRS was set behind the GEM-TPC, one can see the beam spot decreases horizontally.
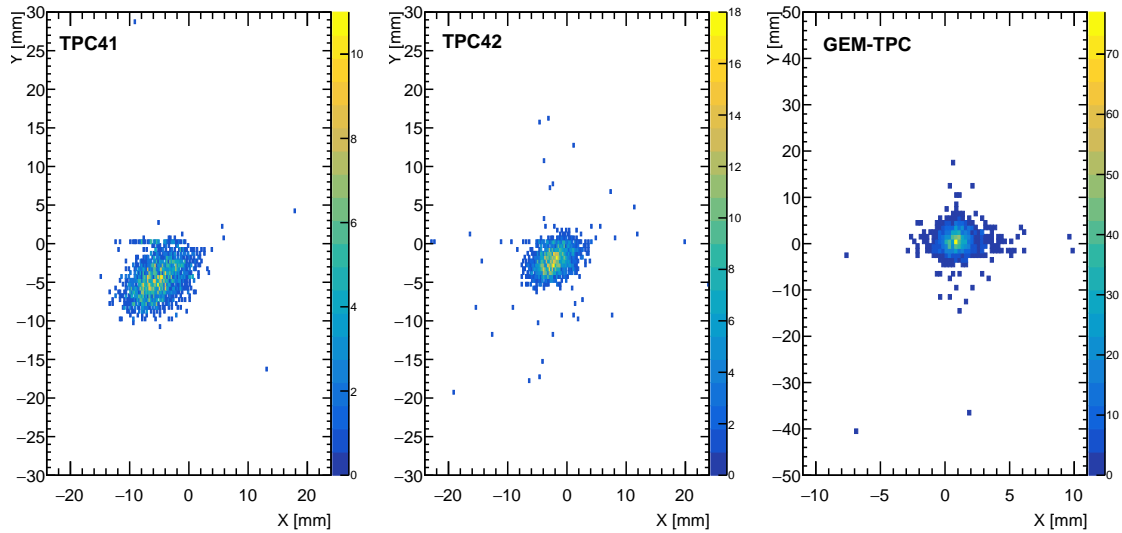
Figure 4.20: Extracted beam profiles at the TPCs and GEM-TPC, in the beam position $x = 0$ mm. The figure is adapted from [1], under the license CC BY 4.0.

4.5.1 Cluster Multiplicity and Cluster Strip multiplicity

Cluster multiplicity represents the number of clusters within one scintillator trigger.

Cluster strip multiplicity is defined as the number of strips fired within one cluster. In Fig. 4.21 measured cluster strip multiplicity is shown in different beam positions. It can be seen that it varies between 9 - 11, which is in agreement with a simulation [99] done earlier using Garfield++ program [101, 102].
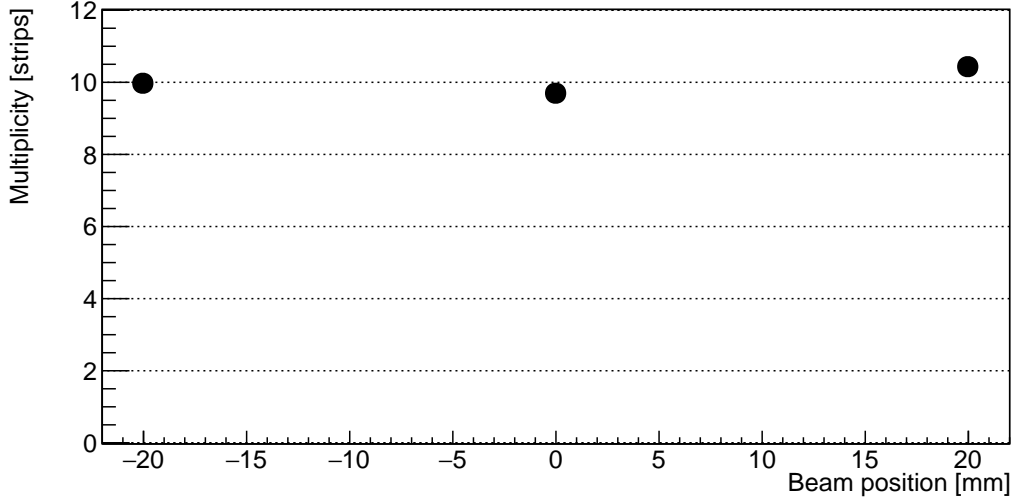
Figure 4.21: Determined cluster strip multiplicity in different beam positions.

4.5.2 Spatial resolution

The spatial resolution of the GEM-TPC is calculated using the residual distribution, which is filled with the differences between measured and extrapolated positions at the GEM-TPC. The linear extrapolation used to calculate the track position in the location of the GEM-TPC x_{ext} is

$$x_{ext} = \frac{x_{42} - x_{41}}{d_1} \cdot d_2 + x_{42}, \qquad (4.2)$$

where x_{42} and x_{41} are the measured track positions in the TPCs, and $d_1 = 1120$ mm and $d_2 = 1235$ mm are the distances between TPCs, and between TPC42 and GEM-TPC respectively. The quadratic sum of the spatial resolution of the GEM-TPC, $\sigma_{GEM-TPC}$, and tracking uncertainty $\sigma_{trackers}$ contains the width of the residual distribution $\sigma_{residual}$ [103], expressed as

$$\sigma_{residual} = \sqrt{\sigma_{GEM-TPC}^2 + \sigma_{trackers}^2}. \qquad (4.3)$$

In this analysis, an assumption was made that the tracking uncertainty includes only the intrinsic spatial resolutions of the TPCs. However, this assumption leads to an underestimation of the tracking system's uncertainty, resulting in a decreasing GEM-TPC spatial resolution. The method described in Ref. [31] was used to determine the intrinsic spatial resolutions of the TPCs. In this method, the deviation of the measured positions Δx, is determined as follows

$$\Delta x = x_1 - x_2, \qquad (4.4)$$

where x_1 and x_2 are the measured positions in the first and second delay line. Then the intrinsic spatial resolution σ_x can be calculated from the width of the deviation distribution

$$\sigma_x = \frac{\sigma_{\Delta x}}{\sqrt{2}}. \tag{4.5}$$

In the beam position $x = 0$ mm, the determined intrinsic spatial resolutions of the TPCs are 81(2) μm and 75(2) μm for the TPC41 and TPC42. One example of the residual distribution with a width of 0.75(2) mm and a mean of -0.15(2) mm at the beam position $x = 0$ mm, is shown in Fig. 4.22. In this position, the extracted spatial resolution of the GEM-TPC is 0.74(2) mm. In Table 4.1 the spatial resolutions at all beam positions are shown. It can be seen that the spatial resolution varies from 0.74(2) mm to 0.81(2) mm but remains < 1 mm at all beam positions, which means that the GEM-TPC fulfills one of the design goals of the Super-FRS. Moreover, the determined spatial resolutions are remarkably different compared to the earlier measurement of 300 μm [32]. The latter measurements were done with the GEM-TPC prototype HB3 using a different electronics, different measurement setup, and the external spatial resolution of the TPCs was used to extract spatial resolution of the GEM-TPC.
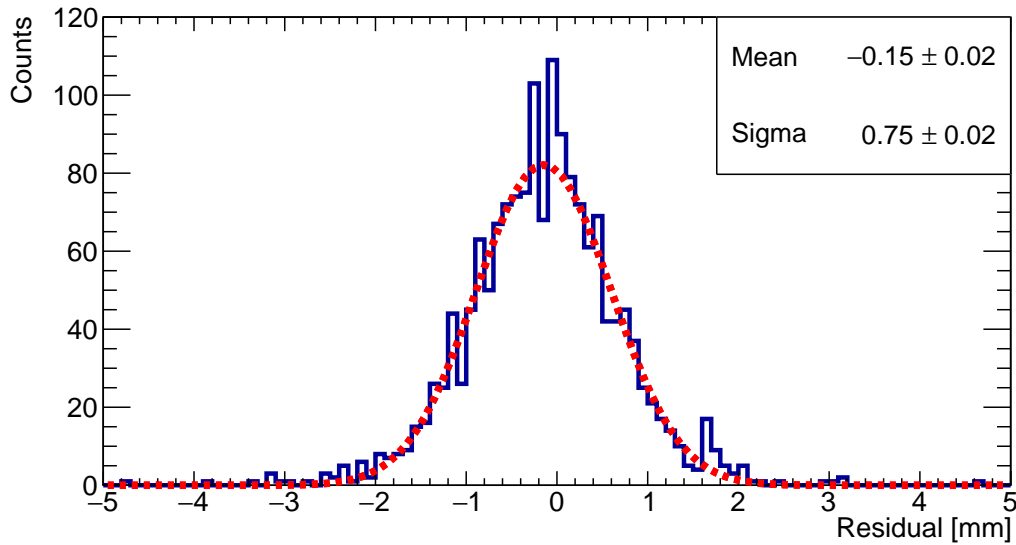
Figure 4.22: The residual distribution example for spatial resolution determination with the Gaussian fit in **red**, at the beam position $x = 0$ mm. The extracted spatial resolution in this beam position is of 0.74(2) mm. The figure is adapted from [1], under the license CC BY 4.0. The x axis of the original figure is scaled, and number of entries is removed.

Table 4.1: Measured spatial resolutions of the GEM-TPC in different beam positions.

Beam position	-20 mm	0 mm	+20 mm
Spatial resolution [mm]	0.81(2)	0.74(2)	0.77(3)

4.5.3 Tracking and Detection efficiency

Tracking and detection efficiencies are studied using the scintillator SC41 as the trigger. For the tracking efficiency determination, the TPCs are used as reference trackers. The tracking efficiency determines the ratio of reconstructed clusters, with a position within 5σ of the extrapolated position extracted using the TPCs, in the GEM-TPC and events in the TPCs. The spatial resolution of the GEM-TPC is used to determine the value of the sigma. Additionally, the detection efficiency of the GEM-TPC is defined as the ratio of events with a reconstructed cluster and the number of triggered events at the scintillator.

The measured tracking and detection efficiencies in all beam positions are shown in Table 4.2. It can be seen that in all positions, the detection efficiency is close to 100 %, and the tracking efficiency >96 % is measured.

Table 4.2: Measured detection and tracking efficiencies of the GEM-TPC.

Beam position	-20 mm	0 mm	+20 mm
Detection efficiency [%]	100.0	99.9	100
Tracking efficiency [%]	96.0	99.0	97.5

4.5.4 Effect of Merging Strips

To study the effect of merging strips e.g. summing up the strip signals of two, three, and four strips was studied to determine changes in the position, spatial resolution, detection efficiency, tracking efficiency, and cluster strip multiplicity. This analysis aims to determine if the number of strips can be reduced while maintaining the required spatial resolution. Hence, support the design of Super-FRS GEM-TPC. An example of the reconstructed cluster with all studied combinations is shown in Fig. 4.23. The mean value (μ_1) of the original cluster is 95.8(2) strips. When two strip signals are summed, the mean value (μ_2) of 47.3(2) strips is determined. Summing three and four strips, the mean values (μ_3 and μ_4) of 31.2(1) and 23.1(1) are obtained, respectively.
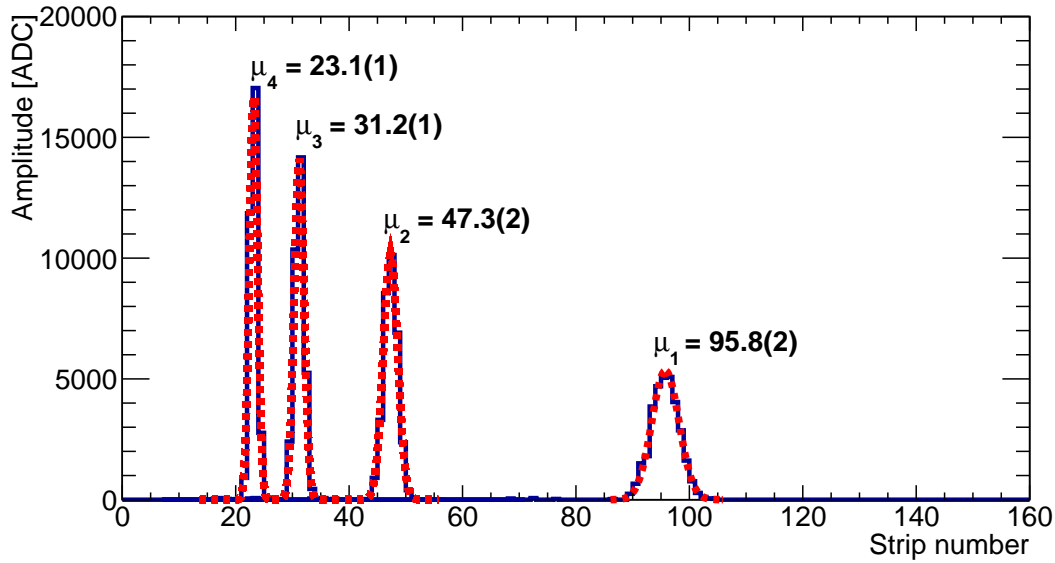
Figure 4.23: The example of clusters where two, three, and four strip signals are merged, additionally the Gaussian fits are shown with a **red** dashed lines. The mean value of the reconstructed cluster changes from strip 95.8(2) to strip 23.1(1).

Table 4.3 shows the effect of merging strips in all studied variables. The maximum difference in the measured spatial resolution deviates by only 9 %, and cluster strip multiplicity decreases as expected. The measured detection efficiency remains the same, and the tracking efficiency is >98% in all cases.

Table 4.3: Effect of the strip merging on the measured position, spatial resolution, and cluster strip multiplicity of the GEM-TPC.

Variable under study	Merged strips			
	0	2	3	4
Measured position [strip]	95.8(2)	47.3(2)	31.2(1)	23.1(1)
Spatial resolution [mm]	0.74(2)	0.81(2)	0.77(2)	0.73(2)
Cluster strip multiplicity [strips]	12.6	7.4	6.3	5.4
Detection efficiency [%]	99.9	100.0	100.0	100.0
Tracking efficiency [%]	99.0	98.2	98.2	98.0

In conclusion, big deviations are not found in the variables under the study.

4.5.5 Effect of the data Digitization

In Ref. [2], the development of a new clusterization method for the GEM-TPC detector, the effect of the data digitization into the measured position, spatial resolution, and cluster strip multiplicity was studied. It was found that by reducing the data digitization from 13 bits up to 4 bits the position reconstruction in the x and y directions did not drastically change. Moreover, the determined spatial

resolution remains almost the same, and only the amplitude of the reconstructed cluster and cluster strip multiplicity decrease as expected.

An example of the reconstructed clusters with different data digitization is shown in Fig. 4.24.
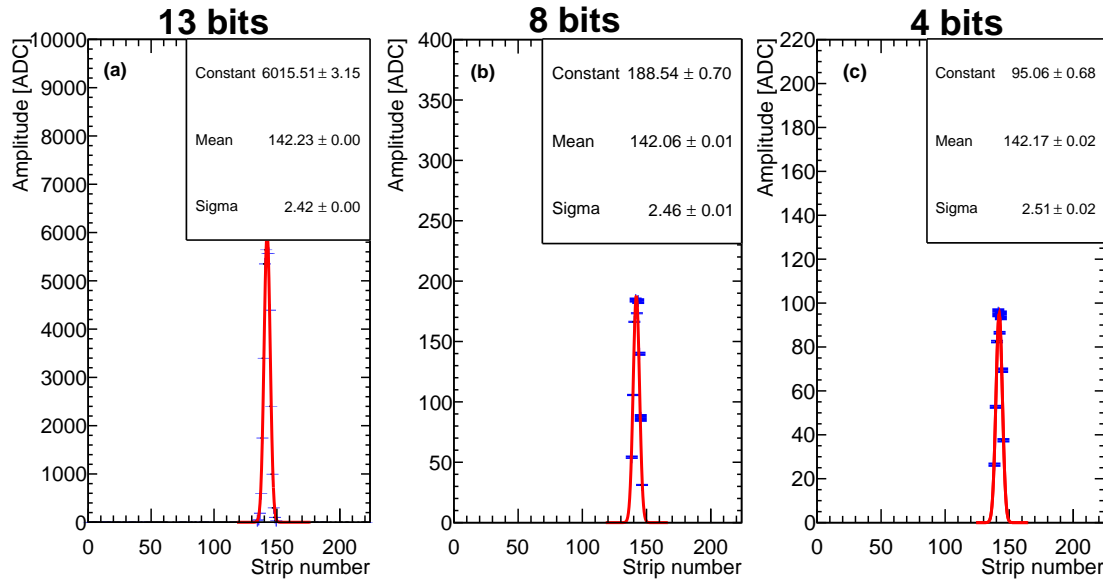
Figure 4.24: Reconstructed clusters with (a) 13 bits, (b) 8 bits and (c) 4 bits. The dashed **red** line represent the Gaussian fit. The figure is adapted from [2], under the license CC BY 4.0. The number of entries and mean values are removed from the original figure, and the accuracy shown for the statistical values is changed.

Figure 4.25 shows the measured cluster strip multiplicities with varying data digitization. As the data digitization decreases, there is a reduction in the number of strips fired within a single cluster.
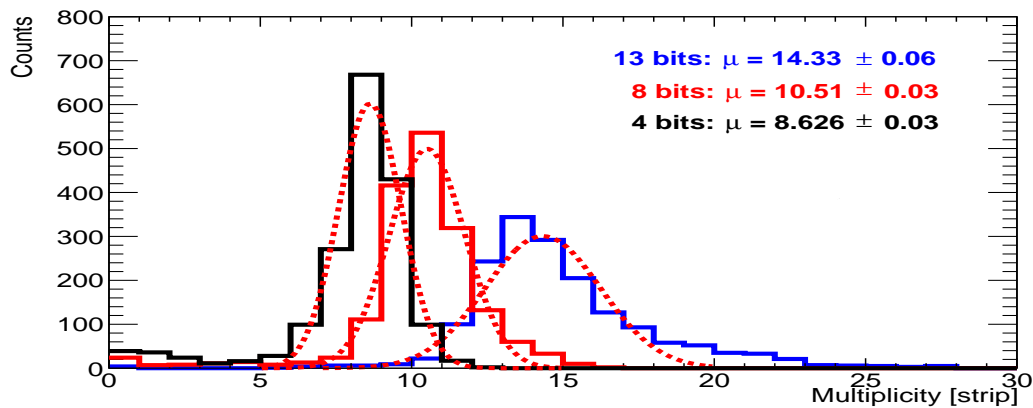
Figure 4.25: Determined cluster strip multiplicity with different digitizations in the data. The Gaussian fits are shown with a **red** dashed line. The figure is adapted from [2], under the license CC BY 4.0. The ticks are added to the x and y axes of the original figure.

After investigating how reduced data digitization affects clusters, the next parameter studied was the position. The beam profiles determined in the GEM-TPC with different digitizations are shown in Fig. 4.26. Although some differences were observed, they were not significant.
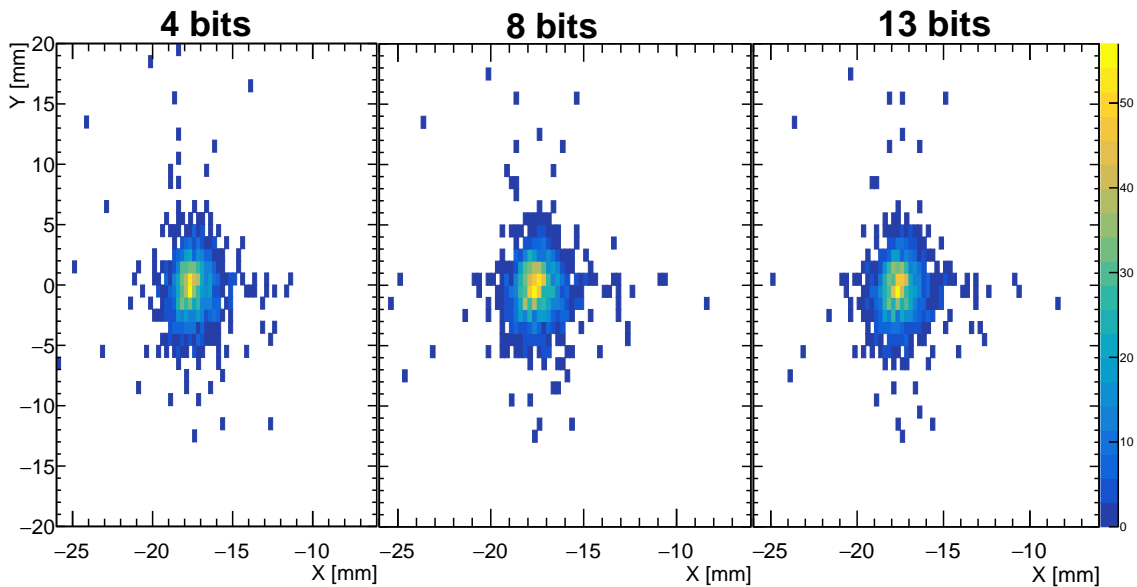
Figure 4.26: Reconstructed beam profiles with different digitizations in the data. The figure is adapted from [2], under the license CC BY 4.0. The order of sub figures in the original figure is changed, and the colour palette is added to the original figure.

In the Table 4.4 the measured spatial resolutions are shown with studied digitizations. It can be observed that there is no remarkable change if the digitization is reduced from 13 bits to 4 bits.

Table 4.4: Measured spatial resolutions with different data digitization.

Digitization [bit]	13	8	4
Spatial resolution [mm]	0.80(2)	0.81(2)	0.82(2)

5 EXPERIMENT FOR MEASURING NEW β-DECAY HALF-LIVES

The NUclear STructure, Astrophysics, and Reactions (NUSTAR) collaboration is one of the four pillars of the FAIR [104, 105]. One of its research interests is to study the production and properties of new exotic proton-rich and neutron-rich nuclei, as well as to explore the limits of nuclear stability [106].

This chapter contributes to the analysis of the *S468* experiment, "Search for new neutron-rich isotopes and exploratory studies in the element range from terbium to rhenium". The *S468* experiment aimed to identify new neutron-rich isotopes, measure their production cross-sections, their masses, and β-decay half-lives.

A primary beam of $^{208}\text{Pb}^{67+}$ with an energy of 1.05 GeV/u and an intensity of $1.5 \cdot 10^9$ ions/spill was used to carry out the experiment. The beam bombarded a beryllium target with the thickness of 4 $\frac{\text{g}}{\text{cm}^2}$, backed by a niobium stripper with the thickness of 223 $\frac{\text{mg}}{\text{cm}^2}$. The resulting fragmentation reaction produced new exotic neutron-rich nuclei within the isotope range from erbium to rhenium. The inclusion of the niobium backing was to achieve the full ionization of 95 % of all fragments [67]. The experimental setup and the identification method employed in the *S468* experiment are described in Chapter 2.

During the *S468* experiment, when the β-decay half-lives were measured, the FRS was tuned to three different settings ^{193}W, ^{193}Ta, and ^{190}Lu. Although the data of this experiment include comprehensive information on the neutron-rich nuclei, this thesis focuses on the new β-decay half-life analysis. The analysis of the identification of the new isotopes can be found in the PhD work of J-P. Hucka [67].

5.1 Analysis technique to measure the half-life of the β-decay

One of the most widely used techniques for measuring the half-lives of the nuclei is to measure the emission of decay radiation from a sample over time and utilize an exponential fit. This fit provides the decay constant λ, which can then be used to calculate the half-life. The successful usage of this technique requires a sufficient number of decaying nuclei and a measuring time long enough to obtain a reasonable number of data points during the decay process. In addition, if the sample contains activities from other nuclei, their time dependence must be taken into account when applying the exponential fit.

Another method in order to measure half-lives is the so-called delayed-coincidence method. In this method, the nuclei of interest are implanted into a catcher, or for example into a moving tape surrounded or followed by tracking detectors. After that, the β-decay half-lives are determined by the time difference between implanted nuclei and subsequent β-decay. In the present work, the resulting time-difference distribution is influenced by the decay constant λ of the implanted nuclei, the detection efficiency, and the decay half-life of the daughter nucleus and background radiation. False correlations with particles not associated with the nuclei under study represent the background of this method. Figure 5.1 shows the schematic figure of the false correlations in the present work where the delayed-coincidence method is used to measure β-decay half-lives.
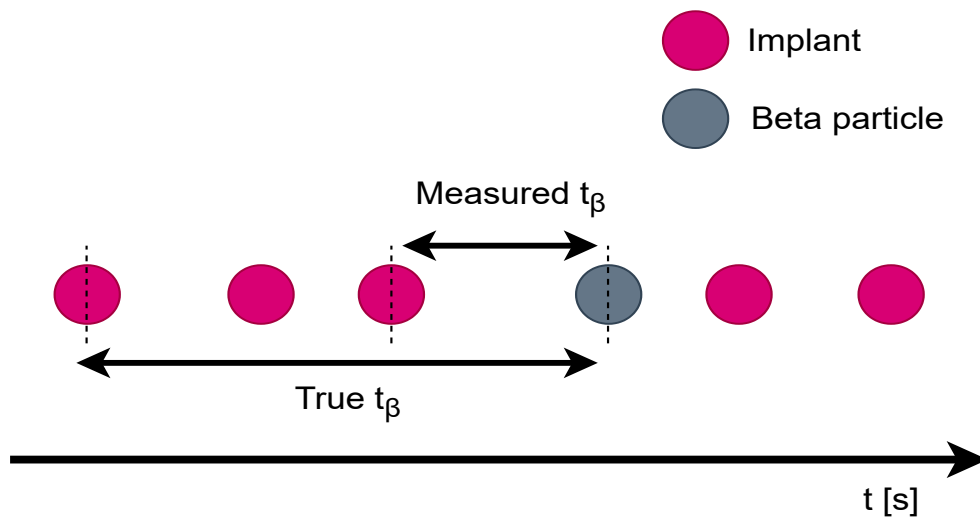
Figure 5.1: Schematic illustration showing the false implant-beta-particle correlation.

The analysis technique used in this work to measure β-decay half-lives was originally presented by T. Kurtukian *et al.* [107]. It includes a χ^2 fitting procedure that compares the experimental data with results from a numerical model derived from Monte-Carlo simulations of fragment-β-decay time correlations. To obtain the shape of the background distribution, a new spectrum is determined by reversing the time of fragment-β-decay correlations. The ratio of the forward-to-backward

time spectra provides the actual information about the β-decay curve. This method is successfully implemented to determine new β-decay half-lives, for example, in two PhD works [108, 109].

In addition, another method has been tested and utilized in this work to determine the background shape of the fragment-β-decay correlations. This alternative method includes shifting the implantations forward in time (at least two half-lives) and determining the "background" correlations between fragment-β decay in the forward direction. After that, the ratio between the actual and background correlations is computed and compared with the results obtained from the numerical model.

5.2 Experimental setup in the β-decay half-life measurement

First of all, the accurate identification of the implanted fragment is essential for measuring β-decay half-lives since various fragments that are delivered to the focal plane *F4* by the FRS decay via β decays, making it difficult to distinguish between them. The analysis focuses on selecting the fragments that stopped in the double-sided silicon strip detector (DSSD), active stopper [110], and measuring their subsequent β decays. The experimental setup at *F4* is shown in Fig. 5.2.
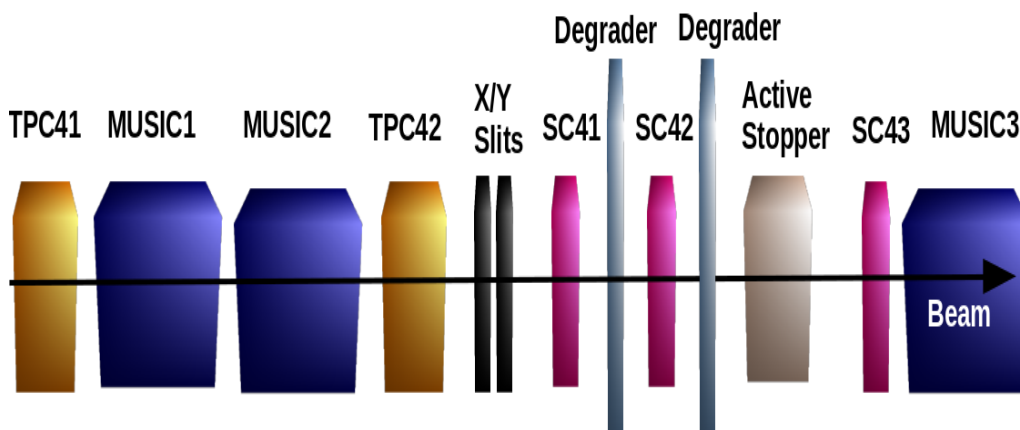
Figure 5.2: Showing the setup used at the *F4* for the measurements of β-decay events.

The fully stripped fragments are selected using the MUSIC1 and MUSIC2 detectors. The TPC detectors provide the position measurement of the fragments while SC41 and SC42 are used for triggering and time-of-flight measurements. The SC43 and MUSIC3 detectors are positioned downstream of the active stopper and used as veto detectors for accurate implantation detection. Degraders are also utilized to slow down the fragments, enabling their implantation into the active stopper.

5.3 The active stopper for the implant and β-particle detection

The active stopper was used to stop the fragments, measure their position, and detect the position of subsequent β decays. Additionally, the deposited energies of the fragments and β particles were measured. The active stopper includes six DSSDs [110]. Each detector consists of 16 strips in both x and y directions with the thickness of 1 mm and strip width of 3 mm. The configuration that was utilized consisted of two layers of three adjacent detectors (see Fig. 5.3).
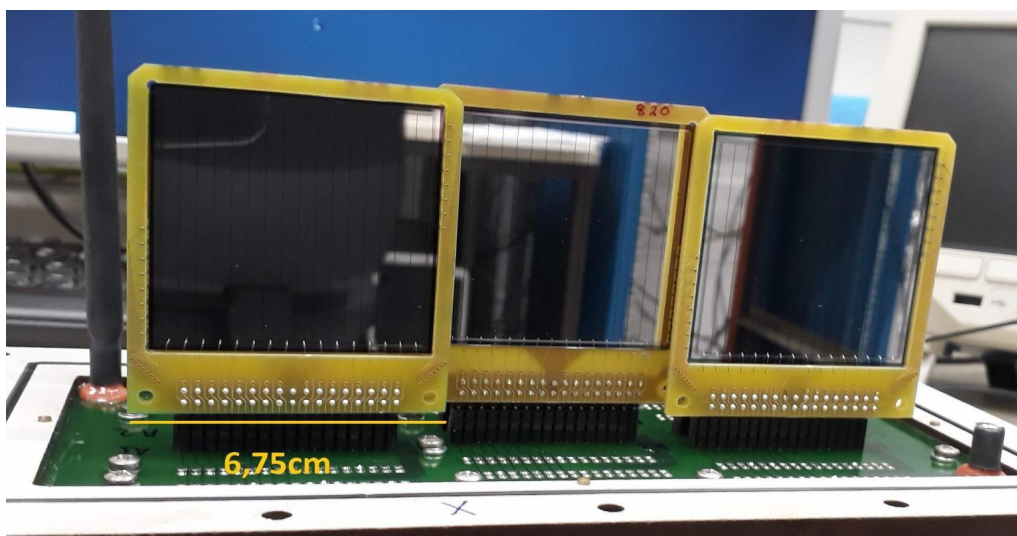
Figure 5.3: Picture showing one layer of the active stopper.

Although the active stopper is capable of measuring the position, energy, and time of both the fragment and the subsequent β decay, the problem arises from the significant difference in energy deposition between these two particles. The fragment can deposit energy at a GeV level, whereas the β particle deposits energy in the MeV range. To handle this issue, a linear-logarithmic pre-amplifier MPR-32 [111] was used. It provides 32 input channels for the 16 x and y strips, with a linear response of 0-10 MeV and a logarithmic response up to 3 GeV beyond that.

A process called "gain match" was performed to achieve the logarithmic range of the pre-amplifier. The gain match includes fitting the corresponding channel of the measured implantation energy with the Gaussian function and aligning it with all strips in the x and y directions. The purpose of the gain match is not to determine the absolute value of the deposited energy of the fragments but to enable gating on implantation energies.

A ^{207}Bi source emitting monoenergetic conversion electrons was utilized to calibrate the linear range of the pre-amplifier. Gaussian functions were fitted to the measured peaks in each strip, and a linear fit was performed to determine the calibration variables.
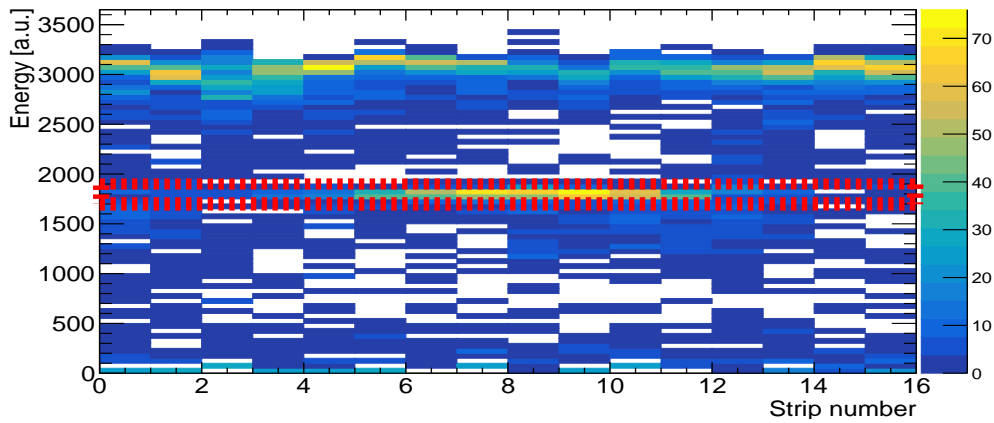
Figure 5.4: Measured energies of ^{199}Os implantation in the x direction at the active stopper. The energy gate used for the implants is drawn with a **red** dashed line.

Additionally, the degrader at *F4* was used to slow down the fragments. Nevertheless, the energies at the active stopper are partly in the saturation in the x direction strips, as shown in an example of the measured implantation energies of the ^{199}Os isotope in Fig. 5.4. In contrast, the measured energies in the y direction are shown in Fig. 5.5. In order to gate on the implantations on the x side, an energy gate around 1800 is chosen for the implants (see Fig. 5.4). The energy gate selected provided a good agreement with the identification of the fragment and its position (see chapter 5.4).
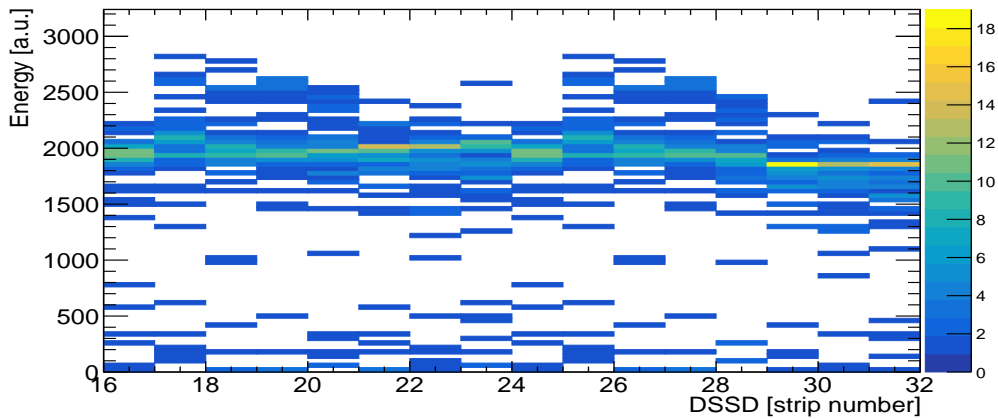
Figure 5.5: Measured energies of ^{199}Os implantation in the y direction at the active stopper.

5.3.1 FRS DAQ system: Trigger for β-decay and implant-like events

In the present experiment, the standard FRS data acquisition system based on the VME electronics was used [93]. The system consisted of four MBS branches, each comprising a VME crate controlled by a RIO3 or RIO4 processor and a TRIVA trigger module [112]. Two processors are used in order to increase the data recording rate. The data collected by the processors was then transmitted to the front-end computer, which handled event formatting and data storage.

In addition, for this particular experiment, two distinct triggers were defined with the aim of identifying either implantation events or decay-like events:

- The first trigger was designed to save data from the detectors while checking for the implantation of nuclei in the active stopper. This trigger was activated when a high-energy signal (CFD threshold of -150 mV) was detected in SC42 left. All data from the FRS detectors and active stopper were saved in this mode.
- The second trigger was intended for measuring decay-like events. It required detecting a low-energy signal (CFD threshold of -2 mV) in SC42 right and a low-energy signal in SC43. When this combination of signals was detected, data from the active stopper and all detectors of the FRS were saved.

By utilizing these trigger configurations, it was possible selectively record data corresponding to the specific events of interest during the experiment.

5.4 Identification of implants

The $B\rho - ToF - \Delta E$ method described in Section 2.2.1 was used to identify the implants. However, many abrasion-fission products were detected together with the fragments, as shown in the identification plot of the ^{193}Ta setting in Fig. 5.6. Hence, only implants with $Z > 70$ that stopped in the active stopper are considered for the β-decay analysis. The scintillator detector SC43 and MUSIC3 detector downstream are used for implantation veto. Additionally, the calculated position of the fragments using the TPCs, denoted as the extrapolated position, was used as a criterion for the implantation veto.
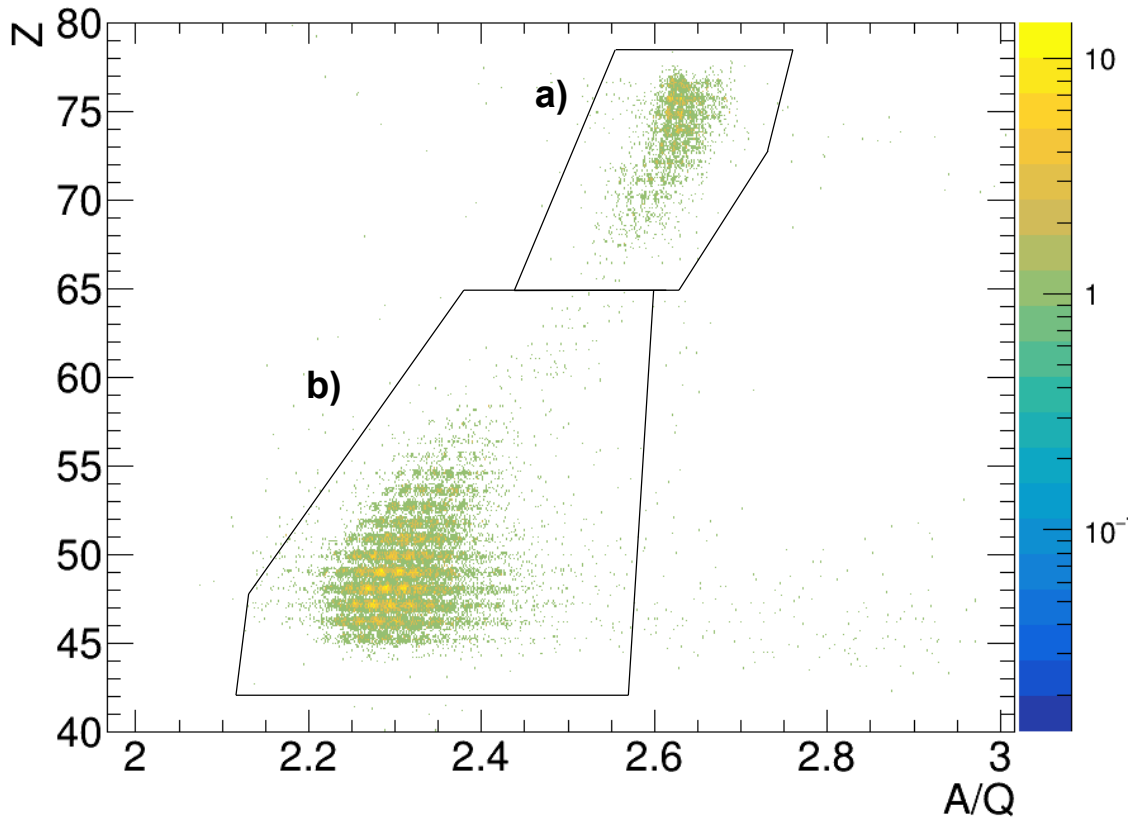
Figure 5.6: The identification plot of the ^{193}Ta setting without any selection or clean-up. In area a) the projectile fragmentation events are shown, while area b) represents the abrasion-fission products.

Figure 5.7 shows the proton number Z versus the mass-over-charge of the fragments at the focal plane *F4* using the ^{190}Lu setting after applying fragment identification and a gate on the selected region for the proton number. This plot enables the identification and gating of different isotopes for the implantation analysis. As a note, some new isotopes are observed with the ^{190}Lu setting, which are not present in the NUDAT database [113].
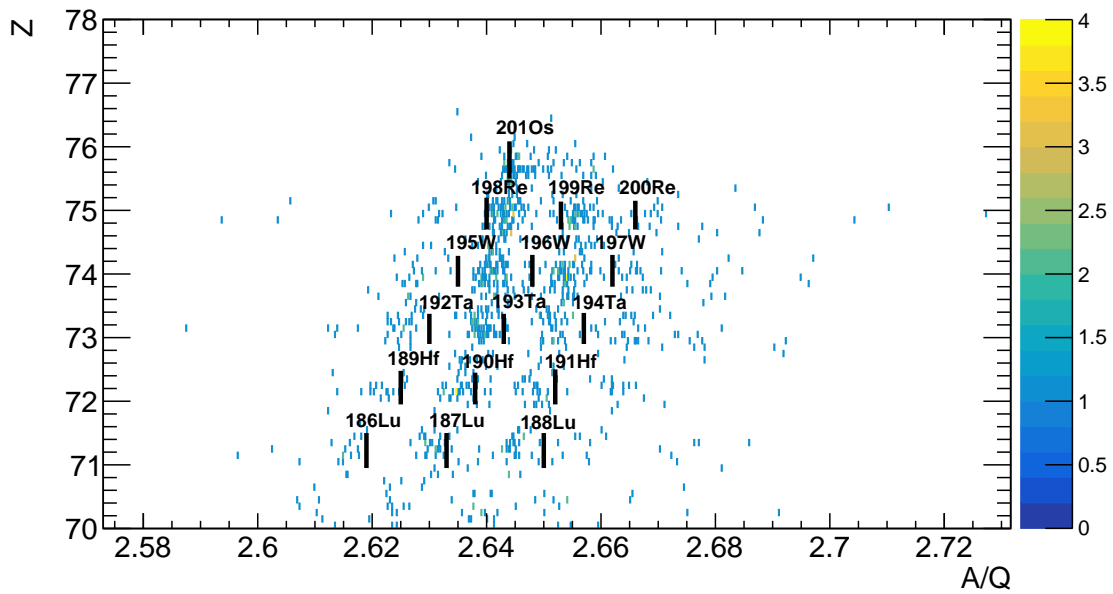
Figure 5.7: Identification of fragments at the *F4* using the ^{190}Lu settings. Vertical lines represent the calculated mass-over-charge ratio of each fully stripped isotope.

Moving forward with the implant identification, a correlation plot between the extrapolated positions by TPCs and the measured positions of the fragments at the active stopper location is shown in Fig. 5.8. Additionally, Fig. 5.9 compares the measured implant positions with the predicted positions generated by LISE++ [71,72]. Both figures show good agreement between the predicted and measured positions. However, in order to match the predicted width of about 13 mm at the active stopper for fragment positions determined with LISE++, a gate was applied to the extrapolated positions extracted with the TPCs.
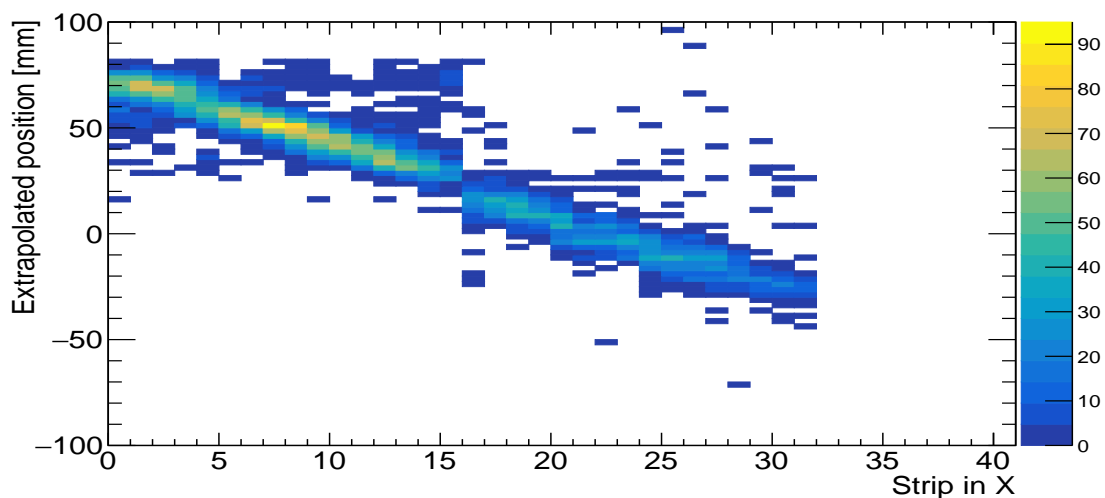
Figure 5.8: The position correlation of the fragments between the extrapolated position by TPCs and measured position in the active stopper in ^{193}Ta setting.
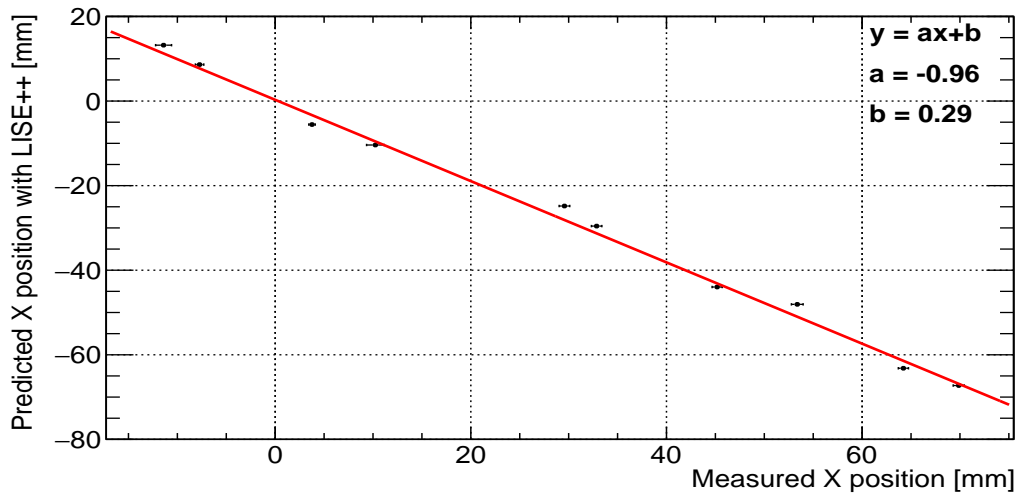
Figure 5.9: Comparison of predicted position by LISE++ and the measured position of the fragments in ^{193}Ta setting. The linear fit is shown with a **red** line.

To determine the position gate, a linear fit was performed on Fig. 5.8. The gate was set up to accept fragment positions within ± 3 strips of the fit, corresponding to a range of 18 mm. The correlation plot with the position gate is shown in Fig. 5.10.
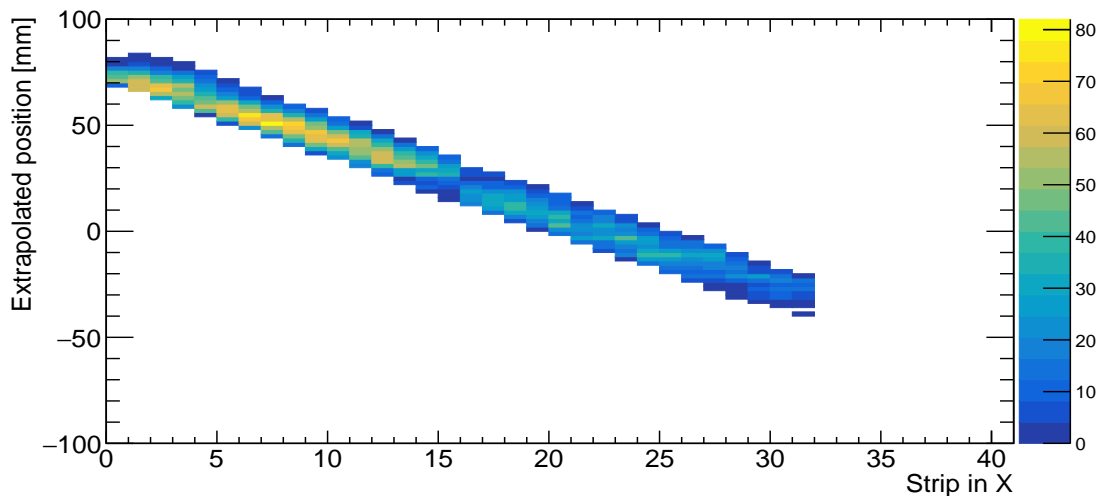
Figure 5.10: Position correlation within the position gate between the extrapolated position by TPCs and the measured position of the fragments in the active stopper in ^{193}Ta setting.

Finally, through the process of selecting the implanted isotopes and utilizing implantation veto conditions and gates, a cleaner proton number Z versus mass-over-charge plot was achieved for the implanted fragments, as shown in Fig. 5.11 with the ^{193}Ta setting. Moreover, Fig. 5.12 presents a schematic figure of the corresponding part of the nuclei chart. This figure presents stable isotopes in grey boxes while the implanted isotopes are highlighted in red. Additionally, the projectile nucleus ^{208}Pb is shown in the top right corner.
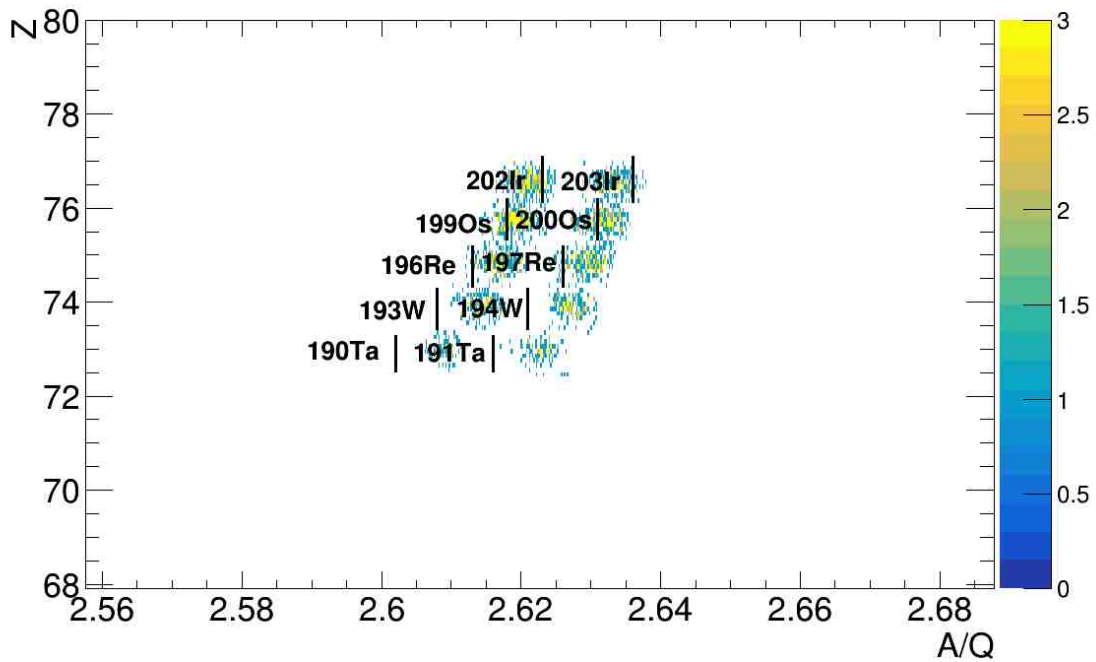
Figure 5.11: Identification of implants at the active stopper using the ^{193}Ta setting.
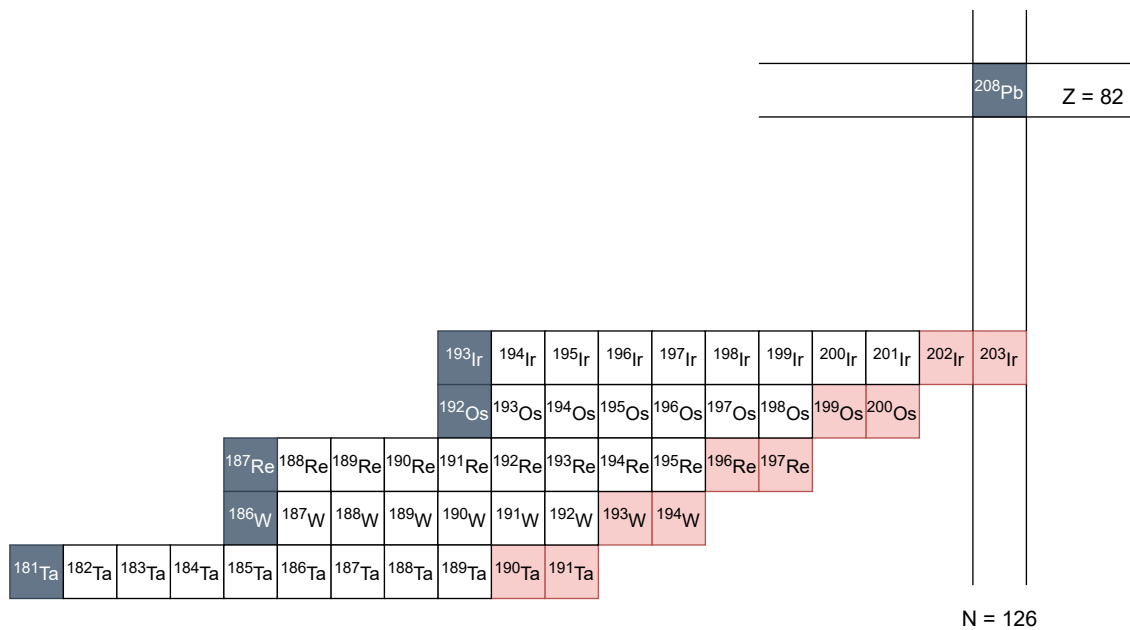
Figure 5.12: The schematic figure of the corresponding section of the nuclei chart with the ^{193}Ta setting. **Red** squares show the isotopes implanted in the active stopper, and grey boxes represent the stable isotopes.

5.4.1 Corrections to the identification in the S468 experiment

After calibrating the trackers as described in Chapter 2, the identification plot i.e., measured Z as a function of the A/Q, did not show the expected grid-structure. Instead, a visible bend was observed (for detailed information, see J-P. Hucka's PhD thesis in Ref. [67]). This tilt can be attributed to the plastic scintillators,

which showed asymmetric output when collecting light over the active area due to ageing and radiation damage. This asymmetry results in a difference between the expected *ToF* value and the measured one.

To anchor and assign fragments in the identification plot, a good agreement was determined with a mass-tagging measurement from the FRS Ion Catcher [114], which was complemented with simulations from LISE++ [71] and MOCADI [115] (see details in J-P. Hucka's PhD thesis in Ref. [67]).

5.5   Selection of β-decay events

In the present work, accurate identification of β-decay events was challenging due to the presence of high β-particle background and abrasion-fission background events (see Fig. 5.6). Therefore, multiple detectors were employed for veto purposes to reduce the risk of false correlations in addition to the β-decay trigger. This included the utilization of scintillators such as *SC41*, *SC42*, *SC43*, as well as the MUSIC detectors *MUSIC1*, *MUSIC2*, and *MUSIC3*.

5.6   Fragment-β-decay correlations

After completing the identification process of the implanted fragments and β decays, the next step was to determine fragment-β-decay time correlations on the event-by-event basis. This measurement was required in order to apply the delayed-coincidence method as explained in Section 5.1. For this analysis, it was necessary to have access to both the position and time information of the fragment-β-decay correlation.

5.6.1 Position correlation

The high energies of the implanted particles lead to observed cross-talk effects in the active stopper. The cross-talk can be seen in the measured strip multiplicity of ^{199}Os with the ^{193}Ta setting in Fig. 5.13, where mainly the strip multiplicity of three was measured for this isotope in the x direction. Moreover, the cross-talk effect was also observed in the y direction of the active stopper, as shown in Fig. 5.14.
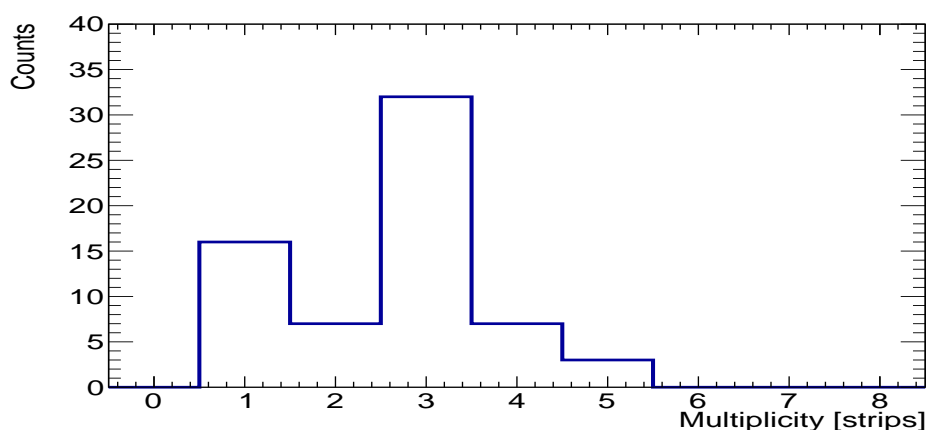
Figure 5.13: Strip multiplicity in the x direction at the active stopper of ^{199}Os implantation.
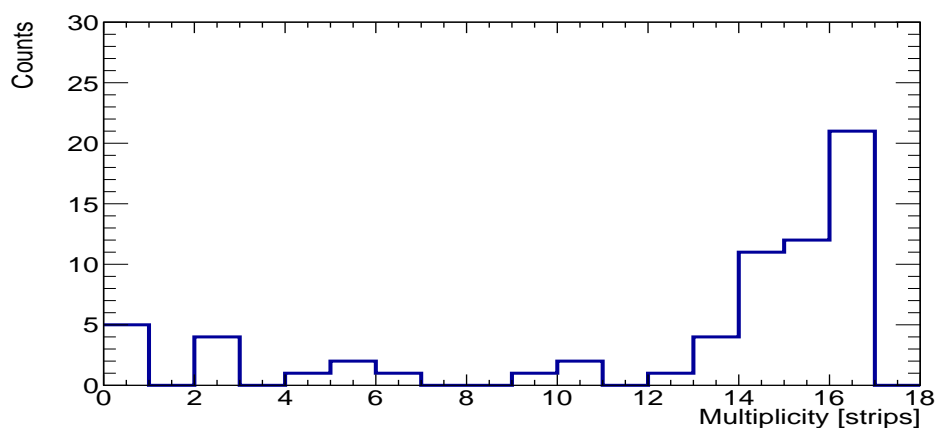
Figure 5.14: Strip multiplicity in the y direction at the active stopper of ^{199}Os implantation.

Considering the cross-talk effect observed in the y strips of the active stopper, the determination of the implantation position and β-particle position relied only on the x strips, since the pixel analysis was not possible. Furthermore, the correlation was required in the fired strips within the energy gate applied for the implantation energy.

5.6.2 Time correlation

The measured beam intensities with the SEETRAM detector as a function of time with all settings are shown in Figs. 5.15a, 5.15b, and 5.15c, and the beam cycles for all settings can be found in Table 5.1. It is important to note that despite the beam cycle shown in Fig. 5.15b, the experiment was done in the so-called "parasitic"-mode, which means that a part of the spills was not delivered to the $F4$, resulting in longer gaps of 7.2 s between spills. The longer gaps can be observed in Fig. 5.15a with ^{193}W setting, in Fig. 5.15c with the ^{190}Lu setting, and in Fig. 5.16, which shows the time intervals between the spills in ^{193}Ta setting.
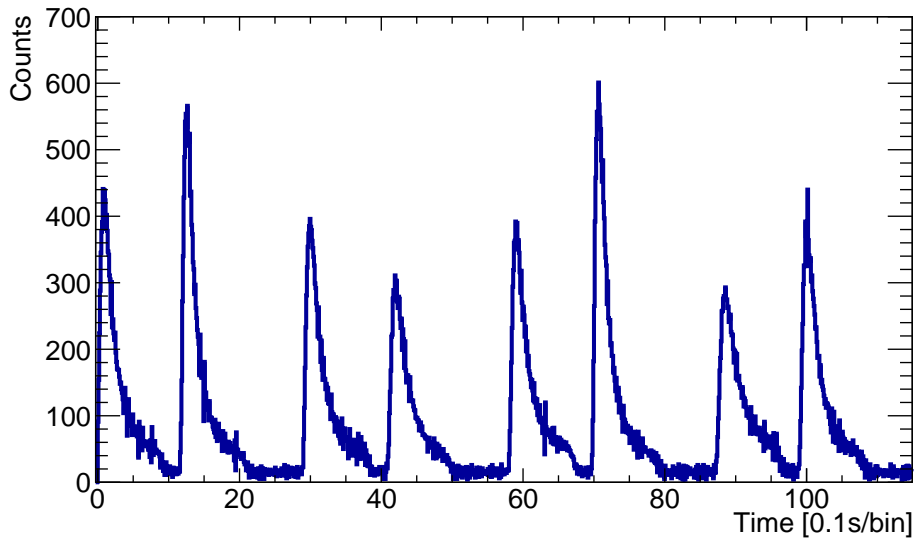
(a)
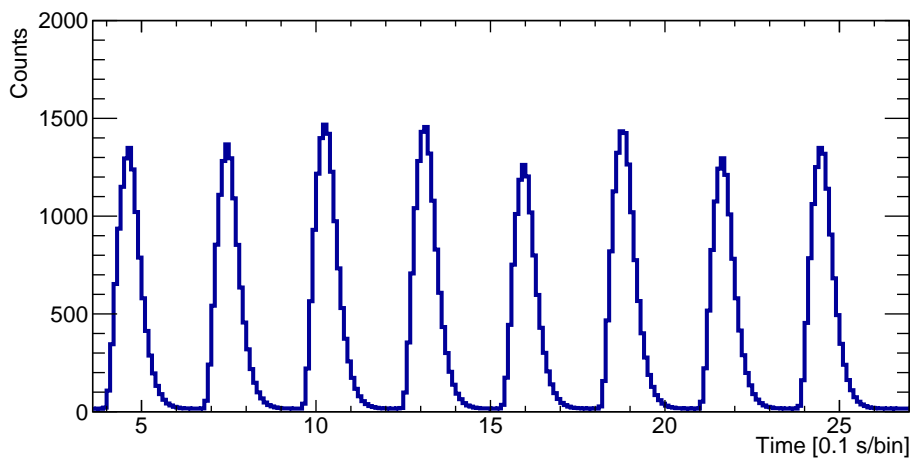
(b)
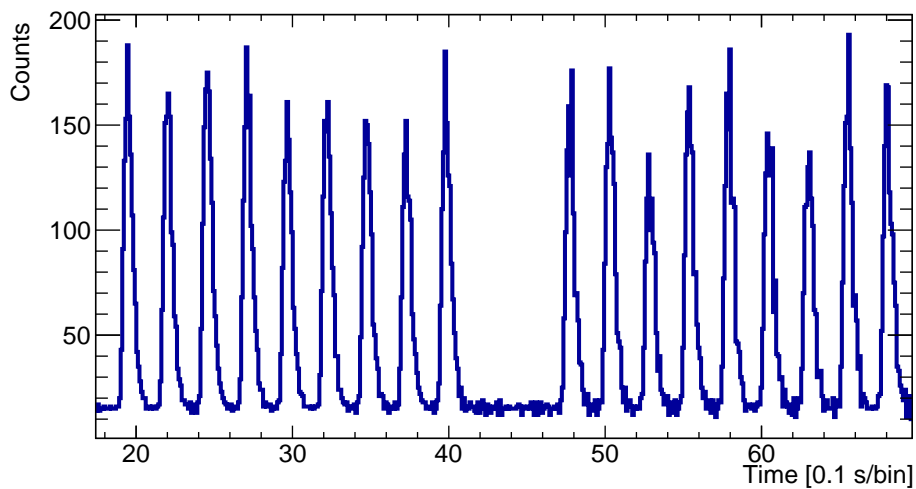
(c)

Figure 5.15: Beam intensity measured with the SEETRAM, (a) with ^{193}W setting (b) with ^{193}Ta setting, and (c) with ^{190}Lu setting.

Table 5.1: Beam cycle in all FRS settings.

Setting	Length of the spill [s]	Time between spills [s]
^{193}W	10.0	1.8
^{193}Ta	1.0	1.8
^{190}Lu	0.7	1.8
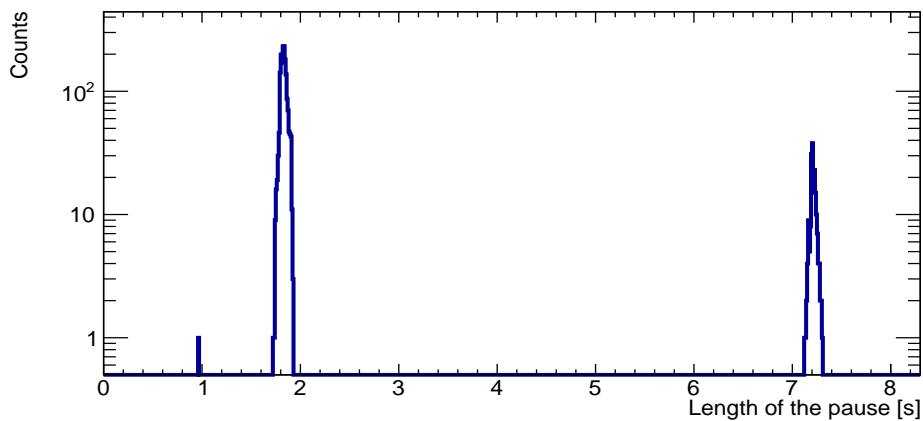
Figure 5.16: Time between spills with the ^{193}Ta setting.

Due to the high fission background during the spills, correlations from the implanted isotope to the subsequent β decay in forward and backward directions in time, as well as in forward direction for the shifted implantations, were determined only between the spills. The measured fragment-β-decay time correlation spectrum determined for ^{199}Os, with the ^{193}Ta setting is shown in Fig 5.17.
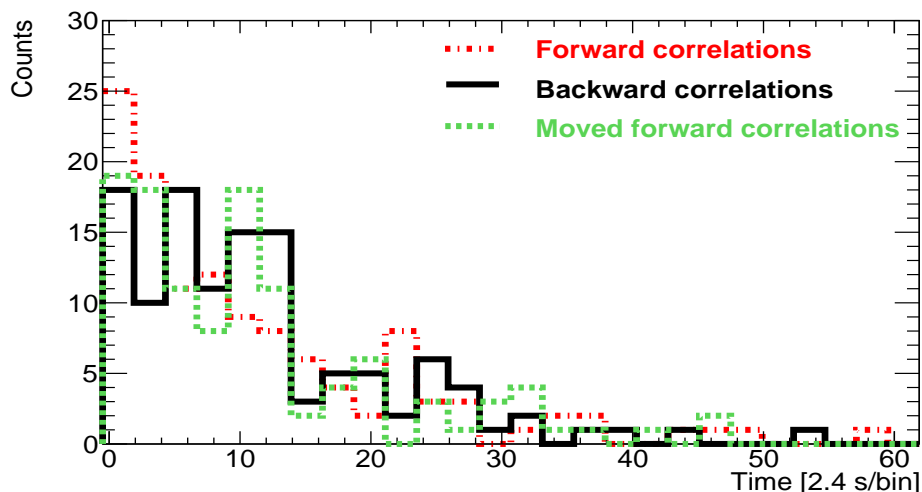
Figure 5.17: Spectra showing time differences between implantation of ^{199}Os and the subsequent β particle. The spectra include the correlations both in forward and backward directions in time, represented by **red** dashed line and **black** line, respectively. Additionally, the correlations in the forward direction are shown by **green** dashed line for implants that have been shifted forward in time.

5.6.3 Fragment-β-decay Monte-Carlo simulations

As mentioned in the previous Section 5.1, the Monte-Carlo code utilized to simulate fragment-β-decay correlations was developed by T. Kurtukian et al. [107]. This code simulates the fragment-β-decay time correlations. The code requires several input parameters, including the measured implantation rate during spills, measured beta rates during pauses, the length of the spills, and time between spills. The free parameters are the detection efficiency of the β decays and the mean lifetime τ.

5.6.4 The χ^2 technique

The measured time-correlation spectra, as shown in Fig. 5.17, differ from the simulated spectra shown in Fig. 5.18. This discrepancy arises due to the limitations in the experimental spectra caused by a limited number of counts in each bin. Furthermore, the experimental spectra are subject to statistical fluctuations following the Poisson distribution.
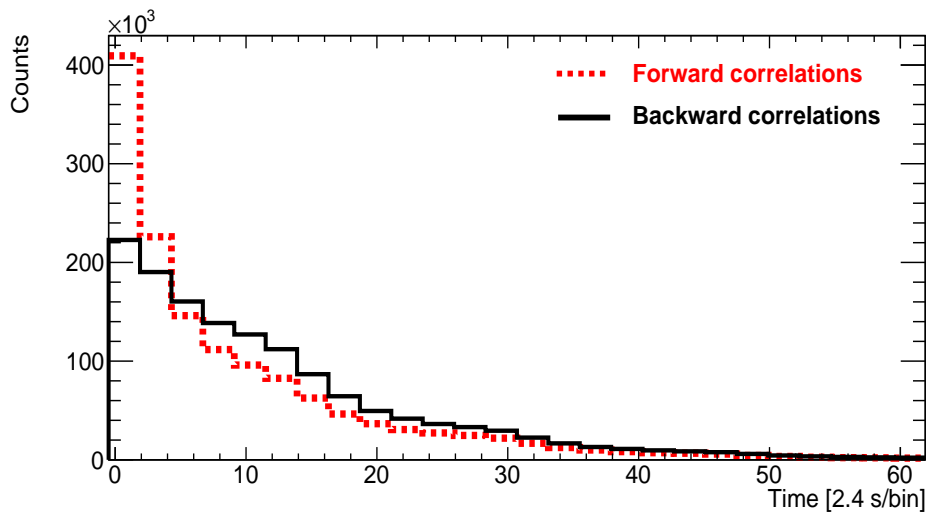
Figure 5.18: Simulated correlation spectra in both the forward and backward directions in time for the ^{199}Os nuclei, represented by **red** dashed line and **black** continuous line, respectively. The simulation was done with the τ of 2.3 s, and the β-detection efficiency of 43 %.

For the half-life determination of the nucleus under investigation, the χ^2 technique was applied. This method aims to determine the simulation that best matches the measured data. The χ^2 test enables the comparison of two data sets, denoted as $g(x_i)$ and $h(x_i)$, to determine whether they originate from the same parent population. The χ^2 calculation can be expressed as follows [98]

$$\chi^2 = \sum_{i=1}^{n} \frac{[g(x_i) - h(x_i)]^2}{\sigma^2(g) + \sigma^2(h)}, \tag{5.1}$$

where the denominator, $\sigma^2(g) + \sigma^2(h)$, represents the variance of the difference between $g(x_i)$ and $h(x_i)$. The expected value for χ^2, denoted as $< \chi^2 >$, equals n, where n represents the number of degrees of freedom. The number of degrees of freedom was calculated by subtracting the number of parameters calculated from the data from the number of bins used to calculate the χ^2.

In addition, the so-called reduced $< \chi_v^2 >$ can be computed dividing the $< \chi^2 >$ by n. The expected value of the reduced chi-squared is 1. If the $< \chi_v^2 >$ value significantly exceeds 1, it indicates large deviations from the predicted distribution. On the other hand, very small value of $< \chi_v^2 >$ also indicates considerable deviations, which are unacceptable [98]. In summary, the $< \chi_v^2 >$ value close to 1 indicates a good comparison between the simulations and measured data.

In the χ^2 technique, Gaussian statistics are assumed, because the standard deviation, i.e. σ, is computed from the Gaussian probability density function. Therefore, about 68.3 % of the events fall within $\pm\sigma$ of the mean, and about 95.4 % fall within $\pm 2\sigma$.

If the aim is to obtain selected variables from the χ^2 fit technique, it is appropriate to apply the least-squares method. This method involves a minimization of the χ^2 for each parameter in order to obtain the optimal values [98]. In the present work, the parameters of interest are the efficiency and half-life. The condition for minimizing χ^2 is that the first partial derivative with respect to each parameter becomes zero. This condition implies that when near a local minimum for all parameters, the behaviour of the χ^2 becomes a quadratic function with respect to that parameter [98]. Furthermore, the errors associated for each parameter can be determined by increasing the χ^2 by one unit from the local minimum.

In the case of a one-parameter experiment, determination of the confidence level is typically straightforward. The data can be plotted, assessed if the distribution follows the Gaussian distribution, and the probability estimated directly from the distribution that the result falls within a specific range. However, when multiple variables are involved, and there exists a correlation between those variables, defining the confidence level becomes more challenging.

The contour plot of χ^2 calculated as a function of two parameters is estimated to be elliptical near the minimum so that the variation of χ^2 with one parameter is independent of the other parameter [98]. However, if there is a correlation between the two variables, the ellipse appears tilted. Therefore, to determine a confidence level of σ, that defines the region in the contour plot where both parameters fall within the 68.3 % probability range, it is necessary to consider the full range of $\Delta\chi^2 = 1$. This approach takes into account the correlation between

the two parameters.

Moreover, to ensure a correct statistical application of the χ^2 calculation, the requirements for the Gaussian statistics have to be fulfilled, and therefore, the number of counts in each bin was required to be larger than 5 [116], or equal to 5 when the so-called Yates correction (0.5 was subtracted from the numerator) [117] was applied to the Equation 5.1. In the present work, the threshold for the number of counts for bins used to calculate the $< \chi^2_v >$ was determined based on the available statistics for the isotope under study.

In this work, the half-lives of interest are determined from two-dimensional χ^2 fits, comparing the ratios of the forward- and backward-time correlation spectra obtained from both simulations and measurements. To ensure that the background determination was not dominated by the beam-induced events, the measured background was also determined by moving the implantation forward in time and computing correlations using the forward-time correlations. These analyses use the least-squares method, which involves the mean lifetime τ and the detection efficiency ϵ for the β particles as the fitting parameters.

5.6.5 Limits of the technique

As explained in the previous section, the β-decay half-life is determined in the present work by using the statistical analysis of the time intervals between the implantation of the chosen fragment and the subsequent β-decay event in the same strip. Gaussian statistics are assumed when performing the χ^2 calculation.

Certain factors need to be considered in order to ensure reliable results in the present analysis. These factors include the efficiency of detecting β particles and the complex β-particle background produced by various fragments. Therefore, having the number of correlated β particles greater than the background fluctuations is crucial, particularly in the histogram region which is used for the β-decay half-life analysis.

If the total number of implanted fragments is denoted as N_f, the rate of β-like particle as F_β, and the detection efficiency for the β particles as ϵ, the following observations can be done. During a time interval of $T_{1/2}$ following the implantation of the fragment, the number of detected "real" β decays is $\frac{N_f \cdot \epsilon}{2}$. At the same time, within this time interval, the corresponding β-particle background detected can be estimated as $N_f \cdot F_\beta \cdot T_{1/2}$, and its square root approximates its statistical fluctuations. Furthermore, assuming that the real correlations should be two times greater than the random correlations, it can be expressed as [108]

$$\frac{N_f \cdot \epsilon}{2} > 2 \cdot \sqrt{N_f \cdot F_\beta \cdot T_{1/2}}. \tag{5.2}$$

By rearranging Equation 5.2, the upper limit for the measurable $T_{1/2max}$ can be written

$$T_{1/2max} < \frac{N_f \cdot \epsilon^2}{16 \cdot F_\beta}. \tag{5.3}$$

In the present analysis, time differences were determined within the same x strip as the implantation to minimize correlations with the background. However, as described in Section 5.6.1, the pixel analysis in the active stopper was not possible, resulting in a higher β-particle background rate. This background includes the β decays of previously implanted fragments near the same strip.

Additionally, the beam cycle produces a periodic time structure for implantations, β particles, and beam-induced background. Therefore, the analysis only focuses on determining time correlations during the pauses between the spills. This approach helps to reduce the impact of the beam cycle on the correlations, and it was successfully employed in the previous analyses conducted under similar conditions [108, 109].

In the case of the ^{193}W setting, the beam cycle consists of 10 s spills with a 1.8 s time gap between the spills, as shown in Fig. 5.15a and Table 5.1. Additionally, this setting produces and delivers most of the fragments at the beginning of the spill. Consequently, this setting creates a non-ideal condition for the analysis method employed in this work, meaning that no equivalent condition is available to determine time correlations in both the forward and backward directions. Therefore, the present work does not concentrate on the analysis of the data with the ^{193}W setting.

In Table 5.2 the number of identified fragments (N_f) at $F4$, the number of implanted fragments (N_i) into the active stopper, the average background rate (F_β) per strip, and the calculated upper limits for the half-lives ($T_{1/2max}$) using the ^{193}Ta and ^{190}Lu settings are shown, respectively. These upper limits were calculated based on the detection efficiency (ϵ) of 30 %.

Table 5.2: Number of identified fragments (N_f) at *F4*, implanted fragments (N_i) into the active stopper, background rate F_β, and calculated upper limit for $T_{1/2max}$ using the ^{193}Ta and ^{190}Lu settings. The values are shown separately for each setting, with a line separating the two sets of data, respectively.

Setting	Isotope	N_f	N_i	F_β $[s^{-1}]$	$T_{1/2max}$ $[s]$
^{193}Ta	^{203}Ir	244	41	0.53	2.6
	^{202}Ir	350	60	0.61	3.2
	^{200}Os	318	56	0.64	2.8
	^{199}Os	379	65	0.53	4.0
	^{197}Re	283	63	0.55	2.9
	^{196}Re	277	68	0.83	1.9
	^{194}W	184	122	1.1	0.9
	^{193}W	169	120	1.0	1.0
	^{191}Ta	121	102	1.0	0.7
	^{190}Ta	97	83	1.0	0.5
^{190}Lu	^{201}Os	78	20	0.24	1.8
	^{199}Re	110	43	0.34	1.8
	^{198}Re	160	84	0.44	2.1
	^{196}W	111	50	0.41	1.5
	^{195}W	159	62	0.42	2.1
	^{193}Ta	50	19	0.52	0.5
	^{192}Ta	95	34	0.45	1.2
	^{190}Hf	26	11	0.30	0.5
	^{189}Hf	45	17	0.34	0.7

In order to determine the half-lives, several parameters need to be considered, as discussed earlier. These include the measured time correlations between the β particles and fragments, the mean lifetime (τ) of the nucleus being studied, the background rate, the detection efficiency of the β particles, the number of fragments, and the time intervals in the histograms, such as the bin width. The time intervals include also the maximum correlation time, denoted as T_{max}, as well as the minimum time between the implantations of the fragments.

The maximum correlation time T_{max} is the time when the implanted fragment can be correlated with the subsequent β particle. It needs to be long enough in order to determine a reasonable decay curve, i.e. the T_{max} should include 2 to 5 half-lives of the nucleus under study [118]. In contrast, very long T_{max} might lead to a false correlation with the background events. The minimum correlation time between the implantations is not constraint in the present work since the different isotopes were implanted in different positions of the active stopper, as shown in Fig. 5.9.

In summary of the discussion above, within the conditions of the present experiment, it was possible to determine the half-lives of 7 isotopes using the least-squares method. These isotopes are ^{200}Os, ^{199}Os, $^{198-196}$Re, ^{191}Ta and ^{195}W. Among these isotopes, four have unknown half-lives ($^{198-197}$Re, ^{191}Ta, and ^{195}W), while

the remaining three have previously measured half-lives.

5.7 Results and discussion

As described in Section 5.6.2, in the present analysis, only the data during the time interval between the spills, denoted as the pause, was considered in order to determine the time correlations. The isotope ^{199}Os was chosen as a reference to proceed with the analysis. This choice was based on its known half-life ($T_{1/2}$) value of 5^{+4}_{-2} s [119, 120], which allowed for comparing the measured values in the present study. Furthermore, the largest upper limit value for $T_{1/2max}$ for this isotope was within the half-life error limits measured previously, as shown in Table 5.2.

After determining the time correlation, the ratios between the forward and backward time correlations were determined to continue to the χ^2 calculations. The resulting ratio spectra for ^{199}Os obtained from the ^{193}Ta data, as well as the simulated ratio spectra for three different mean lifetime (τ) values of 0.1 s, 2.3 s, and 7.0 s, with the efficiency of 43 % are shown in Fig. 5.19. The experimental error bars for the measured data are also included in Fig. 5.19, while the simulations have been done with high statistics, resulting in negligible uncertainties.
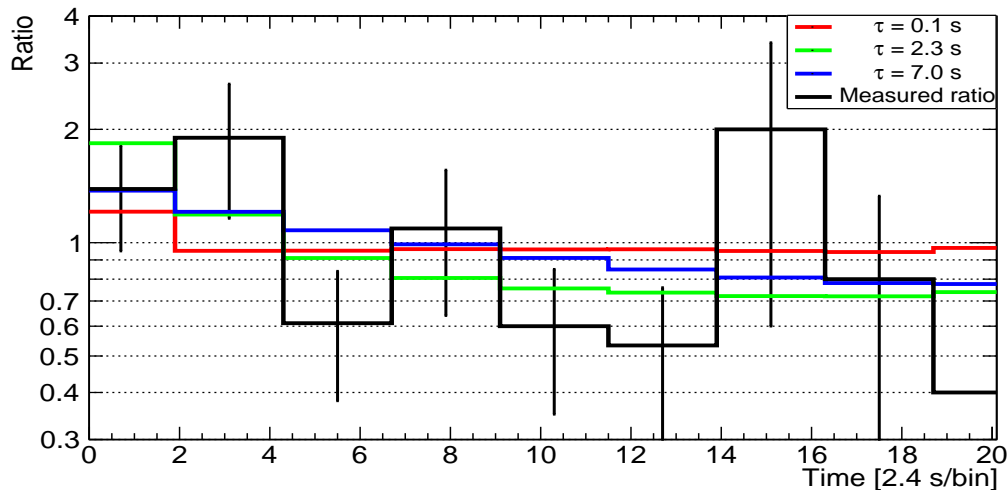
Figure 5.19: Measured ratios of the time difference in forward and backward in time, between the implanted ^{199}Os and the β particle measured in the same strip during the pause between the spills. In addition, simulated ratios with a β-detection efficiency of 43 % and with different values of τ are shown.

As mentioned in Section 5.1, the alternative method was employed to determine the background. This method includes shifting the implantation times to the forward direction by at least two half-lives. The shifted implantation times for ^{199}Os are shown in Fig. 5.20, demonstrating a shift of more than two half-lives.

Subsequently, the false time correlations were determined in the forward direction using β-particle events to continue to the ratio determination.
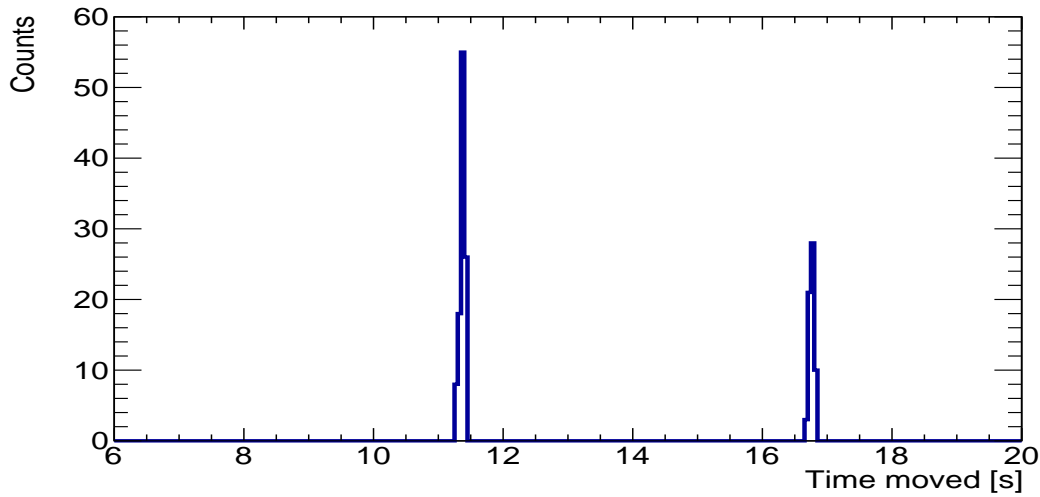
Figure 5.20: Shifted times in the forward direction of the implanted ^{199}Os isotopes using the ^{193}Ta setting.

Next, the ratios between the true forward and the shifted forward correlations were extracted as part of the analysis procedure. The resulting ratio spectra determined for ^{199}Os using the ^{193}Ta data, as well as the simulated ratio spectra with an efficiency of 40 % for three different τ values of 0.1 s, 3.4 s, and 7.0 s are shown in Fig. 5.21.
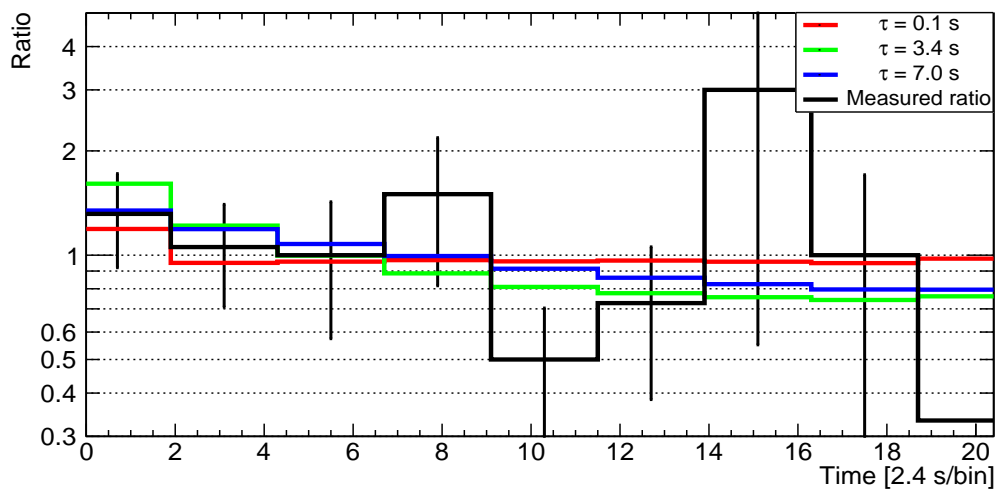
Figure 5.21: Measured ratios of the time differences between the forward correlations, and the supposed background correlations forward in time with shifted implantations, between the implanted ^{199}Os and β particle measured in the same strip during the pause between spills. Additionally, simulated ratios with β-detection efficiency of 40 % and with different mean lifetimes are shown.

As the next step, a series of simulations were conducted with different efficiency and mean lifetime values, followed by the calculations of the χ^2 values from the measured and simulated ratios of the time correlations for each set of simulations. For the extraction of the minimum values for both parameters (efficiency and mean lifetime), two-dimensional χ^2 contour spectra were generated as shown in Fig. 5.22a and 5.22b. In these plots, different colours represent regions where the calculated χ^2 value increases by one, two, and so on. These contour plots allowed the determination of the minimum values, and error limits for both efficiency and mean lifetime. The measured half-life value, was obtained by fitting a second-order polynomial to the region where the minimum value was found, as shown in Fig. 5.23a and 5.23b, while corresponding projections of the χ^2 into efficiency coordinates are shown in Fig. 5.24a and 5.24b.

The analysis method employed in this work yielded measured $T_{1/2}$ values of $1.7^{+1.4}_{-1.1}$ s and $2.4^{+2.9}_{-1.8}$ s for ^{199}Os. The obtained values are consistent with each other, indicating the reliability of the analysis procedure. Furthermore, the $T_{1/2}$ values obtained fall within the error limits of the previously reported $T_{1/2}$ value of 5^{+4}_{-2} s. The corresponding efficiency values were 43^{+26}_{-19} % and 40^{+33}_{-24} %, respectively. These efficiency values also agree with each other, further confirming the reliability of the analysis method employed in this work.
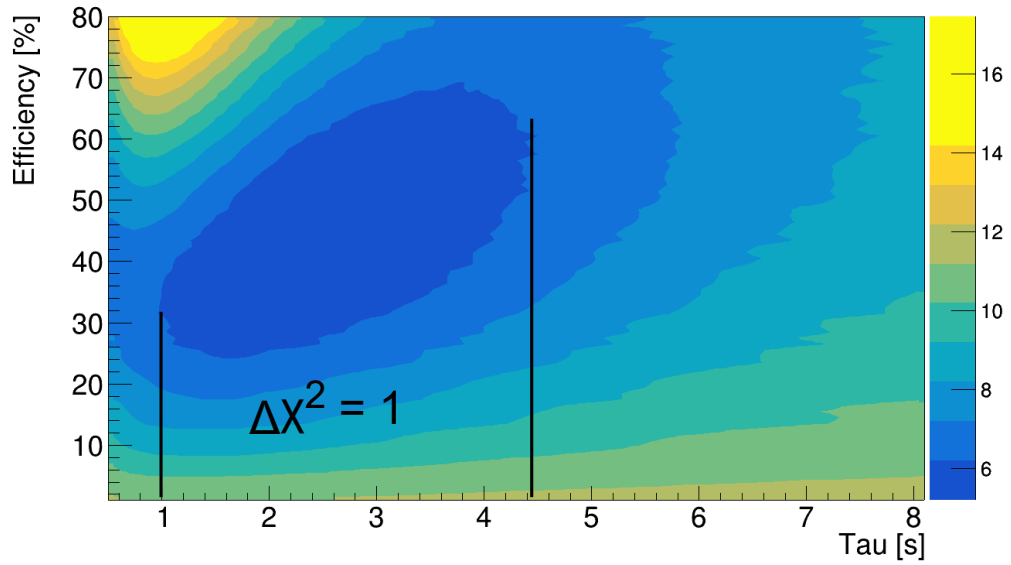
(a)
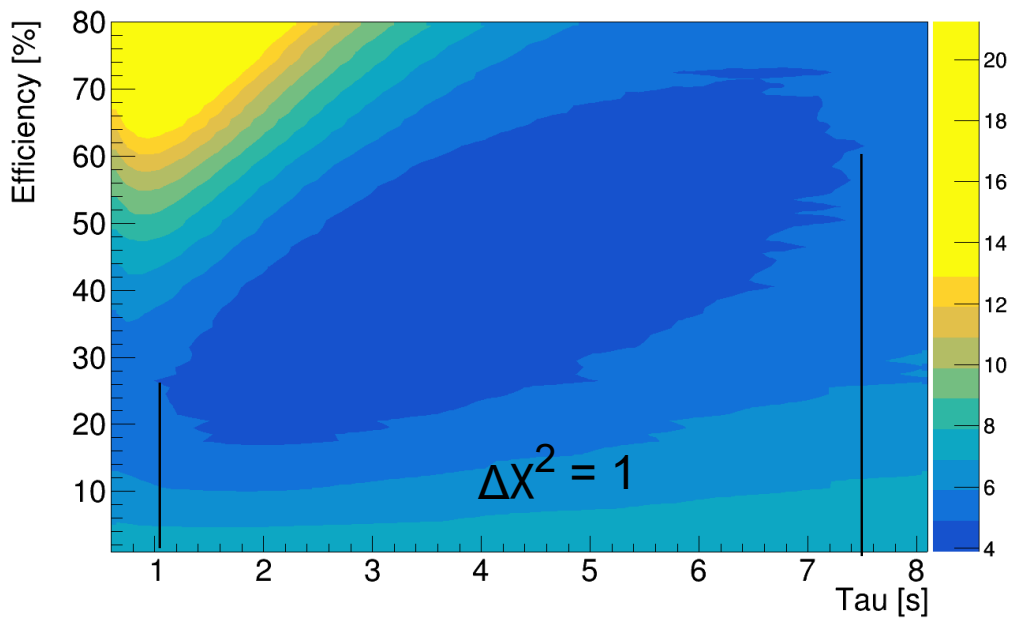
(b)

Figure 5.22: Two-dimensional (mean lifetime and efficiency) χ^2 contour plot with the background determined using (a) backward correlations, and (b) forward correlations of the moved implantations.
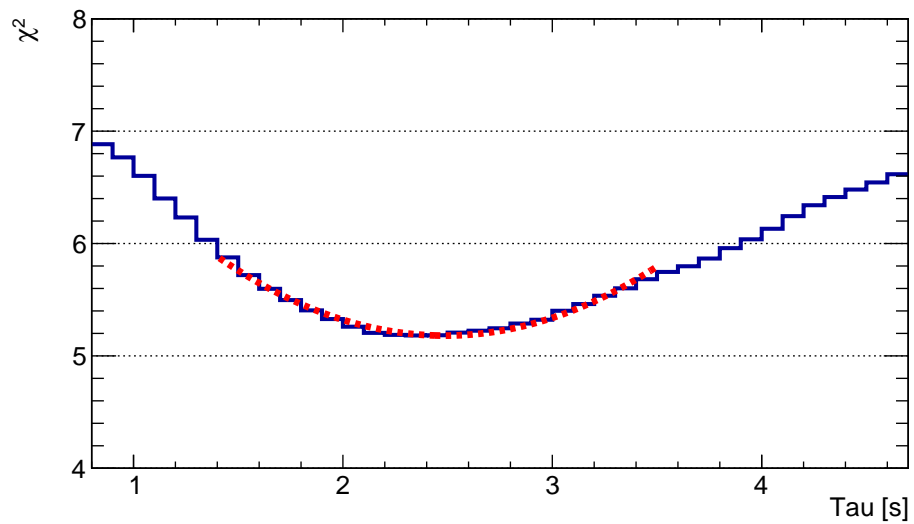
(a)
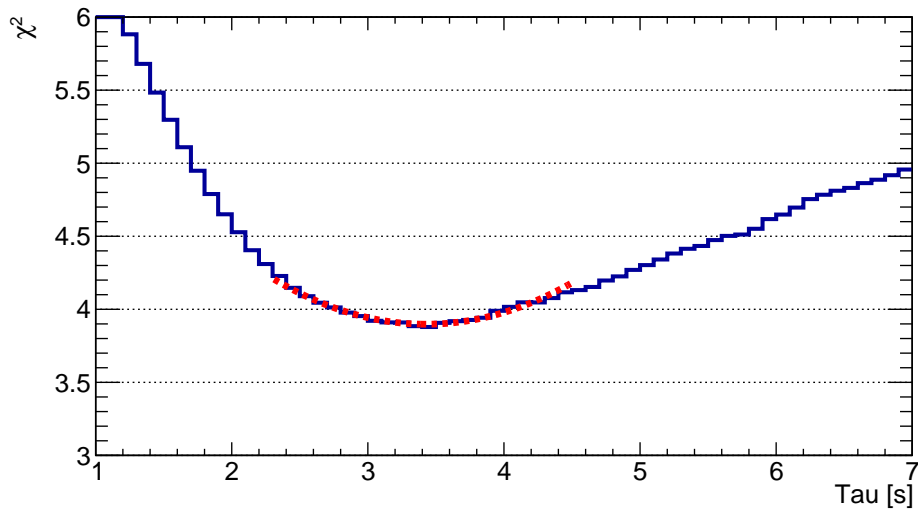
(b)

Figure 5.23: Projection of the calculated χ^2 into the mean lifetime coordinates, with second degree polynomial fits shown with a **red** dashed line for (a) 43 % efficiency, and (b) 40 % efficiency of ^{199}Os isotope.
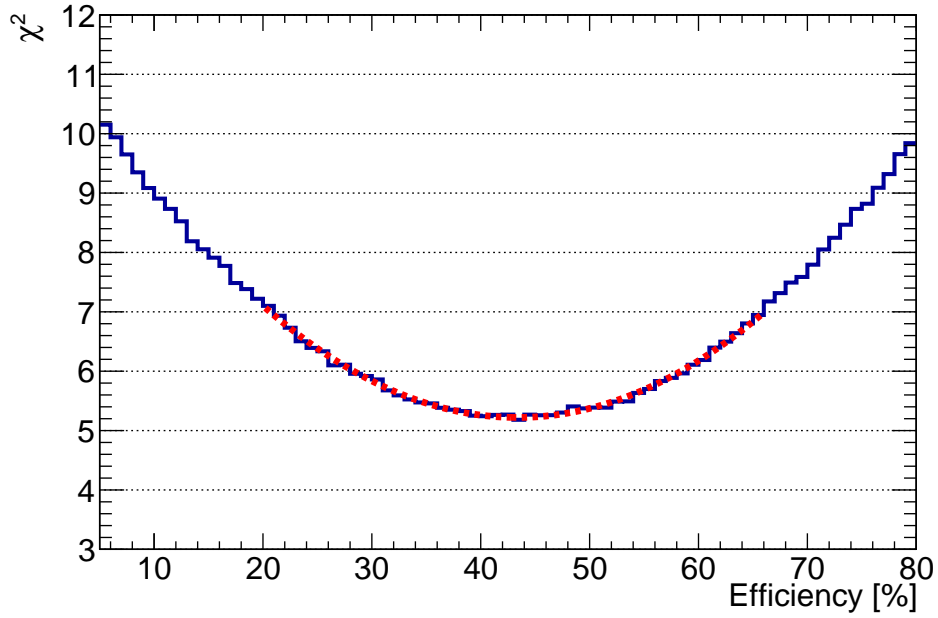
(a)
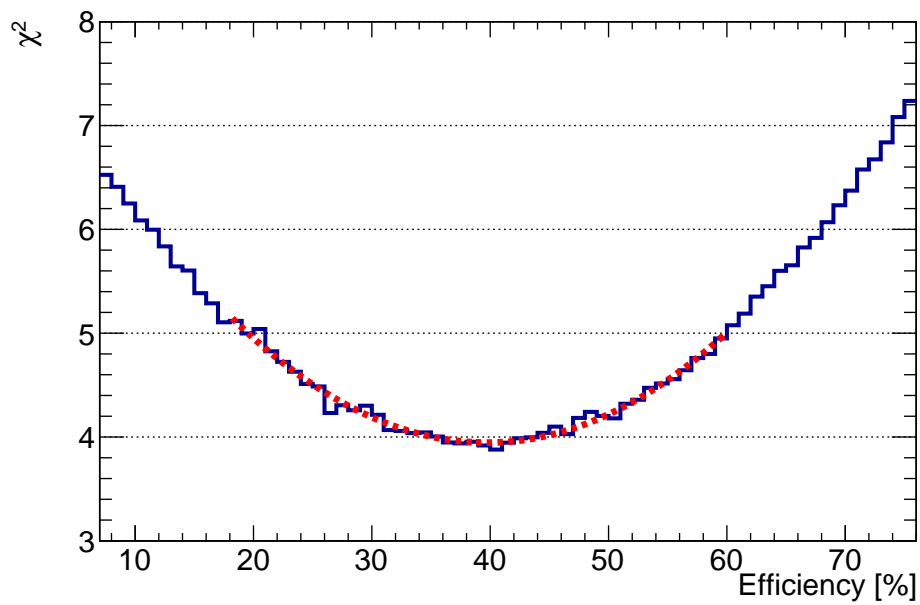
(b)

Figure 5.24: Projection of the calculated χ^2 into the efficiency coordinates, with second degree polynomial fits shown with a **red** dashed line for mean lifetimes of (a) 2.3 s, and (b) 3.4 s of ^{199}Os isotope.

5.7.1 Measured β-decay half-lives

Table 5.3 shows the background determination method, the measured half-life ($T_{1/2}$), the determined efficiency (ϵ), the count limit used per bin for calculating χ^2, and the calculated reduced χ_v^2 value for each nucleus considered in this work. Each reported value corresponds to the minimum of reduced χ_v^2 value. In cases where it was possible to use both methods to determine the background, the obtained values for the half-lives and efficiency are consistent.

The variations observed in the efficiency values shown in Table 5.3 are based on the different implantation profiles and factors such as the position of the implantation. Furthermore, the energy variations between different fragments cause different implantation profiles since the energy of the fragment determines the depth of implantation within the active stopper. Additionally, when fragments enter the active stopper between two DSSDs or near the edge of the detector, there is a higher probability of the β particle escaping. Consequently, this leads to a reduction in the detection efficiency. Hence, the detection efficiency is higher in the middle of the DSSD.

Moreover, it should be noted that one DSSD of the active stopper remained unbiased throughout the entire experiment, leading to a loss in detection efficiency. Additionally, at the beginning of the experiment, individual energy thresholds were set for each strip of the active stopper. Individual thresholds resulted in unequal efficiencies between the strips. In summary, the observed variations in efficiency values can be attributed to factors such as the energy variations of the implanted fragments, implantation position, biased DSSDs, and differing energy thresholds between strips of the active stopper.

Table 5.3: Showing the background determination method utilized for each nucleus, the measured β-decay half-life ($T_{1/2}$), the corresponding efficiency (ϵ), the count limit per bin applied, and the calculated reduced χ_v^2 value for each nucleus analysed in this work.

Nucleus	Background correlations	Measured $T_{1/2}$ [s]	Measured ϵ [%]	Count limit Per bin	χ_v^2
^{200}Os	Forward	$2.3^{+5.0}_{-1.6}$	27^{+40}_{-15}	7	1.9
^{199}Os	Forward	$2.4^{+2.9}_{-1.8}$	40^{+33}_{-24}	8	1.0
^{199}Os	Backward	$1.7^{+1.4}_{-1.1}$	43^{+26}_{-19}	8	1.3
^{198}Re	Backward	$1.0^{+0.8}_{-0.7}$	21^{+13}_{-11}	6	0.9
^{197}Re	Backward	$0.9^{+1.5}_{-0.8}$	17^{+18}_{-11}	5	1.1
^{196}Re	Forward	$2.5^{+3.1}_{-2.0}$	34^{+27}_{-20}	7	3.0
^{196}Re	Backward	$2.2^{+1.9}_{-1.4}$	34^{+21}_{-14}	7	4.6
^{195}W	Forward	$0.8^{+0.7}_{-0.7}$	33^{+21}_{-18}	7	0.8
^{195}W	Backward	$1.2^{+1.7}_{-1.1}$	45^{+18}_{-20}	6	0.2
^{191}Ta	Backward	$1.1^{+1.0}_{-0.7}$	46^{+27}_{-25}	9	0.6

5.7.2 Comparison with literature values and theoretical predictions

The literature half-life values for the $^{200-199}$Os and ^{196}Re isotopes are presented in Table 5.4. All literature values are consistent when compared with the half-life values obtained in the present work . For instance, in the case of ^{196}Re, the difference from previous measurements is about 17 % and 27 %, with the forward correlations and backward correlations (see Table 5.3), respectively, with almost identical lower limits for the half-life but larger upper error limits. However, the present analysis has larger uncertainties, as indicated by the extracted reduced χ_v^2 values of 3.0 and 4.6 when utilizing forward and backward correlations as the background, respectively. The increased uncertainty in the present work could be attributed to the limited statistics available. Specifically, the previous study reported a larger number of fragments (454) compared with the present work (68) (see Table 5.2), resulting in a non-optimal upper limit calculation for $T_{1/2}$ (see Table 5.2).

Table 5.4: β-decay half-life values measured in this work, corresponding literature values and predicted values for the nuclei considered in the present work.

Nucleus	Measured $T_{1/2}$ [s]	Previously measured $T_{1/2}$ [s] [119, 120]	Predicted $T_{1/2}$ [s] (FRDM+QRPA) [56]	Predicted $T_{1/2}$ [s] (CQRPA) [121]
^{200}Os	$2.3^{+5.0}_{-1.6}$	6^{+4}_{-3}	>100	6.6
^{199}Os	$2.4^{+2.9}_{-1.8}$	5^{+4}_{-2}	>100	6.9
^{198}Re	$1.0^{+0.8}_{-0.7}$	-	2.6	
^{197}Re	$0.9^{+1.5}_{-0.8}$	-	4.0	
^{196}Re	$2.5^{+3.1}_{-2.0}$	3^{+1}_{-2}	4.8	1.4
^{195}W	$0.8^{+0.7}_{-0.7}$	-	19.8	
^{191}Ta	$1.1^{+1.0}_{-0.7}$	-	1.8	

So far, various models have been developed to calculate the half-lives of nuclei far from the valley of stability. In this work, two Quasi-particle Random-Phase approximation (QRPA) models were used to compare with experimental results. The first model includes the Finite-Range Droplet Mass Model (FRDM) to predict the masses of the nuclei, and the QRPA calculations within this model consider Gamow-Teller (GT) transitions, including the first-forbidden (FF) transitions based on the Gross Theory [56]. Furthermore, the recent addition to these calculations is the consideration of (n,γ) competition. The theoretical predictions of this model, developed by P. Möller et al., are taken from Ref. [56]. The second model utilized is the density functional+continuum QRPA (CQRPA), computed by I. N. Borzov [58, 59], and the values of theoretical predictions are taken from Ref. [121]. This model takes into account the ground state properties, the FF transitions, the GT transitions, and the excited states by the continuum QRPA calculations. The predicted half-life values by FRDM+QRPA and CQRPA models for all isotopes considered in this study are shown in Table 5.4.

The ratios between the measured half-life values obtained using two background determination methods and the predicted values extracted from FRDM + QRPA and CQRPA calculations are shown in Fig. 5.25. A notable observation is that the FRDM + QRPA model overestimates the half-lives of $^{199-200}$Os isotopes by approximately one order of magnitude. These particular isotopes are the closest to the closed neutron shell at $N = 126$. However, as the mass value decreases, the comparison between experimental and theoretical prediction becomes better, with a difference factor of around two, except for the case of ^{195}W, which contributes to the peak at $A = 195$ in the mass abundance distribution.
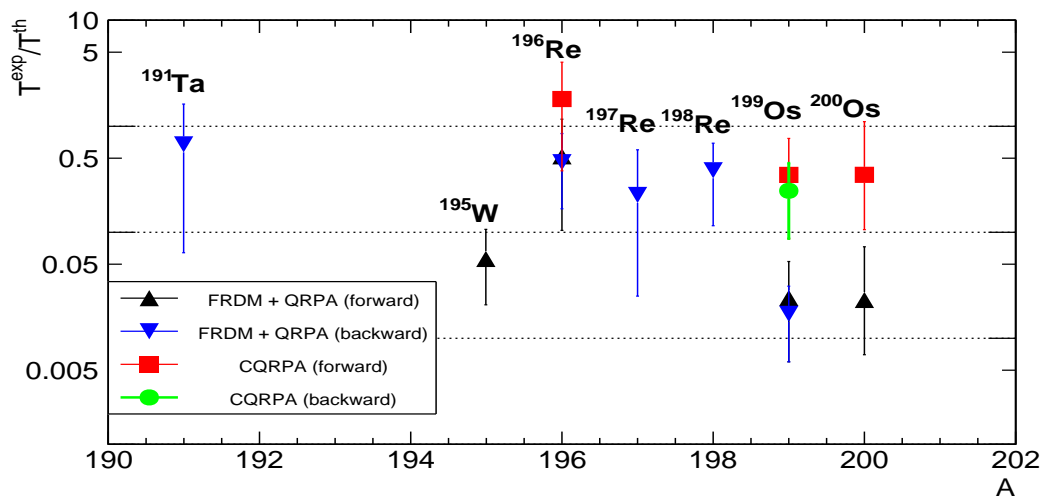
Figure 5.25: Determined ratios of measured half-lives and the theoretical calculations.

The CQRPA model reproduced a closer agreement with the experimental values for all considered nuclei as shown in Fig. 5.25, especially for the nuclei $^{199-200}$Os near the closed neutron shell $N = 126$. For instance, for the ^{196}Re and $^{199-200}$Os isotopes, the difference factor is approximately two and three, respectively, when comparing the CQRPA values with the experimental results. The FF transitions seem to have a significant role in reducing the β-decay half-lives for nuclei approaching closed shell $N = 126$ [5, 59, 122].

The observed results in this work agree with previous experiments [108, 109] demonstrating shorter β-decay half-lives compared with the predicted values. This discrepancy in half-lives influences estimating the timing of r-process element synthesis, particularly for the 3rd r-process mass abundance peak at $A = 195$. Close to this peak, where the half-life of β decay increases, the accumulation of material occurs.

The trend of shorter half-lives, as predicted based on the FRDM model, has led to the study of the impact of shorter half-lives on the r-process nucleosynthesis [123]. This study suggests several effects of the half-lives. Firstly, there is an accelerated mass flow towards heavier nuclei after passing the waiting point at $N = 126$, which is a consequence of the shorter half-lives and influences the

progression of nucleosynthesis. Furthermore, it has been suggested that there is faster consumption of neutrons due to the shorter half-lives. As a result, different conditions arise for the r-process freeze-out, where neutron capture and β-decay towards stability occur within a similar time scale.

M. R. Mumpower *et al.* have been investigating the influence of specific nuclear properties on r-process nucleosynthesis in Ref. [124] and references therein. They observed that the difference between measured and predicted half-lives, based on the FRDM + QRPA model, becomes more significant when the measured β-decay half-life value increases and the Q_β value is small [124]. Their study also showed that variations in predicted half-lives can influence the final abundance pattern. Additionally, the sensitivity of the abundance pattern to the β-decay properties of the ^{195}W isotope was noted [124, 125]. However, it is important to note that the models also use nuclear masses in the calculations, and the accuracy of ± 0.5 MeV in the nuclear mass can result in the changes of predicted half-lives by a factor of about 2 to 4 [126].

The comparisons presented show the importance of measuring β-decay half-lives for heavy neutron-rich nuclei far from the valley of stability. These measurements play an important role in testing existing models and simulations. However, there is lack of information regarding β-decay half-lives near the $N = 126$ shell, which is crucial for modelling the amount of matter transported into the fission region. Consequently, acquiring more experimental data is necessary to address the question of how elements heavier than iron are produced in the universe.

5.7.3 Scientific impact of the present work

In this work, the half-lives of three previously measured nuclei are compared with literature values, and the comparison shows consistency. Furthermore, four new half-lives are measured for the first time and are compared with two theoretical predictions. The decay half-life of an exotic nucleus is one of its most fundamental properties and often the first property measured.

Experimentally accessing the neutron-rich nuclei is extremely difficult, and the present experiment was conducted as an exploratory experiment to address this issue. For accurate r-process modelling, the determination of β-decay half-lives for hundreds of nuclei is required. Achieving this is beyond the scope of a single experiment. Nevertheless, this particular experiment represents a significant step towards this goal, pushing the experimental boundaries closer to the closed shell at $N = 126$.

In the region of the chart of nuclei studied, half-lives provide important input to the nucleosynthesis models that predict, for instance, the location of the r-process and origins of the abundance peaks. In this work, the shorter β-decay half-lives compared to predicted values were obtained. Consequently, it influences

the timing of r-process element synthesis, especially for the 3rd r-process mass abundance peak at $A = 195$, where the accumulation of material occurs. The results obtained highlight the importance of first-forbidden β decay and subsequent reduction in half-lives, emphasizing the need for additional experimental data in this specific region.

In the future, the neutron-rich nuclei will be studied in various facilities such as at FAIR, Argonne N=126 Factory [127], and RIKEN [128]. At FAIR, utilizing the Super-FRS, the upcoming experiments are expected to offer better precision and access to more exotic isotopes since the produced isotopes can be identified with the Super-FRS on event-by-event basis up to 1 MHz counting rate utilizing the GEM-TPC detectors.

6 CONCLUSIONS

The objectives of this work were to investigate new β-decay half-lives of neutron-rich nuclei close to the $N = 126$ neutron shell and investigate the performance of the prototype GEM-TPC detector in the twin configuration. The aim was to extract new nuclear data near the third r-process peak in the mass abundance distribution. Certain requirements are needed for the experimental setup to achieve this experimental goal, such as producing heavy neutron-rich nuclei, identifying them accurately, and having the capability to analyse the collected data.

The experiment, *S468* at the GSI facility, fulfilled these requirements. Heavy neutron-rich nuclei were produced using the fragmentation of a relativistic lead beam. Thereafter, the FRS was utilized to identify and deliver the produced heavy neutron-rich nuclei to the β-decay station, where they were implanted in the active stopper to study their half-lives.

The results presented in this work provide information about the properties of neutron-rich nuclei located in the vicinity of the "waiting point" at $N = 126$. The delayed-coincidence method, initially presented by T. Kurtukian et al. [107], was used to measure four new half-lives for the isotopes $^{197-198}$Re, ^{195}W, and ^{191}Ta. Additionally, the half-life values of $^{199-200}$Os and ^{196}Re isotopes were remeasured, and the obtained values were consistent with the literature values, confirming the reliability of the results. The analysis method deals with the challenging background structure in the time-correlation spectra.

Additionally, an alternative method was utilized to confirm the background shape of the implantation-β-decay correlations, ensuring reliability and consistency of the results. This alternative method included shifting the implantation forward in time and determining the background correlations in the forward direction. By utilizing this method, the half-lives of previously measured isotopes ^{199}Os and ^{196}Re, as well as the new half-life for ^{195}W isotope, were measured. The

comparison between the literature values and measured values, using the forward correlations as the background, showed consistency for all the isotopes under study.

The measured half-lives of heavy neutron-rich nuclei were compared with predicted values from two different models. The first model considered was the Finite-Range Droplet Mass Model, and the Quasi-particle Random-Phase Approximation (FRDM + QRPA), which includes the Gamow-Teller (GT) transitions from the QRPA calculations, the first-forbidden (FF) transitions based on the Gross Theory, and the competition of (n,γ). The second model, known as the density functional+continuum QRPA (CQRPA), considers the ground-state properties, the FF transitions, the GT transitions, and the exited states through continuum QRPA calculations. Comparison between the measured and predicted half-life values showed that the FRDM + QRPA overestimates the half-lives by approximately one order of magnitude near the closed shell $N = 126$. On the other hand, the CQRPA model provided a closer agreement with measured values, with a relative difference of about two to three for all considered isotopes. However, only three predicted half-life values were available from the CQRPA model, limiting the extent of the comparison.

In several experiments, a consistent trend of shorter half-life values compared with the predicted values has been observed for nuclei approaching the closed shell $N = 126$. This finding highlights the importance of the FF transitions in reducing the β-decay half-lives. The shorter half-lives near $N = 126$ contribute to an accelerated accumulation of material into the third r-process peak and towards heavier nuclei. Consequently, the faster consumption of neutrons leads to different conditions for the r-process freeze-out.

Further experiments will be essential to confirm the influence of the FF transitions near the $N = 126$ nuclei approaching the neutron drip line. Confirming these results could lead to revisions in existing theoretical models to predict β-decay half-lives, enabling more accurate predictions of the properties of r-process nuclei close to the third peak of the abundance pattern. Such revisions have the potential to impact our understanding of r-process nucleosynthesis significantly.

M.R. Mumpower et al. have been investigating the impact of half-life differences compared with predictions on the final abundance pattern. They studied how variations in the predicted half-life values for selected nuclei could influence the overall abundance distribution. They observed that the differences in half-life values used in the calculations could indeed have an influence on the final abundance pattern. For instance, the isotope ^{195}W was identified as an important nucleus for sensitivity studies.

In the future, to achieve accurate identification at the forthcoming Super-FRS, the performance of the prototype GEM-TPC detector in the twin configuration was studied in two individual in-beam tests. These studies aimed to determine if the

detector fulfils the requirements for operation at the Super-FRS. The Super-FRS GEM-TPC detector provides the position measurements of the particles. Hence, it plays an important role in the identification.

The performance analysis of the prototype GEM-TPC detector provided information on several of its properties. The investigated properties included the x resolution, y resolution, cluster strip multiplicity, control sum, detection and tracking efficiencies, the impact of summing up the strip signals, and the influence of data digitization. Notably, the data analysis of the prototype GEM-TPC detector involved the utilization of clusterization for the first time. During the analysis, a significant discovery was made regarding calibrating multiple detectors within the same setup. It was found that a single scintillator calibration grid could be effectively utilized to calibrate multiple detectors simultaneously. This can potentially simplify the calibration process. In addition, two different methods were utilized and tested for the offline alignment process, ensuring robustness and reliability in the alignment process.

The performance analysis of the prototype GEM-TPC detector showed that it met the required position resolution of less than 1 mm for both x and y directions. The measured cluster strip multiplicity using P10 gas (90 % Ar, 10 % CH_4) was consistent with previous measurements. The study of the control sum showed the influence of the angle of the incoming beam on the control sum. However, the control sum values measured in this work were consistent across different electric fields and x positions. The detector achieved a tracking efficiency of over 95 % with the beam intensity of 1k ions/spill, and a detection efficiency of close to 100 % up to the beam intensity of 50k ions/spill. Additionally, the impact of data digitization was investigated. It was found that reducing the data digitization from 13 bits to 4 bits did not significantly affect the position reconstruction. The observed spatial resolution remained consistent, although the amplitude of the cluster and cluster strip multiplicity decreased.

Despite the successful experiments in the present work, certain improvements can be implemented in future experiments. Some modifications can be implemented in the experimental setup aimed at studying β-decay properties at the GSI facility. The fragmentation reaction proved effective in producing heavy neutron-rich nuclei, which were successfully delivered to the β-decay station. However, the beam cycles selected with a relatively short time interval between beam pulses limited the opportunity to determine fragment-β-decay correlations before new beam pulses deliver new fragments decaying via β decay. Therefore, allowing for a longer time gap between beam pulses would be beneficial, enabling the study of longer β-decay half-lives. Furthermore, the statistics in the present work were limited, resulting in larger uncertainties. Therefore, if feasible, allocating more time for each setting would improve statistical precision. The possibility of measuring β-decay - γ-ray coincidences would also help reduce uncertainties associated with background correlations. Additionally, some challenges in the present work were related to the high intensities observed at the focal plane

F2, where particular detectors could handle the intensities of up to a few kHz with high detection efficiency. Although the scintillators used at the *F2* caused inaccuracies in the identification, these were corrected with the mass-tagging with the FRS ion Catcher and simulations from LISE++ and MOCADI.

Several improvements can be implemented for future experiments investigating the performance of the prototype GEM-TPC, mainly focusing on the experimental setup. The accurate calibrations of the reference trackers are essential to ensure reliable results in the performance study of the detector under investigation. Having a well-defined setup, including accurate distances and angles in mounting the detectors, contributes to the results obtained. Additionally, confirming the alignment process using a narrow beam perpendicular to all trackers can reduce measurement uncertainties. If feasible, selecting reference trackers with higher resolution than the detector under study would be beneficial, as it allows for more precise performance analysis. Additionally, in future experiments, the detector should be tested with particle rates close to 1 MHz to test high-intensity performance. By implementing these improvements, future experiments studying the performance of the prototype GEM-TPC will yield more accurate results, providing information on the capabilities and characteristics of the detector.

In summary, the results of the comparison between measured half-lives and theoretical predictions presented in this work are valuable information. The findings could be utilized to validate the existing models and evaluate the associated uncertainties. Additionally, the information obtained from the performance study of the prototype GEM-TPC detector has practical benefits for future experiment planning and further supports its usage in upcoming research. In the coming years, the FAIR facility, with one of its main objectives in the physics program to expand research on the r-process path far from the valley of stability, will provide an opportunity to measure more β-decay data. This is only possible with event-by-event particle identification at high counting rates and with high efficiency. In the present work, the performance of the prototype GEM-TPC has been investigated, which will eventually develop into the Super-FRS GEM-TPC. More exotic neutron-rich nuclei can be identified by using the GEM-TPC at the Super-FRS, thus providing an opportunity for a deeper understanding of nucleosynthesis processes and investigating the origin of heavy elements in the universe.

104

REFERENCES

[1] M. Luoma et al. *In-beam test results of the Super-FRS GEM-TPC detector prototype with relativistic uranium ion beam, Nucl. Instr. and Meth. in Phys., vol. , A1052 pp. 168-262* (2023). URL https://doi.org/10.1016/j.nima.2023.168262.

[2] M. Luoma et al. *DEVELOPMENT OF A NEW CLUSTERIZATION METHOD FOR THE GEM-TPC DETECTOR, 13th Particle Acc. Conf. IPAC2022, pp. 233-236* (2022).

[3] J. Cowan and C. Sneden . *Heavy element synthesis in the oldest stars and the early Universe, Nature, 440, 1151* (2006). doi:10.1038/nature04807.

[4] E.M. Burbidge, G.R. Burbidge, W.A. Fowler, and F. Hoyle. *Synthesis of the Elements in Stars, Rev. Mod. Phys., vol. 29, pp. 547-650* (1957). URL https://link.aps.org/doi/10.1103/RevModPhys.29.547.

[5] J. J. Cowan et al. *Origin of the heaviest elements: The rapid neutron-capture process, Rev. Mod. Phys., 93(015002), 491-494* (2021). doi:10.1103/RevModPhys.93.015002.

[6] E. M. Holmbeck, T. M. Sprouse, and M. R. Mumpower. *Nucleosynthesis and observation of the heaviest elements, Eur. Phys. J., A 59:28* (2023). URL https://doi.org/10.1140/epja/s10050-023-00927-7.

[7] R. W. Parsons and C. H. Collie. *Photodisintegration of the Heavy Elements, Proceedings of the Physical Society. Section A, 63, 839* (1950). URL https://dx.doi.org/10.1088/0370-1298/63/8/306.

[8] M. Arnould and S. Goriely. *The p-process of stellar nucleosynthesis: astrophysics and nuclear physics status, Physics Reports, vol. 384, pp. 1-84* (2003). URL https://doi.org/10.1016/S0370-1573(03)00242-4.

[9] M. G. Mayer. *The Shell Model, Science, 145(3636), 999-1006* (1964). doi:10.1126/science.145.3636.999.

[10] G. J. Mathews and J. J. Cowan. *New insights into the astrophysical r-process, Nature, 345(6275), 491-494* (1990). doi:10.1038/345491a0.

[11] F.-K. Thielemann et al. *What are the astrophysical sites for the r-process and the production of heavy elements?, Progress in Particle and Nuclear Physics, 66(2), 346-353* (2011). URL https://doi.org/10.1016/j.ppnp.2011.01.032.

[12] S. Goriely, A. Bauswein, and H.-T. Janka. *r-PROCESS NUCLEOSYNTHESIS IN DYNAMICALLY EJECTED MATTER OF NEUTRON STAR MERGERS, The Astrophysical Journal Letters, 738, L32* (2011). doi:10.1088/2041-8205/738/2/L32.

[13] B. P. Abbott et al. *Observation of Gravitational Waves from a Binary Black Hole Merger, Phys. Rev. Lett., 116, 061102* (2016). doi:10.1103/PhysRevLett.116.061102.

[14] LIGO Collaboration and Virgo Collaboration. *Gravitational Waves and Gamma-Rays from a Binary Neutron Star Merger: GW170817 and GRB 170817A, The Astrophysical Journal Letters, 848, L13, 27pp* (2017). URL https://doi.org/10.3847/2041-8213/aa920c.

[15] I. Arcavi et al. *Optical emission from a kilonova following a gravitational-wave-detected neutron-star merger, Nature, 551, 64-66* (2017). doi:10.1038/nature24291.

[16] J.-J. Gaimard and K.-H. Schmidt. *A reexamination of the abrasion-ablation model for the description of the nuclear fragmentation reaction, Nucl. Phys. A, 531:709* (1991). doi:10.1016/0375-9474(91)90748-U.

[17] R. Serber. *New insights into the astrophysical r-process, Phys. Rev. 72:1114-1115* (1947). doi:10.1103/PhysRev.72.1114.

[18] Ch. Engelmann et al. *Production and identification of heavy Ni isotopes: evidence for the doubly magic nucleus $^{78}_{28}Ni$, Z. Phys. Nucl. A 352* (1995). doi:10.1007/BF01299748.

[19] H. Geissel et al. *Projectile Fragment Separator, A proposal for the SIS-ESR experimental program (1987); and GSI Report GSI-89-30 (1989); G. Münzenberg et al., Proc . 1st Int. Conf. on Radioactive Nuclear Beams (World Scientific, Singapore, 1990) p . 91 .*

[20] H. Geissel et al. *The Super-FRS project at GSI, Nucl. Instr. and Meth. in Phys., vol. B204, pp. 71-85* (2003).

[21] J. Kurcewicz et al. *Discovery and cross-section measurement of neutron-rich isotopes in the element range from neodymium to platinum with the FRS, Physics Letters B, 717, 371-375* (2012). URL https://doi.org/10.1016/j.physletb.2012.09.021.

[22] G. Münzenberg et al. *Identification of element 107 by α correlation chains, Zeitschrift für Physik A Atoms and Nuclei, 300, 107-108* (1981). doi:10.1007/BF01412623 .

[23] G. Münzenberg et al. *Observation of one correlated α-decay in the reaction ^{58}Fe on $^{209}Bi \rightarrow ^{267}109$, Zeitschrift für Physik A Atoms and Nuclei, 309, 89-90* (1982). doi:10.1007/BF01420157 .

[24] G. Münzenberg et al. *The identification of element 108, Zeitschrift für Physik A Atoms and Nuclei, 317, 235-236* (1984). doi:10.1007/BF01421260 .

[25] S. Hofmann et al. *Production and decay of $^{269}110$, Zeitschrift für Physik A Hadrons and Nuclei, A 350, 277-280* (1995). doi:10.1007/BF01291181.

[26] S. Hofmann et al. *The new element 111, Zeitschrift für Physik A Hadrons and Nuclei, A 350, 281-282* (1995). doi:10.1007/BF01291182.

[27] S. Hofmann et al. *The new element 112, Zeitschrift für Physik A Hadrons and Nuclei, A 354, 229-230* (1996). doi:10.1007/BF02769517.

[28] G. Münzenberg et al. *The velocity filter ship, a separator of unslowed heavy ion fusion products, Nuclear Instruments and Methods, 161, 65-82* (1979). doi:10.1016/0029-554X(79)90362-8.

[29] H. Müller et al. *SUPERCONDUCTING MAGNETS FOR SUPER-FRS: PRODUCTION AND TESTING STATUS, 12th Particle Acc. Conf. IPAC2021* (2021).

[30] H. Geissel et al. *The GSI projectile fragment separator (FRS): a versatile magnetic system for relativistic heavy ions, Nucl. Instr. and Meth. in Phys., vol. B70, pp. 286-297* (1992).

[31] R. Janik et al. *Time Projection Chambers with C-pads for heavy ion tracking, Nucl. Instr. and Meth. in Phys., vol. A640, pp. 54-57* (2011). URL https://doi.org/10.1016/j.nima.2011.02.052.

[32] F. García et al. *A GEM-TPC in twin configuration for the Super-FRS tracking of heavy ions at FAIR, Nucl. Instr. and Meth. in Phys., vol. A884, pp. 18-24* (2018).

[33] M. Arnould and S. Goriely and K. Takahashi. *The r-process of stellar nucleosynthesis: Astrophysics and nuclear physics achievements and mysteries, Physics Reports, vol. 450, pp. 97-213* (2007). URL https://doi.org/10.1016/j.physrep.2007.06.002.

[34] Y. W. Hao, Y. F. Niu, and Z. M. Niu. *Synthesis of the Elements in Stars, The American Astronomical Society, vol. 933* (2022). URL https://dx.doi.org/10.3847/1538-4357/ac6fdc.

[35] G. Martínez-Pined et al. *The role of fission in the r-process, Progress in Particle and Nuclear Physics, 59, 199-205* (2007). URL https://doi.org/10.1016/j.ppnp.2007.01.018.

[36] K. Lodders. *Solar System Abundances of the Elements, arXiv* (2010). URL https://doi.org/10.48550/arXiv.1010.2746.

[37] B. Pfeiffer, K.-L. Kratz and P. Möller. *Status of delayed-neutron precursor data: half-lives and neutron emission probabilities, Progress in Nuclear Energy, 41, 39-69* (2002). URL https://doi.org/10.1016/S0149-1970(02)00005-7.

[38] H. Becquerel. *Contribution à l'étude du rayonnement du radium,Journal de Physique Théorique et Appliquée, 9, 190-199* (1900). URL https://doi.org/10.1051/jphystap:019000090019000.

[39] C. D. Anderson. *The Apparent Existence of Easily Deflectable Positives, Science, 76, 238-239* (1932). doi:10.1126/science.76.1967.238.

[40] F. Joliot. *Les nouveaux radioéléments. Preuves chimiques des transmutations, Journal de Chimie Physique, 31, 611-620* (1934). URL https://doi.org/10.1051/jcp/1934310611.

[41] L. W. Alvarez. *Nuclear K Electron Capture, Physical Review, 52, 134-135* (1937). URL https://doi.org/10.1103/PhysRev.52.134.

[42] G. C. Wick. *Sugli elementi radioattivi di F. Joliot e I. Curie, Atti R. Acc. Naz. Lincei. Rend, 19, 319–324* (1934).

[43] H. Yukawa and S. Sakata. *Proceedings of the Physico-Mathematical Society of Japan. 3rd Series, 17, 467* (1935). URL https://doi.org/10.11429/ppmsj1919.17.0_467.

[44] E. Fermi. *Tentativo di una Teoria Dei Raggi β, Nuovo Cim 11, 1–19* (1934). URL https://doi.org/10.1007/BF02959820.

[45] K. S. Krane. *Introductory nuclear physics, John Wiley Sons* (1991).

[46] J. S. Lilley. *Nuclear Physics Principles and Applications, John Wiley Sons* (2004).

[47] G. Gamow. *Nuclear Spin of Radioactive Elements, Proceedings of the Royal Society of London. Series A, Containing Papers of a Mathematical and Physical Character, 146, 217* (1934).

[48] G. Gamow and E. Teller. *Selection Rules for the β-Disintegration , Physical Review, 49, 895* (1936).

[49] G. F. Knoll. *Radiation Detector and measurement, John Wiley sons, New York, 3rd edition, ISBN: 0-471-07338-5* (1999).

[50] S. Koyama, K. Takahashi and M. Yamada. *Gross Theory of Nuclear β-Decay, Progress of Theoretical Physics, 41, 1470-1503* (1969). URL https://doi.org/10.1143/PTP.41.1470.

[51] S. Koyama, K. Takahashi and M. Yamada. *Gross Theory of β-Decay and Its Application to the Fermi Matrix Element, Progress of Theoretical Physics, 44, 663-688* (1970). URL https://doi.org/10.1143/PTP.44.663.

[52] K. Takahashi. *Gross Theory of First Forbidden β-Decay, Progress of Theoretical Physics, 45, 1466-1492* (1971). URL https://doi.org/10.1143/PTP.45.1466.

[53] T. Tachibana, M. Yamada, and Y. Yoshida. *Improvement of the Gross Theory of β-Decay. II: One-Particle Strength Function, Progress of Theoretical Physics, 84, 641-657* (1990). URL https://doi.org/10.1143/ptp/84.4.641.

[54] H. Nakata, T. Tachibana and M. Yamada. *Semi-gross theory of nuclear β-decay, Nuclear Physics A, 625, 521-553* (1997). URL https://doi.org/10.1016/S0375-9474(97)00413-2.

[55] P. Möller, J. R. Nix and K.-L. Kratz. *NUCLEAR PROPERTIES FOR ASTRO-PHYSICAL AND RADIOACTIVE-ION-BEAM APPLICATIONS*, Atomic Data Nucl. Data Tables, 66, 131-343 (1997).*

[56] P. Möller et al. *Nuclear properties for astrophysical and radioactive-ion-beam applications (II), Atomic Data and Nuclear Data Tables, vol. 125, pp. 1-192 (2019).* URL https://doi.org/10.1016/j.adt.2018.03.003.

[57] M. R. Mumpower, T. Kawano, and P. Möller. *Neutron-γ competition for β-delayed neutron emission, Phys. Rev. C, 94, 064317 (2016).* URL https://link.aps.org/doi/10.1103/PhysRevC.94.064317.

[58] I. N. Borzov. *Gamow-Teller and first-forbidden decays near the r-process paths at $N = 50, 82$, and 126, Phys. Rev. C, 67, 025802 (2003).* URL https://link.aps.org/doi/10.1103/PhysRevC.67.025802.

[59] I. N. Borzov. *Beta-Decay of Nuclei Near the Neutron Shell N = 126, Phys. Atom. Nuclei 74, 1435–1444 (2011).* URL https://doi.org/10.1134/S1063778811100024.

[60] H. H. Heckman, D. E. Greiner, P. J. Lindstrom and F. S. Bieser. *Fragmentation of ^{14}N Nuclei at 29 GeV: Inclusive Isotope Spectra at $0°$, Phys. Rev. Lett. 28, 926 (1972).*

[61] H. Geissel, G. Münzenberg and K. Riisager. *Secondary Exotic Nuclear Beams, Annu. Rev. Nucl. Part. Sci., 45:163–203 (1995).* URL https://doi.org/10.1146/annurev.ns.45.120195.001115.

[62] M. Steiner et al. *Preliminary measurements of SIS 18 beam parameters, Nucl. Instr. and Meth. in Phys., vol. A312, pp. 420-424 (1992).* .

[63] *Discovery of Nuclides Project:*. URL https://people.nscl.msu.edu/~thoennes/isotopes/. Accessed on February 21st, 2023.

[64] G. Wrizenberg. *The separation techniques for secondary beams, Nucl. Instr. and Meth. in Phys., vol. B70, pp. 265-275 (1992).* URL https://doi.org/10.1016/0168-583X(92)95942-K.

[65] L. Audouin et al. *Recoil spectrometers for heavy-ion identification and secondary-beam production: Pushing the low-energy limit, Nucl. Instr. and Meth. in Phys., vol. A548, pp. 517-539 (2005).*

[66] H. Folger et al. *Targets and degraders for relativistic heavy ions at GSI, Nucl. Instr. and Meth. in Phys., vol. A303, pp. 24-33 (1991).* URL https://doi.org/10.1016/0168-9002(91)90759-J.

[67] J-P. Hucka. *PhD. thesis, Control System for the Next Generation In-flight Separator Super-FRS applied for New Isotope Search with the FRS (2023).*

[68] H. Geissel et al. *Ions penetrating through ion-optical systems and matter — non-liouvillian phase-space modelling, Nucl. Instr. and Meth. in Phys., vol. A282, pp. 247-260 (1989).* URL https://doi.org/10.1016/0168-9002(89)90148-4.

[69] Chun-Wang Ma et al. *Nuclear fragments in projectile fragmentation reactions, Progress in Particle and Nuclear Physics, 121, 53-74 (2021).* doi:10.1016/j.ppnp.2021.103911.

[70] C. Scheidenberger et al. *Charge states of relativistic heavy ions in matter, Nucl. Instr. and Meth. in Phys., vol. B142, pp. 441-462 (1998).* URL https://doi.org/10.1016/S0168-583X(98)00244-4.

[71] O. B. Tarasov and D. Bazin. *LISE++.* URL :http://lise.nscl.msu.edu/lise.html. Accessed on March 29th, 2023.

[72] O. B. Tarasov and D. Bazin. *LISE++: Exotic beam production with fragment separators and their design, Nucl. Inst. and Meth. in Phys. B (376), 185-187 (2016).* URL http://lise.nscl.msu.edu/lise.html. doi:http://dx.doi.org/10.1016/j.nimb.2016.03.021.

[73] V. Hlinka et al. *Time projection chambers for tracking and identification of radioactive beams, Nucl. Instr. and Meth. in Phys., vol. A419, pp. 503-510 (1998).*

[74] F. García et al. *IEEE Nuclear Science Symposium conference record, ISSN: 1095-7863, pp. 269-272 (2009).*

[75] M. Pfutzner et al. *Energy deposition by relativistic heavy ions in thin argon absorbers, Nucl. Inst. and Meth. in Phys. B (86), 213–218 (1994).*

[76] O. Kiselev et al. *Radiation hardness tests of Si detectors for Time of Flight measurements at the Super-FRS, MU-NUSTAR- FRS-03, 137 p (2014).*

[77] B. Jurado, K.-H. Schmidt and K.-H. Behr. *Application of a secondary-electron transmission monitor for high-precision intensity measurements of relativistic heavy-ion beams, Nucl. Instr. and Meth. in Phys., vol. A483, pp. 603-610 (2002).* URL https://doi.org/10.1016/S0168-9002(01)01931-3.

[78] M. Weber et al. *Beam-Profile Monitors with Gas Amplification and Current Readout for the Projectile-Fragment Separator, Gesellschaft Für Schwerionenforschung mbH Darmstadt (1990).*

[79] *TPC Technical Manual.* URL https://www-win.gsi.de/frs/technical/FRSsetup/detectors/tpc/tpcmanual.pdf. Accessed on May 2nd, 2023.

[80] A. Prochazka, C. Nociforo, and B. Sitar. *Efficiency simulation of TPC detectors, GSI Report 2013-1, p. 174 (2013).*

[81] A. Prochazka et al. *In-beam Test of the TwinTPC at FRS, GSI Report 2015-1, p. 500 (2014).* doi:10.15120/GR-2015-1.

[82] F. Sauli. *GEM: A new concept for electron amplification in gas detectors, Nucl. Instr. and Meth. in Phys., vol. A386, pp. 531-534* (1997).

[83] F. García et al. *The Super-FRS GEM-TPC prototype development - TDR, arXiv* (2016). doi:10.48550/ARXIV.1612.05045.

[84] R. Schneider and A. Stolz. *Technical Manual Ionization Chamber MU-SIC80,*. URL https://www-win.gsi.de/frs/technical/FRSsetup/detectors/music80/music80_manual.pdf. Accessed on May 2nd, 2023.

[85] H. Weick. *How to set up the FRS - From SIS extraction of primary beam to isotope identification.* URL https://web-docs.gsi.de/~weick/frs/frs-steps.html. Accessed on May 1st, 2023.

[86] N. Kuzminchuk-Feuerstein. *Hamamatsu R9800 Specifications.* URL https://web-docs.gsi.de/~nkuzminc/Images/R9800_H10580.pdf. Accessed on March 10th, 2023.

[87] N. Kuzminchuk-Feuerstein. *Hamamatsu R2083 Specifications.* URL https://web-docs.gsi.de/~nkuzminc/Images/R2083.pdf. Accessed on March 10th, 2023.

[88] N. Kuzminchuk-Feuerstein. *TOF FRS Update,*. URL https://web-docs.gsi.de/~nkuzminc/TOF_Update.html. Accessed on May 2nd, 2023.

[89] CDT CASCADE Detector Technologies GmbH. *CASCADE Detector Technologies.* URL www.n-cdt.com. Accessed on June 6th, 2023.

[90] C. J. Schmidt et al. *Characterization of the n-XYTER chip and preparations for the engineering run, CBM Progress Report* (2009).

[91] S. Minami et al. *Design and implementation of a data transfer protocol via optical fiber, 2010 17th IEEE-NPSS Real Time Conference, 1-3* (2010). doi:10.1109/RTC.2010.5750447.

[92] J. Hoffmann. *TRIXOR, PC-based Trigger Module.* URL www.gsi.de/fileadmin/EE/Module/TRIXOR/trixor.pdf. Accessed on March 21st, 2023.

[93] H.G.Essel, N. Kurz. *The general purpose data acquisition system MBS, IEEE Trans. Nucl. Sci 47 (2) (2000) 336.* doi: 10.1109/RTCON.1999.842672.

[94] F. García et al. *Twin GEM-TPC prototype (HGB4) beam test at GSI – a development for the Super-FRS at FAIR, GSI Report 2015-1, p. 140* (2015). doi:10.15120/GR-2015-1-MU-NUSTAR-FRS-04.

[95] P. Wieczorek, H. Flemming, H. Deppe. *Low Noise Amplifier with Adaptive Gain Settings - (AWAGS) ASIC, TWEPP* (2021).

[96] E. Rocco et al. *AWAGS: A single ASIC to identify fast ions from protons to uranium, Nucl. Instrum. and Methods in Phys., A, 167188* (2022). URL https://doi.org/10.1016/j.nima.2022.167188.

[97] URL https://www.gsi.de/work/forschung/experimentelektronik/ digitalelektronik/digitalelektronik/\module/font_end_module/febex/ febex3b. Accessed on March 4th, 2023.

[98] P. Bevington and D. K. Robinson. *Data Reduction and Error Analysis for the Physical Sciences, McGraw-Hill, third edition* (2003).

[99] A. Prochazka et al. *Simulations of the GEM-TPC response, GSI SCIENTIFIC REPORT 2013* (2014). doi:10.15120/GR-2014-1-FG-S-FRS-12.

[100] R. Farinelli et al. *GRAAL: Gem Reconstruction And Analysis Library, Journal of Physics: Conference Series, 1525(1), 012116* (2020). doi:10.1088/1742-6596/1525/1/012116.

[101] R. Veenhof. *Garfield - simulation of gaseous detectors* (2021). URL https:// garfield.web.cern.ch/garfield/. Accessed on March 15th, 2023.

[102] *Garfield++ software.* URL https://garfieldpp.web.cern.ch/garfieldpp/. Accessed on March 15th, 2023.

[103] J. Kaminski et al. *Study of various anode pad readout geometries in a GEM-TPC, IEEE Transactions on Nuclear Science, 52(6), 2900-2906* (2005). doi:10.1109/TNS.2005.862797.

[104] A. Herlert et al. *The NUSTAR program at FAIR, EPJ Web of Conferences 71* (2014). URL https://doi.org/10.1051/epjconf/20147100064.

[105] N. Kalantar-Nayestanaki and A. Bruce. *NUSTAR: NUclear STructure Astrophysics and Reactions at FAIR, Nuclear Physics News, 28:3, 5-11* (2018). doi:10.1080/10619127.2018.1495476.

[106] J. Erler, N. Birge, M. Kortelainen et al. *The limits of the nuclear landscape, Nature 486, 509–512* (2012). URL https://doi.org/10.1038/nature11188.

[107] T. Kurtukian et al. *A new analysis method to determine β-decay half-lives in experiments with complex background, Nucl. Instr. and Meth. in Phys., vol. A589, pp. 472-483* (2008). doi: https://doi.org/10.1016/j.nima.2008.02.098.

[108] T. Kurtukian. *PhD. Thesis, PRODUCTION AND β DECAY HALF-LIVES OF HEAVY NEUTRON-RICH NUCLEI APPROACHING THE STELLAR NUCLEOSYNTHESIS R-PROCESS PATH AROUND A=195, Universidade de Santiago de Compostela* (2006).

[109] A. López. *PhD. Thesis, β-delayed γ-ray spectroscopy of heavy neutron-rich nuclei produced by cold-fragmentation of 208 Pb, Universidade de Santiago de Compostela* (2011).

[110] R. Kumar et al. *Testing of a DSSSD detector for the stopped RISING project, Nucl. Instr. and Meth. in Phys., vol. A598, pp. 754-758* (2009).

[111] URL http://www.mesytec.com. Accessed on March 28th, 2023.

[112] J. Hoffmann, N. Kurz and M. Richter. *TRIVA 7, VME Trigger Module,* (2011). URL www.gsi.de/fileadmin/EE/Module/TRIVA/triva7_1.pdf. Accessed on July 2nd, 2023.

[113] URL http://www.nndc.bnl.gov/nudat3/. Accessed on March 29th, 2023.

[114] W. R. Plaß et al. *The FRS Ion Catcher – A facility for high-precision experiments with stopped projectile and fission fragments, Nucl. Instr. and Meth. in Phys., vol. B317, pp. 457-462* (2013). URL https://doi.org/10.1016/j.nimb.2013.07.063.

[115] N. Iwasa, H. Weick and H. Geissel. *New features of the Monte-Carlo code MOCADI, Nucl. Instr. and Meth. in Phys., vol. B269, pp. 752-758* (2011). URL https://doi.org/10.1016/j.nimb.2011.02.007.

[116] J. R.Taylor. *An introduction to Error Analysis.* University Science Books, second edition (1997). ISBN: 978-0-935702-42-2.

[117] F. Yates. *Contingency Tables Involving Small Numbers and the χ^2 Test, Supplement to the Journal of the Royal Statistical Society, Vol. 1, No. 2, pp. 217-235* (1934). URL https://www.jstor.org/stable/2983604.

[118] R. Peierls. *Statistical error in counting experiments, Proc. R. Soc. Lond. A. 149, 467–486* (1935). URL http://doi.org/10.1098/rspa.1935.0076.

[119] T. Kurtukian-Nieto et al. *First access to beta half-lives approaching the r-process path near N=126, arXiv,* (2007). URL https://doi.org/10.48550/arXiv.0711.0101.

[120] A. I. Morales et al. *Half-Life Systematics across the $N = 126$ Shell Closure: Role of First-Forbidden Transitions in the β Decay of Heavy Neutron-Rich Nuclei, Phys. Rev. Lett., vol. 113* (2014). doi:10.1103/PhysRevLett.113.022702.

[121] T. Kurtukian-Nieto et al. *Beta-decay half-lives of new neutron-rich isotopes of Re, Os and Ir approaching the r-process path near N = 126, Eur. Phys. J. A 50, 135* (2014). doi:10.1140/epja/i2014-14135-5.

[122] Q. Zhi et al. *Shell-model half-lives including first-forbidden contributions for r-process waiting-point nuclei, Phys. Rev. C, 87, 025803* (2013). doi:10.1103/PhysRevC.87.025803.

[123] O. L. Caballero et al. *Local and global effects of beta decays on r-process, arXiv, 1405.0210* (2014). URL https://doi.org/10.48550/arXiv.1405.0210.

[124] M. R. Mumpower et al. *The impact of individual nuclear properties on r-process nucleosynthesis, Progress in Particle and Nuclear Physics 86, 86-126* (2016). URL https://doi.org/10.1016/j.ppnp.2015.09.001.

[125] T. Kajino and G. J. Mathews. *Impact of new data for neutron-rich heavy nuclei on theoretical models for r-process nucleosynthesis, Rep. Prog. Phys. 80, 084901* (2017). doi: 10.1088/1361-6633/aa6a25.

[126] M. R. Mumpower et al. *Impact of individual nuclear masses on r-process abundances, Phys. Rev. C, 92, 035807* (2015). doi:10.1103/PhysRevC.92.035807.

[127] G. Savard et al. *The N = 126 factory: A new facility to produce very heavy neutron-rich isotopes, Nucl. Inst. and Meth. in Phys. B, 463, 258-261* (2020). doi.org/10.1016/j.nimb.2019.05.024.

[128] Y. Hirayama et al. *Nuclear spectroscopy of r-process nuclei using KEK Isotope Separation System, Nucl. Inst. and Meth. in Phys. B, 463, 425-430* (2020). doi.org/10.1016/j.nimb.2019.04.035.